MSc Thesis
Kapteyn Astronomical Institute
RIJKSUNIVERSITEIT GRONINGEN

# Forging Planets:

*Exploring the magma-ocean geochemistry of Super-Earths and Sub-Neptunes*


*Author:*
Jorick Lania
S4094336

*Supervisor:*
Tim Lichtenberg
*Co-Supervisor:*
Rob Spaargaren
*2nd Examiner:*
Inga Kamp


Groningen July 30, 2025

# Abstract

Planets sustaining large-scale magma oceans are a likely outcome of planet formation, and can be sustained for up to Gyr timescales. Due to convection in the molten mantle and atmosphere, these reservoirs may attain chemical equilibrium in this time, with the metal core possibly participating in the equilibration. This will impart significant changes in the compositions of the atmosphere, mantle and core, and has implications for planet evolution and their current demographics.

This thesis expands on a chemical equilibrium model incorporating 26 species across the atmosphere, mantle and metal core, forming a chemical network that captures the fundamentals of atmosphere-mantle exchange and silicate-metal partitioning. Solutions satisfying chemical equilibrium are obtained via a combined Simulated Annealing - Markov Chain Monte Carlo approach. I implement additional statistics to gauge model performance, and expand on previous work by extending this modelling to additional parameters. The aim of this thesis is to investigate atmospheres resulting from global chemical equilibrium with a magmatic interior, to investigate potential trends that can observationally be tied to their interior conditions.

The net result of equilibration is reduction of the melt via ingress of $\mathrm{H_2}$ and oxidation of the atmosphere via silicate evaporation. Results show that the core-mantle equilibration temperature $T_{eq}$ controls the degree of partitioning of $\mathrm{H}$, $\mathrm{O}$ and $\mathrm{Si}$ into the metal. For $T_{eq} > 3500$ K, most of the atmosphere is recycled into the interior, leaving a tenuous $\mathrm{CO}$ dominated atmosphere. $\mathrm{SiO}$ and $\mathrm{H_2O}$ become abundant species in all model atmospheres after equilibration, with both reaching higher abundances when the metal core cannot equilibrate with the rest of the planet. Steadily more $\mathrm{CO}$ and $\mathrm{CO_2}$ are observed in the atmosphere for higher $T_{eq}$, suggesting that their increased abundance could be tied to hotter planetary interiors.

I conclude that the equilibrated atmospheres' enrichment in particularly $\mathrm{SiO}$ and $\mathrm{H_2O}$ may present an opportunity for distinguishing magma ocean atmospheres from conventionally $\mathrm{H_2}$ dominated atmospheres in the infrared, while abundances of $\mathrm{CO}$ and $\mathrm{CO_2}$ may be tied to the interior temperature.

# Contents

# 1 Introduction

## 1.1 Background

Ever since the detections of the first extrasolar worlds by Wolszczan and Frail [1992] and Mayor and Queloz [1995], the field of exoplanetary research has seen significant expansion and advancement. Each new mission dedicated to exoplanet detection invariably revealed more and more candidates, while simultaneously extending our view to broader exoplanet classes - starting with massive, close-in planets before detecting planets with more varied sizes, orbital distances, inclinations and densities. Today, over 5900 exoplanets have been discovered [Christiansen et al., 2025], with thousands of potential candidates still awaiting confirmation. This boom in the population of the exoplanet 'zoo' shows no signs of stopping, and even free-floating extragalactic planets have fallen into the sights of our telescopes in recent years [Bhatiani et al., 2019].

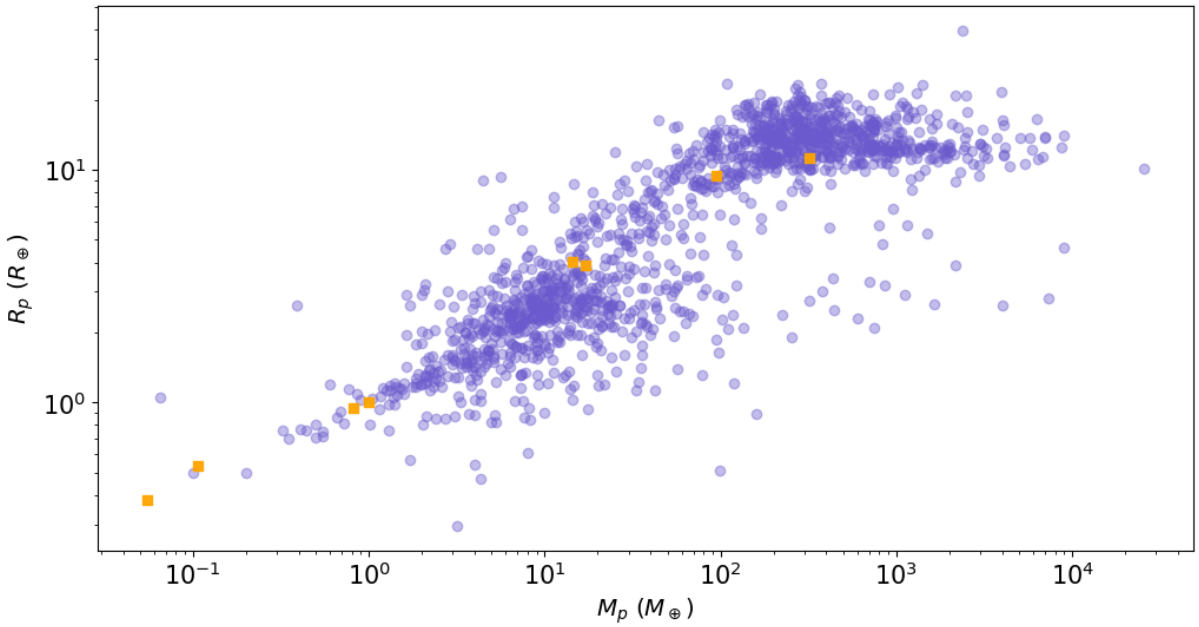


**Figure 1: Mass-Radius diagram of a small exoplanet sample.** Planet masses and radii are listed in terms of Earth units. Of this exoplanet sample, over 90% were discovered via transit photometry. Solar system planets are shown with orange square markers. From left to right: Mercury, Mars, Venus, Earth, Uranus, Neptune, Saturn, Jupiter. This figure was made with data taken from the NASA exoplanet archive.

The diversity of these exoplanetary systems is remarkable. Even if we look at only their masses and radii, our observations span roughly five and four orders of magnitude respectively. Even a subset of the observed exoplanet population fills most of the gaps between the Solar System planets in mass/radius space, with observed planets ranging from Mars-sized rocky bodies to gas giants that exceed Jupiter in mass and radius (Figure 1).

The first detections of exoplanets additionally highlighted the diversity in their environments: the very first confirmed exoplanet orbits a stellar remnant rather than a main-sequence star [Wolszczan and Frail, 1992], and the discovery and study of 51 Pegasi b by Mayor and Queloz [1995] shows the existence of planet types and orbits that do not exist in our own solar system, with 51 Peg b being a gas giant of size comparable to Jupiter, yet on a close-in orbit that is seven times smaller in semi-major axis than Mercury's orbit around the Sun. It remains an open question whether solar systems such as our own are a common outcome of planet formation.

The diversity of exoplanets extends to their ages as well. The oldest exoplanets discovered are several Gyr old, while one of the youngest stands at approximately 17 Myr old according to Rizzuto et al. [2020]. Exoplanets whose host stars are stellar remnants, such as those discovered by Wolszczan and Frail [1992] around a millisecond pulsar, are evidence of what we might call 'second generation' exoplanets - planets who formed from debris disks resulting from supernovae rather than from protoplanetary disks. Observing exoplanets in differing stages of their formation and evolution offers several benefits; these observations are a boon to theories of planetary formation, but the observations of rocky exoplanets in particular may provide windows into Earth's prebiotic past. Close-in rocky exoplanets may undergo various geological stages like magma-oceans, snowball cycles or runaway greenhouse climates, all of which are examples of periods of planetary evolution that may have shaped Earth's current atmosphere and climate. As such, researching exoplanet compositions across these various stages of evolution will inform us on Earth's own formation, and possibly about the conditions in which early life developed on Earth.

## 1.2 Super-Earths, Sub-Neptunes and the Radius Valley

Of the exoplanets observed, most have radii smaller than Neptune ($< 4R_{\oplus}$), falling somewhere between the masses and sizes of the terrestrial and giant planets of the Solar System. This population in turn can be divided into super-Earths (ie. planets whose mass, radius and densities approach the terrestrial planets) and sub-Neptunes (ie. those who approach Neptunian densities). The apparent prevalence of these planets is interesting, especially considering that there are no analogues to these types of planets present in our Solar System. Furthermore, their prevalence begs the question of whether these planet types represent common outcomes of planet formation, and what the mechanism behind their formation is, should this be the case.

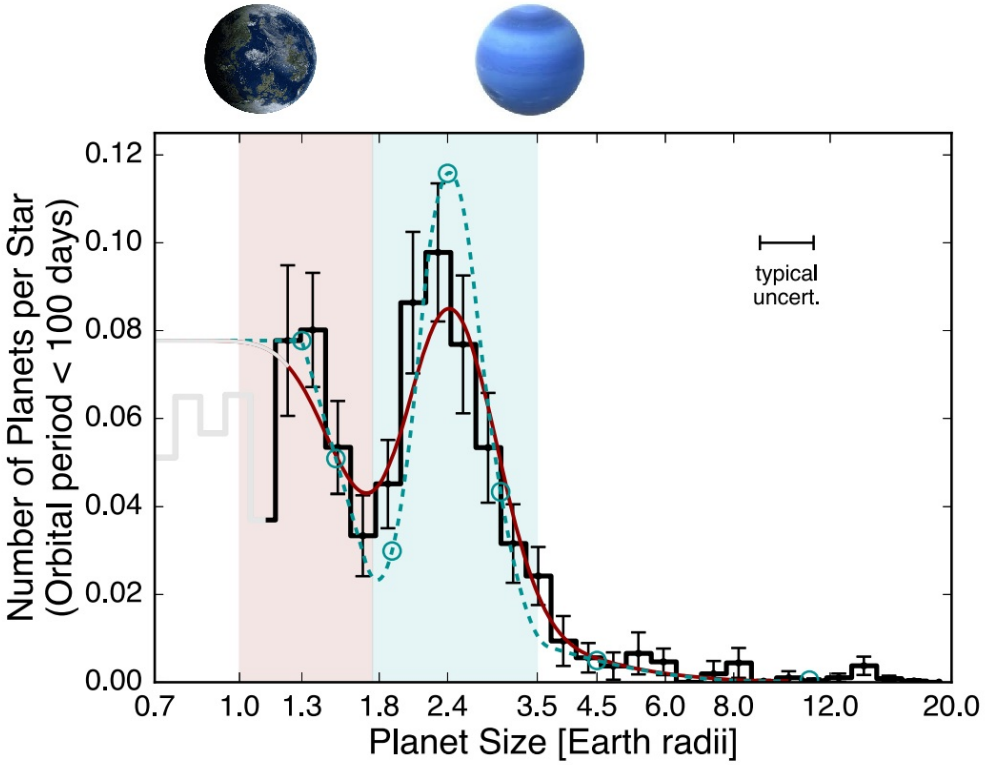


**Figure 2: Completion-corrected histogram of planets in the California-Kepler sample with orbital periods < 100 days.** The occurrence of planets appears bimodal, peaking once around 1.3 $R_\oplus$ (super-Earths, red region) and again at 2.4 $R_\oplus$ (sub-Neptunes, blue region). Red and cyan lines indicate best-fit splines models for the planetary occurrence rate, for which the light grey left portion of the histogram was not included due to poor completeness. Adapted from Fulton et al. [2017]

While we observe a large population of planets with radii below 1.5 $R_\oplus$ and another population with larger radii of roughly 2 - 2.5 $R_\oplus$, there is a noticeable drop in the occurrence rate of planets with radii between these populations. Put simply, planets with radii between those of super-Earths and sub-Neptunes appear to be rare. This 'Radius Valley' was closely investigated via the California-Kepler survey by Fulton et al. [2017], who used a sample of 2025 Kepler planets to study this gap (Figure 2). Since we can observe planets on either side of the valley, it seems unlikely that it originates due to detection limits or biases. Furthermore, a study by Kruijssen et al. [2020] utilised Kepler and Gaia data to show that the radius valley is likely not influenced by the host star's age, metallicity or mass. The cause of the valley is then likely related to the planet itself (with perhaps a slight influence from stellar clustering, as pointed out by Kruijssen et al. [2020]). As such, theories of the formations of super-Earths and sub-Neptunes must be able to account for its existence.

Several mechanisms have been proposed that can account for the radius valley. The first is the stripping of gas envelopes via photoevaporation. At the close orbital distances of the Kepler planets, the irradiance received by a planet is a sizeable frac-

tion of the planet's gravitational binding energy. The UV and X-ray flux from the star is sufficient to strip away the planet's gas layers, possibly leaving the planet's bare rocky core. A study by Owen and Wu [2017] shows that the photoevaporation timescale peaks naturally at a critical envelope mass for which the planet's radius is double that of its rocky core. Planets with such heavy envelopes enjoy long-term stability against photoevaporation. For heavier envelopes, the radius expands further and the evaporation timescale shortens. For planets with lighter envelopes, the radius is dominated by the core radius and the photoevaporation timescale is very short. This leads to an unstable scenario in which the gaseous layers of the planet can be quickly stripped. As such, this theory can account for the lack of planets of intermediate radii, as such planets would have the envelopes driving their larger radii rapidly stripped due to the stellar irradiance.

Alternatively, the core-powered mass-loss mechanism put forward by Ginzburg et al. [2018] can also reproduce the observed radius valley. After dispersal of the protoplanetary disk, planetary cores have temperatures in the range of $10^4$ - $10^5$ K. These hot cores cool by convection, so that energy is transferred to the loosely bound gaseous outer layers. If the cooling luminosity is sufficient, the gas will become unbound and escape from the planet over Myr timescales. However, heavy atmospheres may radiatively cool themselves faster than the rate at which they lose mass, allowing such planets to retain their large gaseous envelopes. In contrast, lighter atmospheres will lose their mass in a shorter timeframe, and this mass loss can drive progressively faster removal of their atmospheres. As shown in related work by Gupta and Schlichting [2019], this reproduces a bimodal population as seen in the observations by Fulton et al. [2017]. Further insights into the nature of the radius valley is clearly tied to the formation and composition of super-Earths and sub-Neptunes.

## 1.3 Composition and Structure

For several planets in the Kepler sample, transit radii combined with estimates of their mass from other observational techniques allows us to estimate their density; from this, conclusions were drawn that super-Earths have densities consistent with a rocky composition and a thin or non-existent atmosphere. Sub-Neptunes have lower densities owing to their significantly larger radii, which is typically explained through a significant $\mathrm{H/He}$ atmosphere that accounts for a few percent of the planet's total mass. Here, I briefly introduce the concept of *volatile species*. These are defined as species which readily vaporize, relative to some standard temperature and pressure (commonly room temperature and 1 bar). Examples of these species include water ($\mathrm{H_2O}$), carbon monoxide and carbon dioxide ($\mathrm{CO}$, $\mathrm{CO_2}$), methane ($\mathrm{CH_4}$), ammonia ($\mathrm{NH_3}$), sulfite ($\mathrm{H_2S}$) and nitrogen ($\mathrm{N}$) [Marboeuf et al., 2014]. In contrast, *refractory species* are those which do not readily vaporize, and instead remain either solid or liquid at standard temperature and pressure. Examples include $\mathrm{Mg}$ and $\mathrm{Si}$, as well as many minerals such as enstatite ($\mathrm{MgSiO_3}$).

## 1.3 Composition and Structure

For a subset of the observed population, small exoplanets appear consistent with an Earth-like composition up to $M = 3M_{\oplus}$ (green line in Figure 3), while on the high radius end we see several planets consistent with hydrogen-rich compositions (solid yellow line). Some examples on the low end include the Trappist-1 planets, while on the high end we see several sub-Neptunes such as TOI-1201b and TOI270c. This would seemingly point to smaller planets having rocky inventories similar to Earth's bulk silicate composition, up towards $\sim$ 1.3 $R_{\oplus}$ and $\sim$ 3.0 $M_{\oplus}$. However, numerous planets fill the gap between these compositions, with planets inconsistent with a broadly Earth-like composition yet likely too small to accrete and retain extensive hydrogen envelopes. While it is harder to isolate a clear clustering around any particular compositions for these middle planets, many are consistent with water-abundant compositions or global magma oceans (blue and purple) [Lichtenberg and Miguel, 2025].

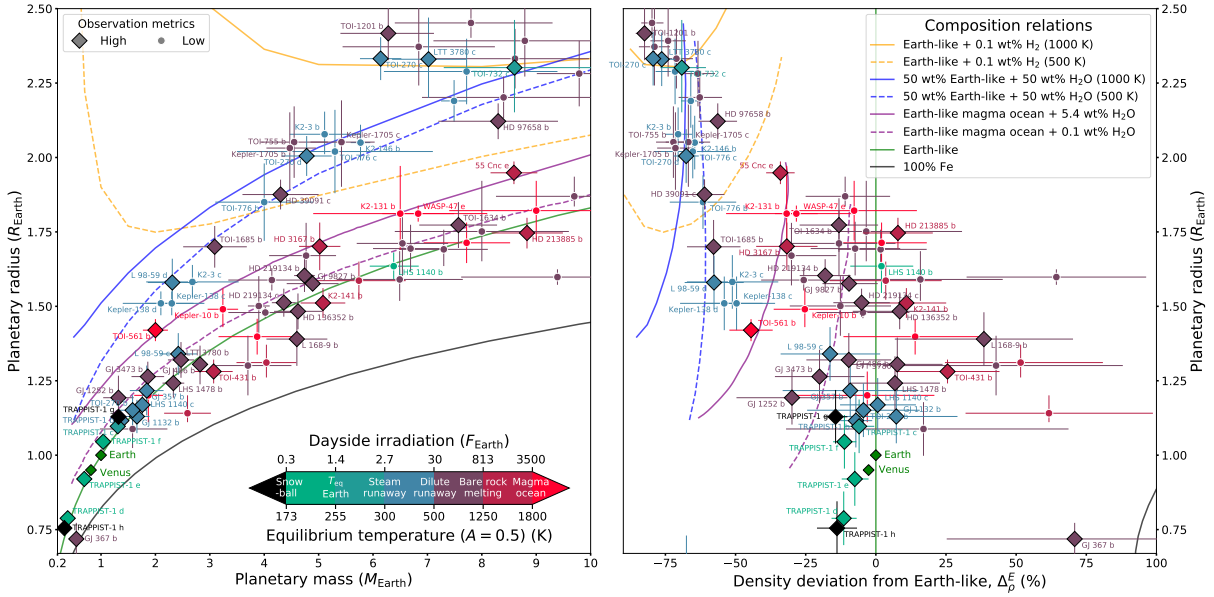


**Figure 3: Clustering of approximately 100 exoplanets around compositional isolines.** Exoplanets with well-constrained radii below 2.5 $R_{\oplus}$ and below 10 $M_{\oplus}$ are shown by mass (**left panel**) and density compared to Earth (**right panel**). Exoplanets are colour-coded with respect to their dayside irradiation, which is linked to a lower limit on their equilibrium temperatures. Coloured lines indicate models of a fixed composition and structure, such as pure iron (black), Earth-like (green), Earth-like with significant water fractions (blue), Earth-like with hydrogen enrichment (yellow) and Earth-like with a global magma ocean (purple). Image taken from Lichtenberg and Miguel [2025]

Both the models of photoevaporation and core-powered mass find that the location of the radius valley shifts depending on the density of the planet's interior. By modelling various interior compositions and comparing the resulting distribution to the radius valley, we can make an inference on the core compositions of sub-Neptunes and super-Earths (Figure 4). These models imply that sub-Neptunes and super-Earths have silicate interiors, with data indicating a silicate-to-iron ratio of $\sim$ 3.1, similar to that of Earth's, in accordance with the trends in Figure 3. This has led to the hypothesis that

these planets form interior to the so-called snow line - the minimum distance from the central protostar in the early solar nebula where conditions allow water to condense into solid grains. This would imply that super-Earths and sub-Neptunes may be separate outcomes for similar planetary embryos; they may originate from the same initial population, but differentiate into either smaller super-Earths or larger sub-Neptunes during their evolution [Bean et al., 2021]. This remains speculative, and other theories have been suggested. For instance, work by Venturini et al. [2020a] illustrates that water-rich sub-Neptunes that formed beyond the snow line could migrate inwards, thereby contributing to the Kepler sample and the radius valley.

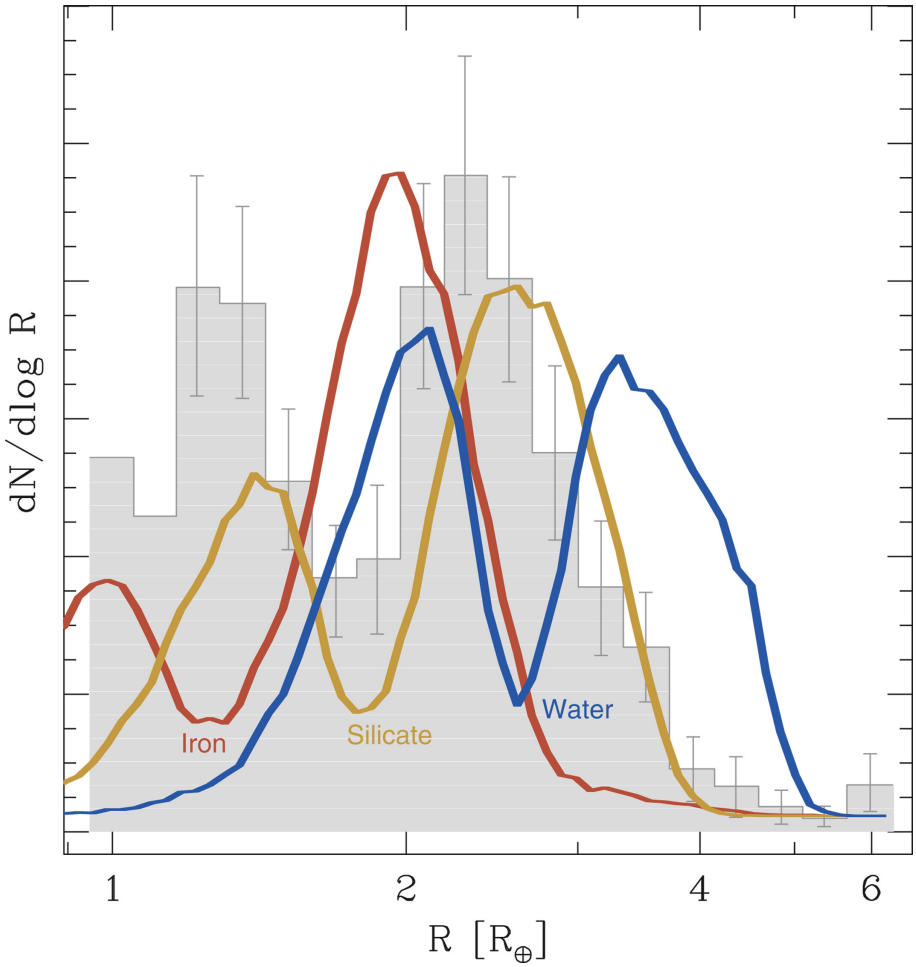


**Figure 4: Radius distributions predicted by photoevaporation models for varying compositions.** The radius distribution of planets in the *Kepler* sample showing the exoplanet radius valley is shown as the grey background. Colored lines represent radius distributions as predicted from photoevaporation models, representing an iron-rich composition (red), rocky composition (yellow) and water-rich composition (blue). Figure adapted from Owen and Wu [2017]

.

With the theory that these planets may have similar rocky inventories, the compositional differences between super-Earths and sub-Neptunes remains uncertain. While

the super-Earths are often assumed to be terrestrial owing to their high densities, sub-Neptunes have several viable characterisations. These include rocky silicate cores overlaid by a thick $\mathrm{H}$ / $\mathrm{He}$ atmosphere as previously discussed, or silicate-ice mixtures in a similar vein to the solar system's ice giants. Other interpretations are "water-worlds", with significant water content (>10% by mass fraction according to Bean et al. [2021]) and lack of a thick $\mathrm{H_2}$ atmosphere. Tied to this is also the concept of a Hycean planet, defined as a temperate ocean-covered world overlain by a thick $\mathrm{He}$ atmosphere by Madhusudhan et al. [2023]. These various interpretations reproduce sub-Neptune masses and radii.

However, it appears unlikely that the current sub-Neptune observational candidates, which are all close-in exoplanets with high equilibrium temperatures, can sustain temperate liquid water oceans beneath their $\mathrm{H/He}$ atmospheres. Innes et al. [2023] note that relatively small pressures of 10 bar under solar irradiation is sufficient to cause a greenhouse effect due to collision-induced absorption by hydrogen in the atmosphere, pushing the liquid water to a supercritical state in which it fully mixes with the overlying atmosphere, forming a miscible supercritical envelope. The presence of water vapour in the atmosphere decreases the runaway greenhouse limit further, requiring these planets to lie far away from the star to sustain temperate water oceans. Modelling by Leconte et al. [2024] supports this view, as they note that the presence of any condensible species heavier than the background gas - such as water against hydrogen - can suppress convection, no matter what the temperature profile within the atmosphere is. By modelling this for a prototype of a temperate sub-Neptune (K2-18b), they show that convection inhibition forms a stable layer in the atmosphere, below which convection is still able to take place. This results in planetary interiors that can be far hotter than previous models indicated, as heat cannot be effectively dissipated. In this view of sub-Neptunes, the interior temperatures are likely high enough to melt their rocky inventories, if they possess any.

As such, the pressures and temperatures in sub-Neptune interiors may lead to a partial or global melting of their rocky inventories, creating a magma ocean covered by the $\mathrm{H/He}$ atmosphere. In such planets, chemical interactions between the atmosphere and the molten rock will drive a variety of reactions that may translate to trends in the atmosphere, possibly allowing remote observations to infer information on the planetary interior [Schlichting and Young, 2022]. Furthermore, such magma ocean planets may be common in our universe throughout the planetary mass and radius regime, being likely outcomes for both super-Earths and sub-Neptunes shortly after formation [Lichtenberg, 2021]. In addition, these planets may represent conditions similar to that of the early Earth, so studies of magma ocean exoplanets may inform us of Earth's early history. As such, magma ocean exoplanets are a valuable point of study for both Earth's history as well as planet formation and evolution models at large. I will delve further into the chemistry of magma ocean exoplanets in this thesis.

## 1.4 Magma-Ocean Exoplanets

### 1.4.1 Formation and Lifetimes

In the context of this work, I refer to a magma ocean exoplanet as any exoplanet with at least a portion of its silicate inventory in a liquid state. There is a distinction between a *global* magma ocean, where the entire surface of the planet is molten, versus a hemispheric or partially molten rocky mantle in which only a portion of the surface sustains a magma ocean.

For super-Earths and sub-Neptunes, which are expected to form with a significant amount of silicates, an initial magma-ocean state is very likely. Ikoma et al. [2018] cites several sources of energy that drive temperatures high enough to form and sustain magma oceans. The first is heat from accretionary impacts, which primarily drives higher temperatures at the planetary surface, and becomes significant for planetary embryos and protoplanets. Figure 5 shows how impactors of varying sizes drive local magma oceans and can cause emulsification of metal cores into the planetary mantle, leading to non-homogenous silicate-iron mixtures in most cases. Second, there is significant heat produced from radioactive decay of radiogenic isotopes. Additionally, as shown in Figure 3, stellar irradiation will be a significant source of energy for many planets, particularly those on close-in orbits. Depending on these sources, magma oceans may form at the planet's surface (impact-driven) or the entire silicate mantle may become molten, especially given sufficiently energetic giant impacts.

Another important source of heat is generated by planetary differentiation. This refers to the accumulation of chemicals in different areas within the planet due to their respective densities or chemical affinities. The Earth, Moon and numerous other objects are so differentiated; the present-day solid Earth is broadly differentiated into its core, mantle and crust. Earth's core is metallic, comprised primarily of monatomic iron and nickel. Its mantle is mostly comprised of *mafic* rock, meaning minerals with high contents of magnesium and iron and relatively reduced silica ($\mathrm{SiO_2}$) content. This includes oxides such as $\mathrm{MgO}$ and $\mathrm{FeO}$; lastly, silicate minerals (molecules composed of $\mathrm{Si}$ and $\mathrm{O}$) make up the bulk of Earth's crust, with $\mathrm{SiO_2}$ being its bulk constituent [Anderson, 1991]. In this thesis, I refer to metals, rocks and silicates in a similar fashion: metals are dense, monatomic species, while I refer to polyatomic compounds of magnesium, silicon and sodium as rocks, with silicates referring specifically to the silicon and oxygen bearing species.

Planetary differentiation partially occurs due to gravitational settling, as denser species will 'sink' and accumulate in lower layers. Chemical affinities of species can further modify this behaviour; elements can be categorized as being siderophile (iron-loving), lithophile (rock-loving) or atmophile (gas-loving) based on the state they preferentially occupy. As such, siderophile elements will readily alloy with metals such as iron, and may differentiate into a denser core alongside these metals [Wood et al., 2006]. The settling of these materials into differentiated layers generates heat that can contribute to the total energy budget to form or sustain a magma ocean [Ikoma et al.,

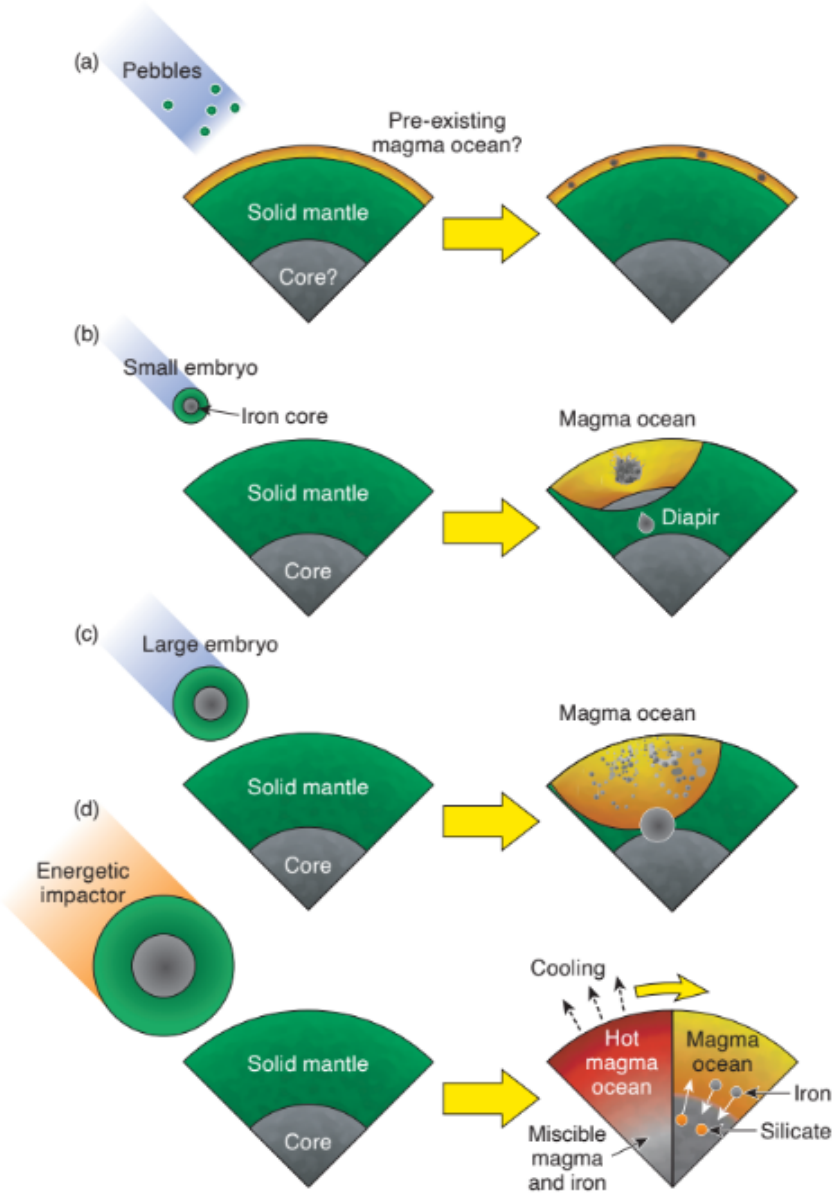


H

**Figure 5: Formation of Magma oceans by increasingly energetic impactors. a:** Small pebbles may not carry sufficient energy to induce magma oceans, but may become emulsified in a pre-existing magma ocean. **b:** Larger embryos carry sufficient energy to form localized magma oceans, and any iron core they carry may then become emulsified. It may sink lower to form a diapir in the planetary mantle. **c:** The energy induced via collision is proportionate to the impactor's mass, so larger embryos will generate larger melt fractions. The degree of emulsification of the metal will be lower as it fractionates and becomes more homogenous with the surrounding magma. **d:** The most massive of impacts may raise the core-mantle temperature high enough for the melt and metal to become miscible, with the two separating only after cooling down. Figure taken from Lichtenberg et al. [2022]

2018].

While the hot, early planet would cool off by means of black-body radiation (in the absence of an atmosphere), there is significant evidence that the formation of rocky protoplanets - whether they become super-Earths or sub-Neptunes - form rapidly, and attain atmosphere-forming volatile elements within that timeframe. This increases the maximum temperatures that these protoplanets can reach, as there is less time for the planet to radiatively cool between accretion events. Furthermore, the presence of $\mathrm{H_2}$ and $\mathrm{H_2O}$ further increases the cooling timescale of these hot planets, because they act as greenhouse gases. Hence we expect rocky planets, with or without extensive hydrogen envelopes, to be largely molten during and immediately after accretion [Lichtenberg and Miguel, 2025].

The longevity of such magma oceans is a function of several parameters. Nicholls et al. [2024] studied the evolution of magma oceans of rocky planets under a variety of parameters, finding solidification time to be parameter sensitive to the planet's orbital distance from its host star, mantle oxidation state (see Section 1.4.3) and atmospheric hydrogen budget. Their modelling finds magma ocean lifetimes of several Myr, with the longest being 90 Myr. The composition of the atmosphere strongly influences the magma ocean lifetime due to aforementioned effects in increasing the cooling time. In any case, the Myr lifetimes of typical rocky-planet magma oceans is a long stretch of time, in which the interactions of the magma ocean with the rest of the planet will play a key role in the planet's further evolution. For sub-Neptunes, the presence of a thick gaseous envelope leads to increased temperatures at the magma ocean surface, allowing the surface to remain molten for far longer. Modelling by Vazan et al. [2018] shows the cooling time of the magma ocean to be a function of envelope mass, with sub-Neptunes with envelopes between 0.5 and 10% of their total mass taking between $1$ and $7$ Gigayears to transition from a magma ocean phase to a solidified state. Some sub-Neptunes may sustain permanent magma oceans if they form within some critical distance from their host star, within which irradiation is high enough to overcome the radiation limit of the planet's primary atmosphere, especially if they contain even small amounts of water given its aforementioned role as a greenhouse gas. Modelling by Hamano et al. [2015] shows that close-in planets with a water endowment above 1% of the planet's mass will sustain magma oceans for as long as it takes for the water to escape from the atmosphere via UV-driven escape, which is on the order of the lifetime of a typical G-class main-sequence star. So for many planets, the magma ocean lasts for up to several Gyrs, and its interaction with the rest of the planet will have a large impact on its evolution and composition.

### 1.4.2 Magma Ocean Geochemistry

A major influence on the overall chemical evolution of magma-ocean planets comes from the potential for the atmosphere and silicate melt to enter chemical equilibrium. The concept of chemical equilibrium is best explained with a short example, such as

with the oxidation reaction of $\mathrm{CO}$ to $\mathrm{CO_2}$:

$$2\,^{(g)}\mathrm{CO} + {}^{(g)}\mathrm{O_2} \rightleftharpoons 2\,^{(g)}\mathrm{CO_2}$$

This reaction can take place in either direction: $\mathrm{CO_2}$ can be formed from $\mathrm{CO}$ and $\mathrm{O_2}$, but it can also dissociate into them. Chemical equilibrium is reached once the forwards and backwards rates of the reaction are equal - irrespective of the amount of products or reactants present initially, the system ends up in a state of balance where the net concentration between the three components remains constant. This is tied to the notion of *chemical potential* $\mu$, the energy absorbed or released for a given species when the particle number in the substance changes. Particles will tend to move from high chemical potentials to lower ones, and will react in such a way as to reduce the free energy in the system; the potential energy minimized in this way is the *Gibbs free energy*, $G$. For a system in chemical equilibrium, the Gibbs free energy is minimized.

On a planetary scale, there is a wealth of reactions that can take place within the atmosphere, within the liquid mantle, or between the two phases. Given the longevity of magma oceans, chemical equilibration between the magma ocean and the overlying atmosphere is likely. For context, it takes Earth's modern day $\mathrm{H_2O}$ ocean only $\sim$ 100 years to equilibrate $\mathrm{CO_2}$ with the atmosphere. Equilibration with a magma ocean is likely even faster, because both the atmosphere and liquid mantle of these planets are highly convective. They therefore cycle their material throughout these reservoirs rapidly, allowing for large quantities of material to chemically equilibrate. This, combined with the longevity of magma oceans, strongly implies that they will reach chemical equilibrium with their atmospheres [Hirschmann, 2012].

Furthermore, chemical equilibration between the mantle and the metal core may also be possible under the right conditions. Metallic cores of the Earth and likely other planetary bodies form as liquid metals separate from the rock, whether this rock is crystallized or is globally molten. This can result in a dense metal core that is differentiated from the mantle, and chemical equilibration may occur so long as the magma ocean has not yet crystallized. Research by Rubie et al. [2003] indicated that equilibration in this case is unlikely, as the lower portions of the magma ocean may crystallize too quickly even as the liquid metal sinks deeper and becomes further inaccessible for equilibration. However, a differentiated metal core is not the only scenario important to consider for metal-silicate equilibration. Lichtenberg and Miguel [2025] notes that gravitational settling of dense metals into a differentiated core is not a straightforward process, as the stresses undergone by metal droplets sinking through the mantle are typically greater than the downwards gravitational force. As mentioned in the previous section and shown in Figure 5, giant impacts of already segregated bodies may induce a global melt in which the metal becomes well-mixed with the mantle, which would allow for large scale equilibration to take place. Lichtenberg et al. [2022] additionally notes that planets substantially more massive than the Earth (those in the super-Earth to sub-Neptune regime) would have sufficient gravitational energy to be homogenous after accretion, leading to a miscible envelope containing the liquid rock and metal. Finally, in sufficiently convective mantles, metals and siderophile elements may be entrained throughout the mantle rather than 'raining out' onto a metal core, which would

likewise allow for metals to equilibrate with the mantle material.

### 1.4.3 Mantle Oxidation State

Of importance to the discussion of atmosphere, mantle and core equilibration is the concept of the mantle oxidation state and oxygen fugacity. The fugacity $f$ of a gas is a measure of its effective partial pressure in a non-ideal treatment, and is tied closely to the chemical potential of that gas. For the purposes of this work, oxygen fugacity ($f_{O2}$) may be thought of as a measure of the effective concentration of oxygen available to react. Meanwhile, the mantle oxidation state refers to the degree of oxidation of polyvalent elements in the mantle, including $\mathrm{Fe}$. The oxygen fugacity is a measure of the mantle oxidation state, as it measures how much oxygen is able to react with polyvalent elements to increase their valence states. In the context of planetary science, oxygen fugacity is frequently cited in reference to a buffer for which the oxygen fugacity is constrained; this thesis makes frequent use of the Iron-Wüstite buffer. This is the oxygen fugacity at which the reaction to form $\mathrm{FeO}$ (Wüstite) from $\mathrm{Fe}$ and $\mathrm{O_2}$ is in equilibrium:

$$\mathrm{Fe^{+0}} + \frac{1}{2}\mathrm{O_2} \rightleftharpoons \mathrm{FeO}$$

Compared to other redox buffers, the Iron-Wüstite (IW) buffer indicates reducing conditions; for reference, Earth's present day mantle is thought to have $f_{O2} = \Delta IW + 3.5$ [Katyal et al., 2020].

The relevance of the oxygen fugacity and the mantle oxidation state is that the mantle oxidation state influences the iron chemistry within the magma ocean. The availability of oxygen to react shifts the balance of chemical reactions in equilibrium towards a given side; for instance, under fugacities above the IW buffer (more oxidizing), $\mathrm{FeO}$ becomes more stable, with it becoming less prevalent for smaller oxygen fugacities (more reducing). This will also impact the distribution and abundances of volatiles in the planet. Many volatiles dissolve readily into the magma ocean, where they may speciate and undergo redox reactions into various other species. The availability of oxygen in the magma ocean will impact the formation of species in the mantle, thus affecting the composition of the atmosphere resulting from mantle evaporation. The mantle oxidation state also influences the metal-silicate partitioning, as experiments show that mantle oxidation state plays a role in impacting the siderophile and lithophile natures of a variety of elements, including $\mathrm{H}$, $\mathrm{C}$ and $\mathrm{O}$, as well as $\mathrm{H_2O}$ [Frost and McCammon, 2008] and various metals [Corgne et al., 2008].

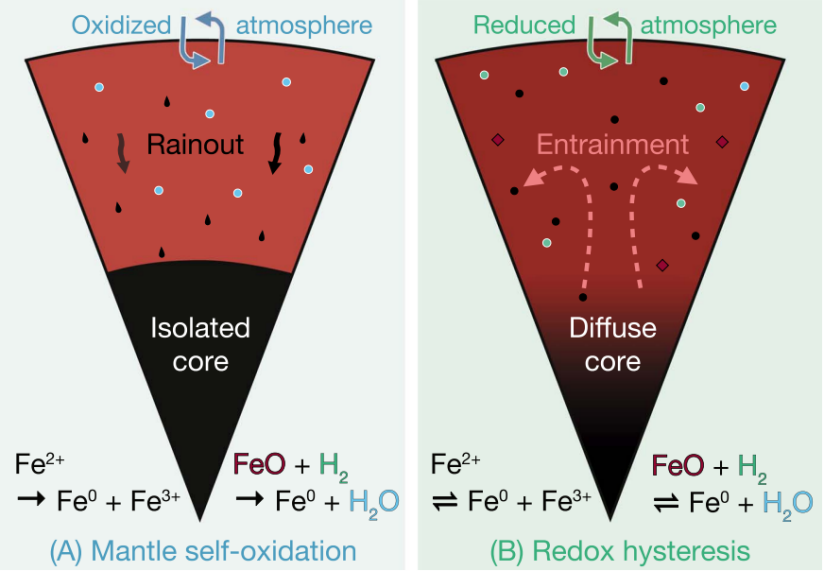


**Figure 6: Schematic representation of two varying degrees of silicate-metal equilibration cases. Left:** metal differentiates into a solid core, causing net oxidation of the mantle and a more oxidized atmosphere. **Right:** mantle is convective enough to entrain metal droplets throughout, leading to a more homogenous system with no strongly differentiated core. The redox reaction between $\mathrm{FeO}$ and $\mathrm{H_2O}$ is shown, which occurs only forwards for the left case, but can occur both ways for the right case. Adapted from Lichtenberg [2021].

The oxidation state of the mantle and the degree to which it equilibrates with the metal is an important factor in the chemical evolution of magma-ocean planets. It is likely that there are significant differences between the interior magma oceans of sub-Neptunes and super-Earths; if for no other reason than that sub-Neptune magma oceans are likely deeper and undergo larger gravitational forces [Vazan et al., 2018]. Figure 6 shows the structures of two magma oceans and illustrates how the reactivity of the core itself can affect the mantle oxidation state, and the nature of the atmosphere. The left magma ocean is not convective enough to circulate liquid metals throughout its mantle, leading to a 'rainout' of metals into a differentiated core. This limits the degree of equilibration and removes $\mathrm{Fe}^0$ from the melt, leading to a net oxidation of the melt. The higher mantle oxidation state can allow for the production of volatiles such as $\mathrm{H_2O}$, and as a result one would expect to observe a more oxidized atmosphere. However, a vigorously convective magma ocean may entrain such iron droplets to form a more homogenous interior, in which large-scale equilibration between the mantle and metals is possible. In this case, the redox reaction forming $\mathrm{H_2O}$ from $\mathrm{FeO}$ and $\mathrm{H_2}$ may occur in reverse, leading to no net oxidation of the mantle. The atmosphere will be more reducing as a result. This brief example showcases how the mantle oxidation state and the degree to which the mantle and core equilibrate are of vital importance to studying these systems in detail [Lichtenberg, 2021].

## 1.5 Aims of this Thesis

A treatment of chemical equilibrium between the molten silicate mantle and atmosphere has been recognized to be a crucial step in understanding the resulting chemistry and structure of exoplanets early in their formation, as global magma oceans are a likely outcome post-accretion. Expanding this view to magma oceans in sub-Neptune interiors allows us to make predictions on their atmospheric compositions, which may be observably verified with present and future instruments such as JWST and Ariel [Benneke et al., 2024]. Such modelling has been undertaken in recent years. In particular, Schlichting and Young [2022] created a chemical equilibrium model that aims to simulate the compositions of the atmosphere, melt and metal core after chemical equilibrium has been reached. In order to account for the possibility of a non-reactive differentiated mantle, they modelled both a 'reactive' case, in which the metal core is able to fully equilibrate with the overlying melt, and an 'unreactive' case in which the core is chemically isolated from the rest of the system.

Schlichting and Young [2022] found that equilibration causes large amounts of lighter material ($\mathrm{H}$, $\mathrm{O}$) to ingress into the metal, with resulting implications for the core densities of the planet. Simultaneously, $\mathrm{H_2O}$ is produced within the melt and outgasses to the atmosphere, forming a volatile-rich atmosphere in most cases that is significantly more oxidized than the initial 99% $\mathrm{H_2}$ atmosphere used in their modelling. The atmosphere is populated by mineral gases, such as $\mathrm{SiO}$, $\mathrm{Na}$, $\mathrm{Mg}$ and numerous volatiles such as $\mathrm{CO}$ and $\mathrm{H_2O}$. These trends all vary with increasing magma-ocean surface temperature, which they modelled from 3500 to 6000 K. They additionally modelled various amounts of initial hydrogen, between 1 and 14% of the planet by weight, to model how varying degrees of hydrogen endowment alters the interior chemistry. The effects of hydrogen endowment are less important than those of the surface temperature, but has implications for observations as the hydrogen budget of a sub-Neptune can in some cases be inferred from the atmosphere alone.

The results from Schlichting and Young [2022] illustrate the large-scale impact that chemical equilibrium has on the chemical makeup of these planets. However, it is likely that numerous parameters beyond the surface temperature significantly alter the chemical trends observed in their research. If we aim to uncover atmospheric trends that may speak to the state of the planetary interior, we must consider a larger range of parameters, to improve the chances of observing exoplanetary systems with conditions that overlap with our modelling conditions. In addition, the chemical model utilized by Schlichting and Young [2022] has seen significant alterations over the passing years, with it now incorporating additional chemical reactions and species, as well as deviations from ideal behaviour added by Young et al. [2023] to facilitate in-depth modelling of Earth's primordial melt-atmosphere equilibration.

The aim of this thesis is to investigate the chemical equilibrium between exoplanetary atmospheres, molten silicate mantles, and metal cores. The interaction between the magma ocean and atmosphere will give rise to unique atmospheric compositions, which may change in response to different interior conditions such as core-mantle equi-

libration temperature and mantle composition. As such, I follow the methodology of Schlichting and Young [2022] but expand the modelling to additional parameters, in order to complement their work and offer a more complete picture of the chemical interaction between planetary magma oceans and atmospheres. Of particular interest are atmospheric trends that connect to the planetary interior, as these may provide a window for current instruments to infer information about conditions that are otherwise inaccessible with remote observations.

This work is structured as follows; in Section 2 I outline the methodology utilised in the model developed by Schlichting and Young [2022] and describe its most important assumptions. In Section 3, I present the modelling results and the influence of various parameters on the atmospheric, mantle and core compositions. In Section 4 I will discuss the implications of these results for the interiors of magma-ocean exoplanets and observations thereof. I will also discuss the key assumptions and limitations of this model, and explore their implications for my results. I summarise and offer some final remarks in Section 5.

# 2 Methods

## 2.1 Reaction Network

To investigate the chemical interaction between the hydrogen atmosphere, the molten silicate mantle and the metal core, I follow the methodology described in Schlichting and Young [2022] (Hereafter abbreviated as SY22), which is described in this section. While I have made significant alterations to their code in an effort to make the model more modular and readable, I adhere closely to the methodology outlined in their work. All python code used in this thesis can be found on the Forming Worlds Lab GitHub page, which is kept up-to-date to reflect the latest changes to the model's code base.

In the model, the planetary chemistry is simulated through a chemical network that is divided into three reservoirs: the atmosphere, the molten silicate mantle, and the metal core. In the following description, I will refer to these as discrete, separate phases, although the boundary between these phases is unlikely to be sharp in reality, as mentioned by SY22 and Lichtenberg and Miguel [2025]. To make the modelling of the chemical equilibration between these phases tractable, a few simplifying assumptions are made:

- The planet neither accretes new material, nor does it lose any material (through atmospheric escape or otherwise),
- The silicate mantle is fully molten,
- The three phases of the planet are in constant chemical contact and reach chemical equilibrium with each other.

The first of these assumptions allows for strong constraints to be placed on the model, as it requires that the amount of material at initialisation is the same as the amount of material at the end of a model run. Realistically, there should be significant escape from the atmosphere, either driven from heat from the interior or from stellar irradiation; I will review the implications of their inclusion in Section 4.

Given the longevity of magma oceans and the effectiveness of chemical equilibration, the second assumption is feasible; chemical equilibrium will likely occur before a fully molten silicate mantle crystallizes, and such full-scale molten systems are imaginable shortly after accretion or given sufficiently energetic impacts thereafter.

The last assumption likely holds for the atmosphere and silicate melt, which are highly convective; as such, the material will be able to circulate quickly enough to effectively bring the full reservoir into chemical contact. The silicate melt and metal core will likely not be in constant or full chemical contact, at least not if the core is differentiated from the melt. As such, the model likely over-estimates the amount of material that is able to equilibrate between the melt and metal core, except for the case where the metal is fully mixed with the molten mantle.

The elements taken into consideration in the model are H, C, O, Na, Mg, Si and Fe. $\mathrm{H}$ is crucial to include as the predominant component of sub-Neptune atmospheres. Meanwhile $\mathrm{O}$ and $\mathrm{Si}$ together compose the bulk of Earth's crust. Combined with $\mathrm{Na}$, $\mathrm{Mg}$ and $\mathrm{Fe}$, a variety of mafic rock and silicates can be composed, which should capture the fundamentals of a molten mantle with a composition resembling that of Earth's rocky inventory. Lastly the inclusion of carbon bearing atmophile species such as $\mathrm{CO}$ and $\mathrm{CO_2}$ further captures useful reactions for the atmosphere-mantle exchange. In the code, species are explicitly labelled as belonging to either the metal core, silicate melt or atmosphere, in order to track in which reservoir they are present. The metal core is more accurately described as an alloy in this model, as it allows for the ingress of $\mathrm{Si}$, $\mathrm{H}$ and $\mathrm{O}$ into the predominantly Fe core.

Firstly in the silicate mantle, the following species are present: $\mathrm{MgO}$, $\mathrm{SiO_2}$, $\mathrm{MgSiO_3}$, $\mathrm{FeO}$, $\mathrm{FeSiO_3}$, $\mathrm{Na_2O}$, $\mathrm{Na_2SiO_3}$, $\mathrm{H_2}$, $\mathrm{H_2O}$, $\mathrm{CO}$ and $\mathrm{CO_2}$.

For the atmosphere, these are $\mathrm{H_2}$, $\mathrm{CO}$, $\mathrm{CO_2}$, $\mathrm{CH_4}$, $\mathrm{O_2}$, $\mathrm{H_2O}$, $\mathrm{Mg}$, $\mathrm{Fe}$, $\mathrm{SiO}$, $\mathrm{Na}$ and $\mathrm{SiH_4}$, all present in the gas phase.

Finally for the metal core the model incorporates $\mathrm{Fe}$, $\mathrm{Si}$, $\mathrm{H}$ and $\mathrm{O}$. This gives a total of 26 species.

To form the reaction network, it is not necessary to exhaustively describe each possible chemical reaction that can take place given these species. The many possible reactions will not be independent of each other, and the full network can be specified by constructing a basis set. Any other possible reactions can be constructed as linear combinations of these basic reactions. For their derivation I will refer readers to the work by SY22, but I provide the basis set of reactions here.

The first seven capture the chemical exchange within and between the liquid mantle and metal core. These include speciation reactions for $\mathrm{Na_2O}$, $\mathrm{MgO}$ and $\mathrm{FeO}$ in the melt:

$$\mathrm{Na_2SiO_3} \rightleftharpoons \mathrm{Na_2O} + \mathrm{SiO_2} \tag{R1}$$

$$MgSiO_3 \rightleftharpoons MgO + SiO_2 \tag{R2}$$

$$FeSiO_3 \rightleftharpoons FeO + SiO_2 \tag{R3}$$

Three redox reactions between oxygen, silicon and iron in the melt:

$$\frac{1}{2}SiO_2 + Fe_{metal} \rightleftharpoons FeO + \frac{1}{2}Si_{metal} \tag{R4}$$

$$O_{metal} + \frac{1}{2}Si_{metal} \rightleftharpoons \frac{1}{2}SiO_2 \tag{R5}$$

$$2\,{}^{(l)}H_2O + Si_{metal} \rightleftharpoons SiO_2 + 2\,{}^{(l)}H_2 \tag{R6}$$

As well as an exchange of hydrogen between the metal core and molten mantle:

$$2\,H_{metal} \rightleftharpoons {}^{(l)}H_2 \tag{R7}$$

In the atmosphere there are three independent reactions, all of which are oxidation and reduction reactions taking place inside the atmosphere:

$$CO + \frac{1}{2}O_2 \rightleftharpoons CO_2 \tag{R8}$$

$$CH_4 + \frac{1}{2}O_2 \rightleftharpoons 2\,H_2 + CO \tag{R9}$$

$$H_2 + \frac{1}{2}O_2 \rightleftharpoons H_2O \tag{R10}$$

Finally, the remaining reactions describe the exchange between the atmosphere and the magma ocean. The first four capture the evaporation of the lithophile elements and iron in the magma ocean:

$$FeO \rightleftharpoons {}^{(g)}Fe + \frac{1}{2}\,{}^{(g)}O_2 \tag{R11}$$

$$MgO \rightleftharpoons {}^{(g)}Mg + \frac{1}{2}\,{}^{(g)}O_2 \tag{R12}$$

$$SiO_2 \rightleftharpoons {}^{(g)}SiO + \frac{1}{2}\,{}^{(g)}O_2 \tag{R13}$$

$$Na_2O \rightleftharpoons 2\,{}^{(g)}Na + \frac{1}{2}\,{}^{(g)}O_2 \tag{R14}$$

The remaining four capture the solubilities of atmospheric gases into the magma ocean:

$${}^{(g)}H_2 \rightleftharpoons {}^{(l)}H_2 \tag{R15}$$

$$^{(g)}H_2O \rightleftharpoons {}^{(l)}H_2O \tag{R16}$$

$$^{(g)}CO \rightleftharpoons {}^{(l)}CO \tag{R17}$$

$$^{(g)}CO_2 \rightleftharpoons {}^{(l)}CO_2 \tag{R18}$$

While this is the reaction network as described in SY22, one additional reaction was added in the years following, which describes the formation of $\mathrm{SiH_4}$ in the atmosphere through the following redox reaction:

$$^{(g)}SiO + 2\,{}^{(g)}H_2 \rightleftharpoons {}^{(g)}SiH_4 + \frac{1}{2}\,{}^{(g)}O_2 \tag{R19}$$

With this system of basis reactions in place, the conditions for chemical equilibrium may be defined. Physically, chemical equilibrium is attained once the forwards and backwards rates of the reactions are equal; while the reactions continue to take place, the overall concentrations of reactants and products will be constant, regardless of the initial quantities of reactants and products. The assumption of a closed-box system is key to this approach.
Mathematically, the condition for equilibrium is that the product of the chemical potential $\mu_i$ of species $i$ with its stoichiometric coefficient in the reaction, $\nu_i$, is zero:

$$\sum_i \mu_i \nu_i = 0$$

To model this in practice, $\mu$ is defined specific to either the atmosphere, mantle or metal phase, and rewritten in terms of the partial molar Gibbs free energy of the species in the reaction:

$$\mu_i = \Delta G_i^o + RT \ln a_i$$

Where $\Delta G_i^o$ is the net Gibbs free energy of the formation of species $i$ at temperature $T$ and 1 bar of pressure, and $a_i$ is the thermodynamic activity of species $i$. This assumption holds if the temperature and pressure at which the reaction takes place is constant, and when the amount of material is specified in terms of moles. $a_i$ may be related to the mole fraction of the species by $a_i = \gamma_i x_i$, with $x_i$ the mole fraction of species $i$ and $\gamma_i$ the activity coefficient. These coefficients capture deviations from ideal behaviour and are often not well known. If all mixing in the model is treated as ideal, $\gamma_i$ = 1 and these equations simplify, but to allow for the inclusion of non-ideal mixing, I make room for $\gamma_i$ in these equations.

In practice, non-ideal behaviour is implemented for $\mathrm{Si}$, $\mathrm{O}$ and $\mathrm{Fe}$ in the model, pertaining in particular to reactions R4, R5, R6 and R7. Their non-ideal behaviour was implemented prior to this work by the model authors in order to model the ingress of light elements into the metal core for the primordial Earth. The description of these activities are found in Young et al. [2023].

Ultimately, equilibrium conditions are defined for each reaction R1 - R19 in the following form:

$$\sum_i \nu_i \ln x_i + \sum_i \ln \gamma_i + \left[ \frac{\Delta G_r^o}{RT} + \sum_g \nu_g (P/P^0) \right] \tag{1}$$

Here, $\Delta G_r^o$ is the net Gibbs free energy of the reaction, $T$ and $P$ are the temperature and pressure at which the reaction occurs, and $P^0$ is the pressure at a standard state (1 bar in this model). The sum over index $i$ applies to all species in the system, while the sum over index $g$ applies only to the gas species. This extra term incorporates pressure effects onto reactions involving gas species, and is constructed by replacing $\ln x_g$ with the product $\ln(x_g P/P^0)$. With this set of equations in place, we have 19 equilibrium equations in terms of 26 mole fractions.

Logically, since a closed-box system is assumed, the amount of each element present in the system is conserved; if we begin our modelling with 1000 moles of hydrogen, we require that same amount to be preserved in our result. Therefore the model contains seven mass-balance equations, one for each element, with the following form:

$$n_e - \sum_k \sum_i \eta_{e,i,k} x_{i,k} N_k = 0 \tag{2}$$

Here, $n_e$ is the number of moles of element $e$ in the system; the sum over index $k$ represents the three phases of the planet; atmosphere, melt or core, while $i$ as always represents the chemical species. Hence, $\eta_{e,i,k}$ is the amount of moles of element $e$ in species $i$ in phase $k$. $x_{i,k}$ is the concentration of species $i$ in phase $k$, and finally $N_k$ is the total amount of moles in phase $k$. As such, the full sum is simply the difference between the amount of moles of element $e$ initially versus the amount of moles of element $e$ at an arbitrary point in the model. It is important to note that the amount of moles in each phase, e.g. $N_{atm}$, $N_{melt}$, and $N_{metal}$ are not constant; their amounts will change as the system tends towards chemical equilibrium. As such, they are treated as variables, giving a system of 19 + 7 = 26 equations in 29 variables.

Additionally, the mole fractions of the species within each phase must sum up to one. For example, $1 - x_{Fe} - x_{Si} - x_H - x_O = 0$ for the metal phase. Hence for each phase $k$, a summing constraint is defined as follows:

$$1 - \sum_i x_{i,k} = 0 \tag{3}$$

Finally, the pressure at the bottom of the atmosphere must be computed for each iteration; this is because equation 1 is based on the assumption that the reaction takes place at a constant pressure, yet the changing composition of the atmosphere will modify the mean molecular weight of the atmosphere and hence the pressure at the interface between the atmosphere and silicate melt. The model solves for the pressure simultaneously with the other equations through the following approximate equation:

$$\left(\frac{P_{surface}}{1\text{bar}}\right) \approx 1 \times 10^6 \frac{M_{atm}}{M_p} \left(\frac{M_p}{M_\oplus}\right)^{2/3}$$

In practice, rather than compute the mass of the atmosphere in grams, the mass fraction of the atmosphere relative to the planet's total mass is calculated, labelled $m_{atm}$, and the pressure is then computed as follows:

$$\left(\frac{P_{surface}}{1\text{bar}}\right) \approx 1 \times 10^6 \frac{m_{atm}}{1 - m_{atm}} \left(\frac{M_p}{M_\oplus}\right)^{2/3} \tag{4}$$

This results in 19 + 7 + 3 + 1 = 30 equations in terms of 30 variables; the 26 mole fractions, the total moles of atmosphere, melt and metal core, and finally the pressure.

## 2.2 Implementation of Equations

The system of equations of this model constitutes an inverse problem; given an initial set of parameters $\theta_i$ capturing the planetary composition (in terms of the mole fractions and moles in each phase), we wish to acquire a new set of parameters $\theta_f$ for which equations 1 2 and 3 are satisfied. In other words, we wish to find the set of parameters that satisfies the conditions for chemical equilibrium. In this section, I outline the strategy put forward by SY22 to find the resulting set of parameters.

First, the net Gibbs free energy of each reactions must be computed at relevant temperatures. The specific Gibbs free energy of formation of compound $i$ can be related to the specific enthalpy $H$ and entropy $S$ as $G_i^o = H^o - TS^o$, with $T$ the temperature. The most straightforward way of calculating this for each relevant species is by computing the specific enthalpy and entropy by means of a Shomate polynomial:

$$H^o = H^o_{298.15} + aT + \frac{bT^2}{2} + \frac{cT^3}{3} + \frac{dT^4}{4} - \frac{e}{T} - h \tag{5}$$

$$S^o = a \ln t + bt + \frac{ct^2}{2} + \frac{dt^3}{3} - \frac{e}{2t^2} + g \tag{6}$$

These are empirical formulae to compute the standard state molar enthalpy $H^o$ and entropy $S^o$ at 1 bar of pressure at temperature $T$, with $t = T/1000$. Coefficients $a, b, c, d, e, f, g, h$ are empirical coefficients, and $H^o_{298.15}$ is the standard enthalpy for the species at a reference temperature. If data on the empirical coefficients is available, the Gibbs free energy is easily computed at the desired temperature. For the majority of the species incorporated in this model, data is available through the NIST database, for either the gas-phase thermochemistry, condensed-phase thermochemistry, or both. In most cases, data is available between temperatures of no lower than 298 K, and no higher than 6000 K.

Given the standard molar Gibbs free energy of the formation of the pure species, one can compute the *net* Gibbs free energy of a reaction through simple subtraction of the reactants and products of the reaction. Taking reaction R8 as an example:

$$\Delta G^o_{r8} = G^o_{CO2}(T) - G^o_{CO}(T) - 0.5 G^o_{O2}(T)$$

. However, NIST data is not available for all species in the required phases. The authors of the original model computed values based solely on empirical data from NIST for reaction 3 and reactions 8-14. For the remainder, they combined values computed from NIST data with data from other works; for details I refer to the Appendix of SY22 and references therein to Fegley and Cameron [1987], Badro et al. [2015], Hirschmann et al. [2012], Okuchi [1997], Moore et al. [1998] and Pan et al. [1991].

The dependency of temperature on the Gibbs free energies of these reactions raises an important question; at which temperature do these reactions take place? Realistically, both temperature and pressure will vary with depth in the atmosphere and silicate mantle; however, these equations must be solved at a set temperature and pressure. One could subdivide the planet into vertical layers and ascribe varying temperatures to each according to theoretical temperature profiles, but doing so is beyond the scope of this work. Instead, the model utilises two distinct temperatures which are used to compute the Gibbs free energies of the reactions.

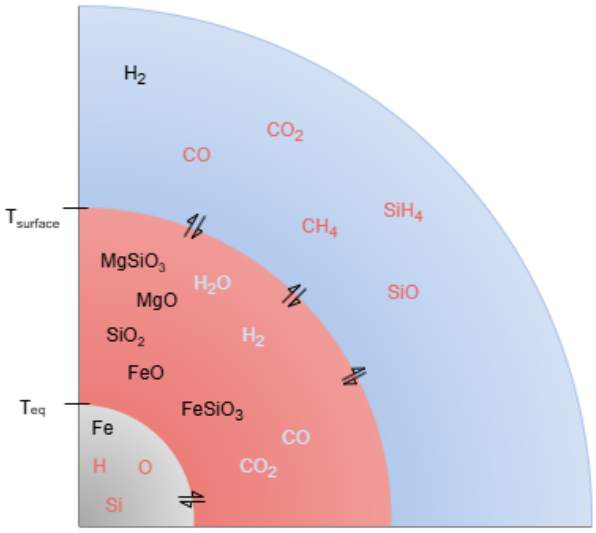


**Figure 7: Schematic of a simplified layered structure for a model planet**. The phases of the planet are highlighted in blue (atmosphere), red (silicate melt) and grey (metal core). Several species present in the phases are indicated, either in black if they are native to the phase or in a corresponding colour if they undergo exchange between phases.

Figure 7 shows a simplified schematic of the interior structure of a model planet. Exchange between the metal core, silicate melt and atmosphere happens at two interfaces; the first forms the core-mantle interface, and the second the boundary between the melt and the atmosphere. Reactions take place under one of two temperatures; the *surface temperature* $T_{surface}$ is defined as the temperature at the interface between the atmosphere and the silicate melt. As this temperature is varied, I expect to see significant differences in the overall composition of the melt and atmosphere, as this temperature is critical to the degree of evaporation of the melt as well as the degassing of the atmosphere into the liquid. In addition, I define the *core-mantle equilibration temperature* $T_{eq}$ as the temperature at the core-mantle boundary. Reactions R4 - R7, the

partitioning reactions between the silicate mantle and the metal core, take place under this temperature. Given the increased depth compared to the mantle-atmosphere boundary, I require that $T_{eq} > T_{surface}$. These temperatures are important input parameters on the model, and I do not model cases where the core-mantle equilibration temperature is lower than the surface temperature.

It is crucial to note that while figure 7 suggests a layered structure for the planet, the model in fact makes no assumptions about the planet's structure whatsoever. It merely tracks the molar compositions of the three distinct reservoirs. For example, the model does not distinguish between metallic iron located in a differentiated core or suspended in droplets entrained throughout the magma ocean, as in Lichtenberg [2021]. This view of a more homogenous mantle would have implications for the core-mantle equilibration temperature, which should not be uniform in this situation.

With the Gibbs free energies computed and calculating the atmospheric pressure through equation 4, equation 1 (chemical equilibrium) can be evaluated for reactions 1 - 19, equation 2 (mass balance equations) can be evaluated for all seven elements comprising the model, and equation 3 can be evaluated for the three phases: the atmosphere, silicate mantle and metal core. As previously stated, these variables can be summarized in a parameter vector $\theta$: it contains the individual mole fractions of each species, the number of moles in each of the three phases, and the atmospheric pressure for a total of 30 variables. The goal then is to find values for these parameters that satisfy the equations for chemical equilibrium. This constitutes an inverse optimisation problem, which can be quantified through a cost or objective function, $f(\theta)$. This function quantifies how much a given parameter vector $\theta$ deviates from equilibrium. If $\theta_f$ is a hypothetical set of variables that perfectly satisfies equations 1 - 3, it should evaluate $f(\theta_f) = 0$. The goal is therefore met by minimizing the objective function. For each set of variables considered, the objective function is evaluated and a new set of variables $\theta_i$ is considered which evaluates progressively lower values of $f(\theta)$.

The domain of the objective function is formed by the vector $\theta$ containing the 30 model variables; as such, the parameter space is extensive and minimising the objective function is no small task. To start, we consider the prior distribution of the model parameters. Every variable must be real and non-negative, and mole fractions must clearly be between 0 and 1, exclusive. The strategy employed by SY22 is to approximate the global minimum of the objective function, and obtain the most probable composition satisfying chemical equilibrium via Markov-Chain Monte Carlo sampling.

## 2.3 MCMC Sampling

Generally speaking, the aim of an MCMC sampler is to draw samples from a complicated probability density using an array of independent Markov Chains. Each of these chains has a slightly displaced position, and probabilistically moves from one state to the next. The goal of these methods is to construct a Markov Chain that can quickly move towards a region of interest, after which samples can be collected around this stationary distribution. There are various different algorithms that govern how the Markov

Chain moves from state to state; the most general being the Metropolis-Hastings algorithm. This model utilizes a so-called 'Stretch-Move' algorithm, developed by Goodman and Weare [2010] and is described in the context of the python package emcee by Foreman-Mackey et al. [2013].

Each chain, or 'walker', starts with an initial parameter set $\theta$ containing the model variables. The walker then considers a new set of variables within the allowed prior distribution and considers 'moving' to this new position based on some probability. In this case, the probability is defined such that the walkers will prefer parameter sets which evaluate smaller and smaller values of the objective function. The posterior probability function on which the walkers advance is defined via a prior and likelihood function, as follows:

$$P(\theta_i) = \begin{cases} 0 & \text{if } \theta_i < 0 \\ 0 & \text{if } \theta_i > 1 \text{ for i} \in [1, 26] \end{cases} \qquad \text{(prior)}$$

$$\mathcal{L}(\dagger|\theta) = \frac{y^* - y(\theta)}{2{\sigma_y}^{*2}} \qquad \text{(likelihood)}$$

Here, $\theta$ represents the parameter vector that contains the 30 model variables. A flat or uninformative prior is used, which prescribes a probability of zero if any of the parameters becomes negative or when any of the 26 mole fractions becomes greater than one. The likelihood function is constructed via three vectors $y^*$, $y(\theta)$ and $\sigma_\theta$. $y^*$ are the expected values of the equations 1, 2 and 3 for equilibrium. $y(\theta)$ are the values of these equations evaluated over the parameters in $\theta$. Lastly, $\sigma_y$ is a blanket uncertainty on $y^*$ chosen by hand. The logarithms of these functions are taken and combined into the posterior probability function that is passed to the MCMC sampler.

An ensemble of 200 walkers is constructed, whose initial positions are based on an initial vector $\theta$, but shifted by a small random amount. This way, each walker has an independent position, allowing the full ensemble to sample a broader region in the parameter space. The walkers are advanced initially by 500 iterations, in which they rapidly move towards regions in the domain of higher probability. This is referred to as a *burn-in* run. After these initial steps are finished, the drawn samples of the burn-in run are discarded, and additional samples can be obtained. Once all walkers have finished a desired number of iterations, the sample with the highest posterior probability is retrieved. This MAP result (*maximum a posteriori*) is taken as the final result.

Probabilistic approaches such as MCMC sampling face several challenges; perhaps most relevant for the purposes of this model is how sensitive the MCMC sampler is to the initial position of the walkers. For a small domain in which the global minimum of a function is isolated, a walker would likely quickly move towards the minimum. But the domain of the objective function is extensive, and contains a large amount of local minima in which the walkers can become 'trapped'. To illustrate this, figure 8 shows the value of the objective function $f(\theta)$ for 20,000 random parameter sets $\theta$, which is only a small portion of the objective function's full domain. Between these parameter

sets, fluctuations of several orders of magnitude are expected in the objective function, creating a landscape of numerous local extrema. The walkers may therefore end up in a local region of high probability, that is not necessarily close or representative of the true global minimum. As a result, samples drawn from these walkers will not represent compositions that satisfy chemical equilibrium. Once the walkers are stuck in these regions, it is futile to run additional samples. To avoid this problem, the global minimum may be approximated first using Simulated Annealing.

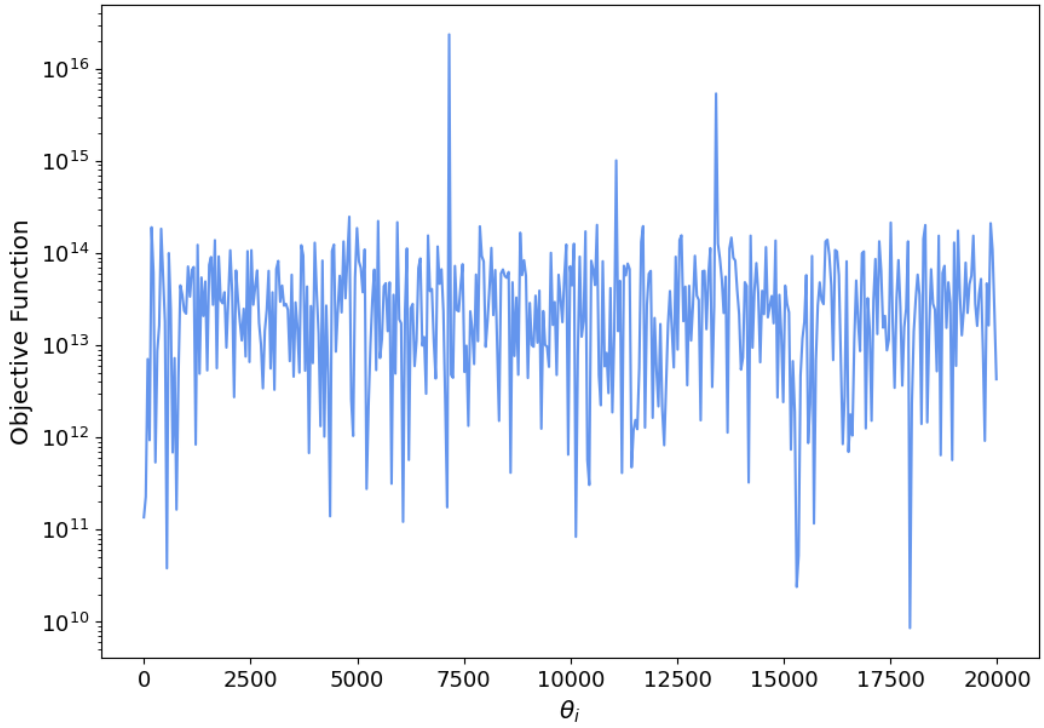


**Figure 8: Fluctuation of the objective function for 20000 different parameter sets**. Each parameter set $\theta_i$ contains the 30 model parameters, each of which takes a random value within the prior distribution. The value of the cost function varies drastically between various parameter sets, creating a parameter space with a large amount of local extrema.

### 2.3.1 Simulated Annealing

In cases such as these where the function domain is very broad, slow but precise root-finding algorithms are not feasible. Likewise, the abundance of local minima in the search space can cause local search strategies to fail. Simulated Annealing is a probabilistic technique that can be applied in this case to approximate the global minimum. It works by starting in an initial state $s$ for which the cost function is evaluated. A random neighbour state $s^*$ is then likewise evaluated and the algorithm probabilistically decides whether to stay in state $s$ or move to the new state based on the difference in the value of the objective function for said states, eg. $\Delta E = e - e^*$. Over time, the algorithm will

move to states with progressively smaller values of the objective function. The probability of moving to a new state $P(e, e^*, T)$ is governed by the values of the objective functions in the states and a global parameter $T$ called the 'temperature' of the annealing algorithm. $P$ is positive even when $e^* > e$, such that the algorithm may move to a 'worse' solution even if its current state is more favoured. These 'uphill' moves allow the algorithm to escape local minima whereas a simpler heuristic technique would get stuck there. The probability of accepting an uphill state decreases as $T$ decreases; for $T = 0$, the algorithm will only accept downhill solutions. A simulated annealing search will therefore begin with a very high temperature, allowing the algorithm to explore a wide stretch of the parameter space. At each iteration, the temperature is decreased according to some annealing scheme, causing the algorithm to progressively favour downhill solutions until it exclusively travels downhill once $T = 0$.

SY22 uses an implementation of *dual annealing* from the SciPy library, which combines a classical simulated annealing method with a so-called Fast Simulated Annealing (FSA) method, which allows for greater 'jumps' between states. In practice, one can only obtain an estimate of the global minimum using this approach, as the time needed to obtain a precise solution is impractically large. To help this process, the elements of the objective function are scaled by hand-tuned weight parameters and a sigmoidal penalty function, which bloats the value of the objective function element if the value of that element falls outside of an accepted tolerance. These tolerances are 1 for 1 for reactions 1 - 19; 0.01 for 2 for the mass balance of the elements and 0.005 for 3 for the summing of the mole fractions for each of the three phases. By doing so, the total value of the objective function becomes far larger for states that do not satisfy equilibrium, allowing the simulated annealing algorithm to move towards regions of lower objective functions faster.

In practice, the simulated annealing algorithm is ran for a set number of iterations, and the resulting vector $\theta_{SA}$ is passed to the MCMC sampler. The walker ensemble takes this parameter set as the initial position, and the chain then advances from this position as normal. By applying simulated annealing in this way, the walker ensemble begins drawing samples from a region much closer to (or already in) the global minimum, and samples drawn from there will be representative of compositions that are close to or at chemical equilibrium. I draw an abundance of samples from this region for several reasons. First, it allows for more robust statistical checks to be placed on the performance of the MCMC algorithm, on which I will elaborate below. I also plot the distribution of the highest posterior probability samples for individual variables. This shows the shape of the posterior distribution that I aim to sample and provides a visual comparison of the MAP sample compared to the underlying posterior distribution. Figure 9 shows such histograms for the mole fraction of $\mathrm{H_2}$ in the atmosphere and the total number of moles comprising the silicate melt.
Estimates on the uncertainties on the MAP parameters may be obtained in two distinct ways: computing the standard deviation of the 500 highest probability samples, and computing the 16th / 50th / 84th percentile values for each variable. It is notable that the MAP value for a variable should be comparable to the mean and the distribution of

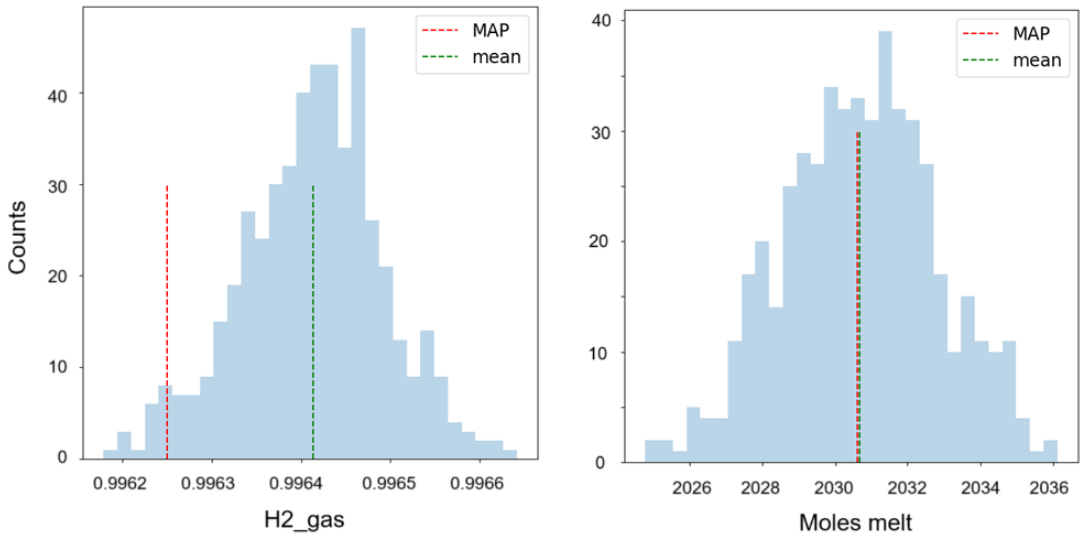


**Figure 9: Distributions of highest posterior probability samples after converged MCMC search.** Shown are histograms from the 500 highest probability samples for the mole fraction of $H_2$ in the atmosphere (left) and the total number of moles comprising the silicate melt (right). The variable's value in the MAP sample is indicated in red, whereas the green line denotes the mean value for the variable across the samples.

values around the mean should be symmetric for the first method to be a fair uncertainty on the MAP result.

## 2.4 Judging convergence

Judging the convergence or performance of any algorithm can be a difficult task. One tool I utilise is a visual inspection of the final samples. As seen in figure 9, I create histograms of the 500 highest probability samples and examine the shape of the resulting distribution for the individual variables. For the examples given, the samples lie in a Gaussian-like distribution in a tight range around the mean value, which can indicate that the chains have converged to a region of high probability. Note that the MAP result does not necessarily coincide with the mean of this distribution; the MAP value for each parameter is drawn from a singular sample that has the overall highest probability, and therefore some variables will have MAP values that diverge strongly from the mean. Since the posterior distributions in these histograms are additionally not always symmetric, this makes it unfeasible to use the standard deviation of these distributions as an uncertainty on the MAP results.

Several statistics can be calculated to further investigate the performance of a model run. The first is the *acceptance fraction* $a_f$. Each time a new position for the model parameters is proposed to one of the (independent) walkers in the ensemble, it is accepted or refuted based on the probabilities as defined by the likelihood and prior of the model. The acceptance fraction is the fraction of proposals that are accepted

[Foreman-Mackey et al., 2013]. If $a_f \approx 0$, none or very few proposed steps are accepted and the sampling will not be representative of the target density. Conversely, if $a_f \approx 1$, nearly all steps are accepted and the chain takes a random walk without considering the target density. The mean acceptance fraction is computed after each run of the MCMC search, and runs with acceptance fractions lower than 0.1 or exceeding 0.6 are treated with suspicion. The likelihood function's error vector $\sigma_{y*}$ can be relaxed to increase the acceptance fraction.

Second, I apply a *Gelman-Rubin statistic* on each variable. If the MCMC search converges, I would expect that the parallel walkers all arrive and sample the same stationary target distribution. After a sufficient number of steps, it should not matter which walker is sampled, and they should become indistinguishable. This can be inspected by comparing the variance within each walker with the variance between all walkers in the ensemble. In practice, I define for each variable $\theta_i$ a Gelman-Rubin statistic computed as follows:

$$R(\theta_i) = \frac{\frac{L-1}{L}W(\theta_i) + \frac{1}{L}B(\theta_i)}{W(\theta_i)} \tag{1}$$

Where $W$ is the mean variance within the walkers, $B$ is the variance between walkers, and $L$ is the length of the chains after the initial burn-in of the ensemble sampler. I calculate the statistic separately for each variable in the model. One can see that as $L \to \infty$ and $B \downarrow 0$, $R$ will tend to unity.

In theory, one could run the walker ensemble until $R$ approaches 1 to within some tolerance. However, work on MCMC methods by Flegal et al. [2008] notes that the Gelman-Rubin statistic is prone to running chains that are either too short or too long. To avoid wasting time on unnecessary iterations or risk obtaining unusable samples, I therefore use these statistics as an additional check on the model. I treat a run where one or multiple variables show poor Gelman-Rubin statistics (outside the range of 0.9 - 1.1) with suspicion, in a similar manner to the acceptance fraction.

Finally, following the methodology of SY22, I calculate a simple statistic, analogous to a reduced $\chi^2$ statistic, based on the difference between the most probable result from the MCMC search, and the expected equilibrium values for each reaction, the mass balance of elements and the constraints on the mole fractions of each phase. If the modelling converges to a solution that satisfies chemical equilibrium, this statistic will be smaller than one. In practice, I monitor its value throughout a grid search and flag any runs whose statistic exceeds unity. Additionally, I compute the value of the objective function using the MAP variables. I deem values around 1.0 to be acceptable given the wide parameter space the model considers.

These statistics can be used to track the performance of the model, even if they cannot be used as a condition to stop further iterations. 'Bad' runs may stem from the random walkers essentially getting stuck in a series of local minima rather than converging towards the global minimum, leading to a poor result once the desired number of iterations has been reached. Model runs flagged as having poor statistics can be re-run with a larger number of iterations for the simulated annealing phase, which can help the new run converge towards the true global minimum. The follow-up MCMC search may then provide a more realistic result.

## 2.5 Unreactive Core Modeling

In order to investigate the result of a metal core that is chemically isolated from the rest of the system, I modify the objective function to exclude all reactions taking place between the silicate melt and the metal core; these are reactions R4, R5, R6 and R7 in the reaction network. I also exclude Equation 3 from the system, so that the entire metal core reservoir is effectively excluded from the model. As a result, I have a reduced system of 25 equations in 25 variables, with the metal mole fractions $x_{Fe}$, $x_{Si}$, $x_H$, $x_O$ and $N_{metal}$ excluded from the parameter vector $\theta$.

Equation 4 is calculated by maintaining the initial metal core composition from the input file and using it to calculate the atmospheric mass fraction at each step. This fraction will now only change in response to equilibration with the mantle, and not the entire planet. Similarly, any final results computed after the MCMC search has concluded will take the metal core composition directly from the input file when needed for computation.

## 2.6 Model adaptations

In this work I closely adhered to the methodology outlined in SY22. The original model may be run by specifying the initial conditions and configurable parameters in a single input file that is passed to a single script containing the full model, which then outputs a single output file. The output file contains the MAP parameters, further results derived from them, and the equilibrium constants of the 19 reactions. The input file is then appended to the output file for convenience. I have largely followed this methodology, but have spent considerable effort to rewrite and improve the code in several areas. In particular, my adaptations aim to make the code more modular, readable, flexible and efficient.

To this end, I have divided the original singular model script into various subscripts with clearly defined tasks, making it easier to modify individual segments of the model - such as the thermodynamic calculations or activity coefficients $\gamma_i$. A simple but flexible logging system has been implemented to track performance throughout individual model runs, as well as throughout multiple runs over larger parameter spaces. I have implemented the option to enable or disable non-ideal mixing as well as the reactivity of the metal core through boolean parameters in the model configuration file. In an effort to further investigate the model's performance, I have implemented two methods of estimating uncertainties on the model's results, on which I elaborate below. Finally, I have attempted to provide robust documentation of the various functions and methods utilized in the model, to make it easier to understand, modify and interpret.

The work put into these improvements have aided the sustainability and accessibility of the model, which can open the door to utilizing this code to further investigate the coupled chemical evolution between the atmosphere, mantle, and core of hot young exoplanets. Although the model is currently not coupled to any larger interior-

atmosphere framework for exoplanet modelling, this remains an option for future work. As mentioned before, the latest commit of the model version utilized in this thesis is publicly available on the Forming Worlds Lab GitHub page.

# 3 Results

## 3.1 Convergence Criteria

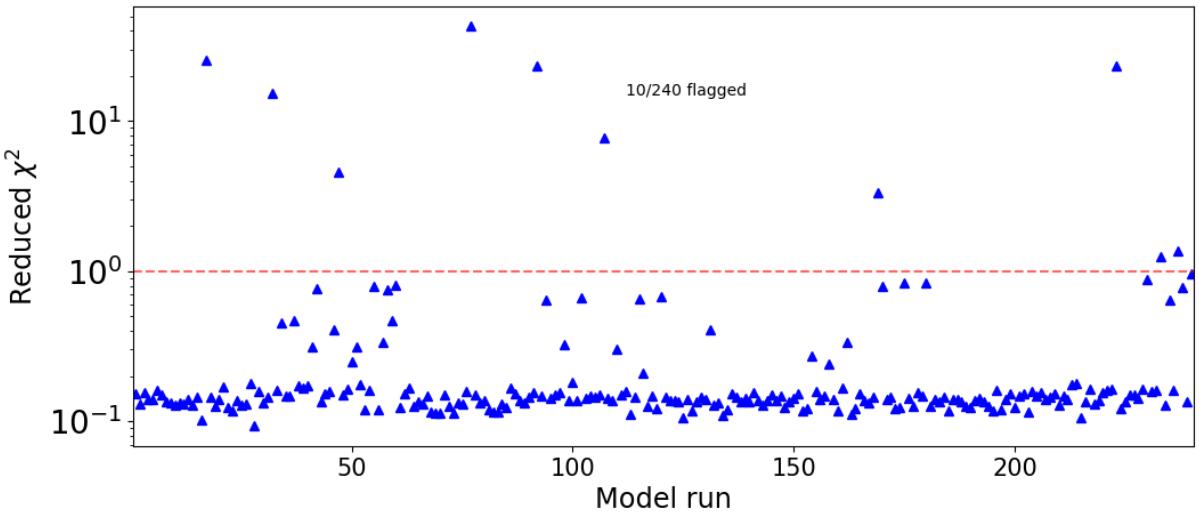


**Figure 10: Reduced $\chi^2$ statistic across 240 model runs**. Models with a statistic exceeding unity (red line) are flagged and may be re-run under different parameters. Converged runs tend to have a mean statistic of $\approx 0.19$.

I have performed over three hundred runs of this model to investigate the effects of various parameters on the overall equilibration of the planet. This includes the surface temperature, equilibration temperature, planet mass, planet composition and the incorporation of non-ideal mixing. In each model run, I allow for 50,000 iterations of Simulated Annealing and draw 300,000 samples in an ensemble of 200 walkers before obtaining the MAP parameter set. Throughout I monitor the model's runtime, reduced $\chi^2$ statistic, mean acceptance fraction $a_f$ and Gelman-Rubin statistics for each variable. Figures 10 and 11 show the former two statistics across 240 model runs. My criteria for convergence are $\chi^2 < 1.0$, $0.1 \leq a_f \leq 0.6$ and Gelman-Rubin statistics between $0.9$ and $1.1$. Runs whose statistics do not satisfy these criteria are flagged and can be rerun with more iterations. Datapoints owing from runs with poor statistics are marked as crosses in most figures, in order to accurately represent my results but maintain clear and interpretable trends where possible. Gelman-Rubin statistics are not shown here, but typically fall within the accepted range when the $\chi^2$ statistic and acceptance fraction indicate a converged run. The Gelman-Rubin statistics are shown for each variable in Appendix A (Figures 32 - 34).

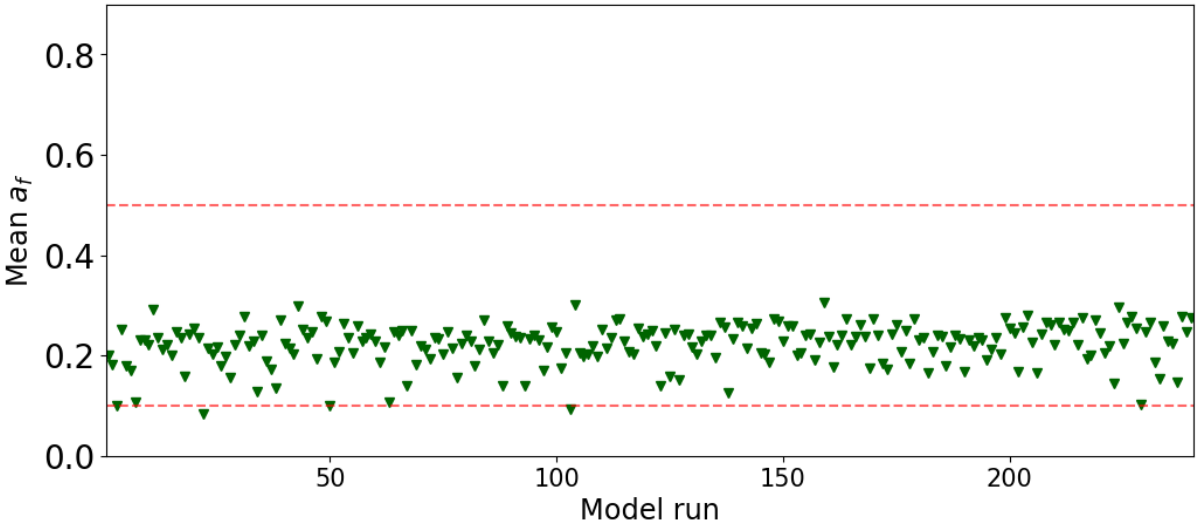


**Figure 11: Mean acceptance fraction $a_f$ across 240 model runs**. The MCMC sampler tends towards low acceptance fractions; runs whose acceptance fraction falls below 0.1 are flagged, but are not re-run if their statistics indicate the MAP to satisfy chemical equilibrium.

## 3.2 Chemical equilibration of cores, mantles and atmospheres

To allow for comparison to the results of SY22, I model a planet of 4 $M_\oplus$ with a thick primary atmosphere consisting of 99.9% $\mathrm{H_2}$ and 0.01% $\mathrm{CO}$. The mantle composition is 92.11% $\mathrm{MgSiO_3}$, 3.2% $\mathrm{MgO}$, 0.1% $\mathrm{SiO_2}$, 0.05% $\mathrm{FeO}$, 0.05% $\mathrm{FeSiO_3}$, 0.7% $\mathrm{Na_2O}$, and 0.1% $\mathrm{Na_2SiO_3}$, with small amounts of $\mathrm{H_2}$, $\mathrm{H_2O}$, $\mathrm{CO}$ and $\mathrm{CO_2}$ making up the remainder. The core is composed of 99% $\mathrm{Fe}$ with trace amounts of $\mathrm{Si}$, $\mathrm{O}$ and $\mathrm{H}$. The initial amount of moles are 1448 for the atmosphere, 2000 for the mantle, and 1250 for the core. This corresponds to a planet that is approximately 1% $\mathrm{H_2}$ and 25% $\mathrm{Fe}$ by weight. In these runs, I incorporate nonzero activity coefficients for $\mathrm{Si}$ and $\mathrm{O}$, as well as non-ideal mixing for water in the melt.

In SY22, the influence of chemical equilibration between the three phases was investigated for surface temperatures ranging from 3500 to 6000 K and hydrogen mass fraction from 1 to 14% of the planet's total mass. To investigate the influence of more parameters, I additionally vary the equilibration temperature $T_{eq}$ to be either 1000, 2000 or 3000 Kelvin above the surface temperature, and explore comparatively colder surface temperatures than those considered in SY22.

### 3.2.1 Effect of surface temperature

First, I examine the effects of the surface temperature $T_s$ on the planet's composition after chemical equilibrium is reached. I vary the surface temperature from 1000 to 2800 K, with a constant equilibration temperature $T_{eq} = 3000$. Equilibration of the three reservoirs causes compositions of the atmosphere, mantle and core to change, as

well as the total amount of moles in each phase. The latter is shown in figure 12, which shows the total amount of moles in each phase in the left panel. As the surface temperature is increased, the 'size' of the metal and melt phases slightly increase at the detriment of the size of the atmosphere.

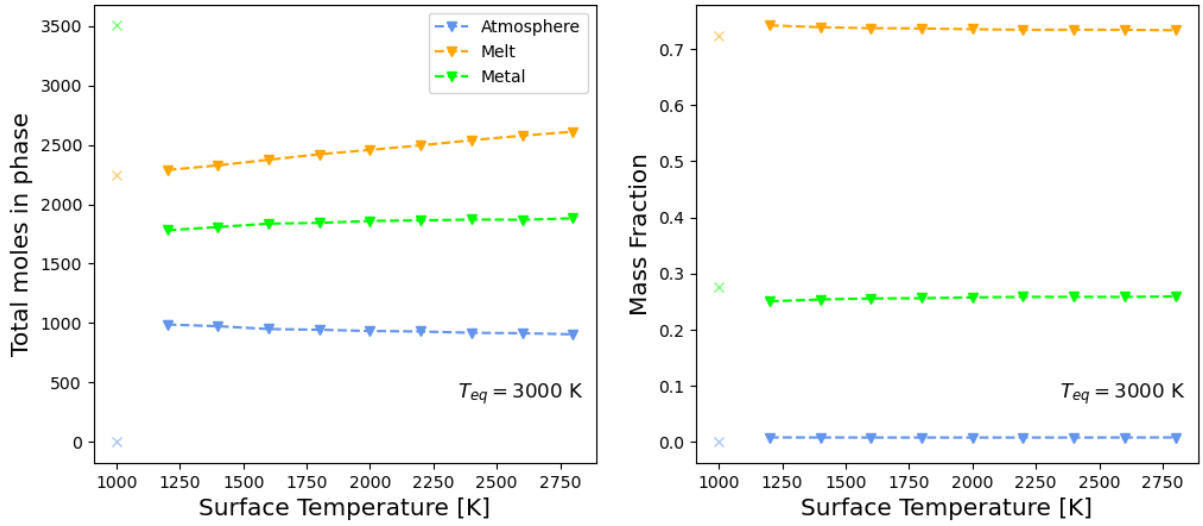


**Figure 12: Relative sizes of atmosphere, melt and metal phases**. The variation with increasing surface temperature is shown for the total number of moles in each phase (**left**) and the mass fraction of each phase relative to the total mass of the planet (**right**). Model planet mass is $4M_{\oplus}$, and the initial amounts of hydrogen and iron correspond to approximately 1 and 25 % of the planet's mass respectively.

Note that while I initialized this model with $N_{atm} > N_{metal}$, immediately after equilibration the metal reservoir is larger in terms of moles than the atmosphere. It is important to stress that the total amount of moles across all three phases (That is, $N_{total} = N_{atm} + N_{melt} + N_{metal}$) is not conserved; and at $T_s = 2800$ K I seem to have over 5000 moles in total, whereas I initialized the model with only 4698 moles. This is because the moles vary according to the stoichiometry of the reactions in the network. For example. reaction R7 describes the exchange of molecular hydrogen and atomic hydrogen between the mantle and metal core:

$$2\,\mathrm{H}_{\mathrm{metal}} \rightleftharpoons {}^{(\mathrm{l})}\mathrm{H}_2 \tag{R7}$$

If this reaction occurs from right to left, it results in each mole of $\mathrm{H}_2$ being counted as two moles of $\mathrm{H}$; hence the total amount of moles across all phases may be higher than one might expect. Inspecting the molar sizes of these reservoirs is a decent first step in estimating which reservoirs are most enriched through the equilibration.

I investigate the effects of the surface temperature on the mass fractions of each reservoir; that is, the total mass of the phase relative to the total mass of the planet, plotted in the right panel of figure 12. The increased amount of moles in the melt and metal reservoirs appear at a glance to have a negligible effect on their mass fractions. The planet remains consistently made up of roughly 74% mantle, 25% metal and a thin

atmosphere comprising roughly 1%.

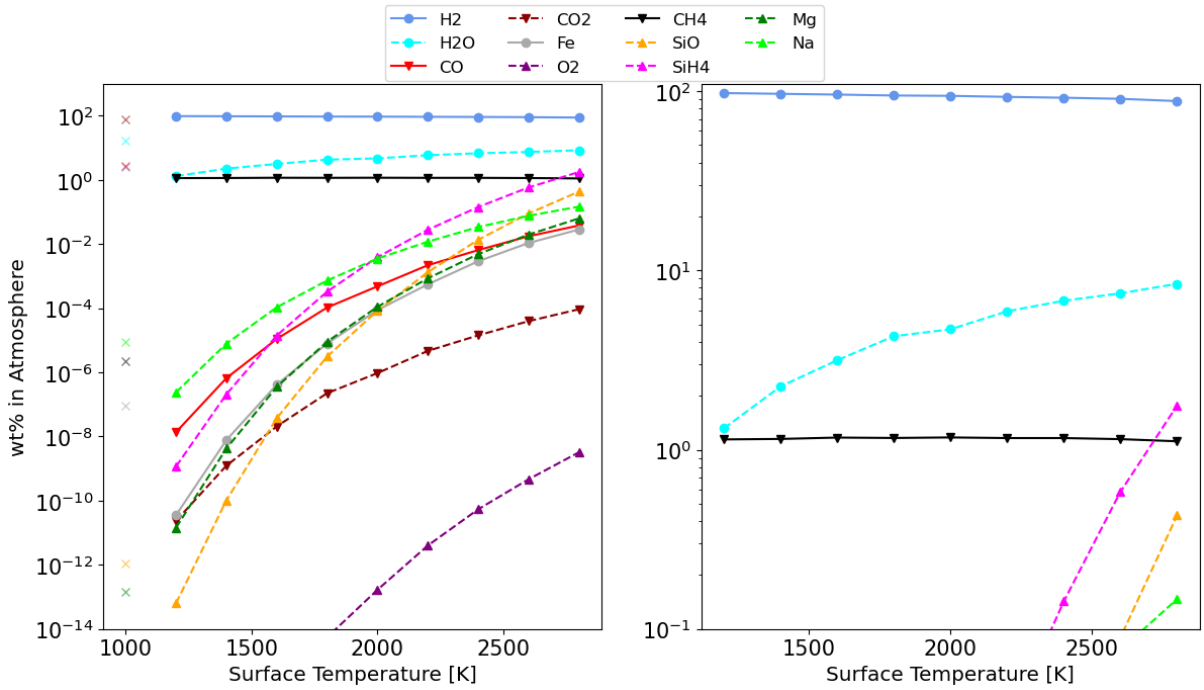


**Figure 13: Atmospheric Composition in wt% under increasing surface temperature.** Atmospheric composition is shown for a 4 $M_\oplus$ planet with a constant $T_{eq} = 3000$ K. Datapoints marked with an 'x' stem from runs with poor statistics. The panel on the right is zoomed in on the region 0.1% - 100%.

Figures 13, 14 and 15 show the compositions of the atmosphere, silicate mantle and metal core respectively, which are altered significantly compared to their initial states. Although $\mathrm{H_2}$ remains the most abundant species in the atmosphere, there is a significant increase even at modest $T_s$ in the abundances of $\mathrm{H_2O}$, $\mathrm{SiH_4}$, $\mathrm{SiO}$, and $\mathrm{Na}$. After equilibration, the atmosphere contains roughly 1% $\mathrm{CH_4}$, which remains roughly constant for increasing $T_s$. The rocky species remain scarce compared to hydrogen throughout the temperature range, but the atmosphere is steadily enriched in $\mathrm{SiO}$, $\mathrm{CO}$, $\mathrm{Na}$ and $\mathrm{Mg}$ as the surface temperature is increased.

The mantle is primarily composed of $\mathrm{MgSiO_3}$, with smaller amounts of $\mathrm{MgO}$ and $\mathrm{SiO_2}$ making up the remainder. This remains true after equilibration, however a major difference is the ingress of $\mathrm{H_2}$ in the melt, which makes up $\approx 0.1\%$ of the melt by weight after equilibrium is reached. This amassed hydrogen reacts with $\mathrm{SiO_2}$ to form $\mathrm{H_2O}$ in the melt and $\mathrm{Si}$ in the metal (R6). As such, the amount of water in the melt increases in tandem with the amount of $\mathrm{Si}$ in the metal, as seen in figure 15. The rise in the weight fraction of $\mathrm{SiO_2}$ in spite of its removal by means of reaction R6 is likely due to the speciation of enstatite ($\mathrm{MgSiO_3}$) and ferrosilite ($\mathrm{MgSiO_3}$), and to a lesser extent $\mathrm{Na_2SiO_3}$, which all produce $\mathrm{SiO_2}$.

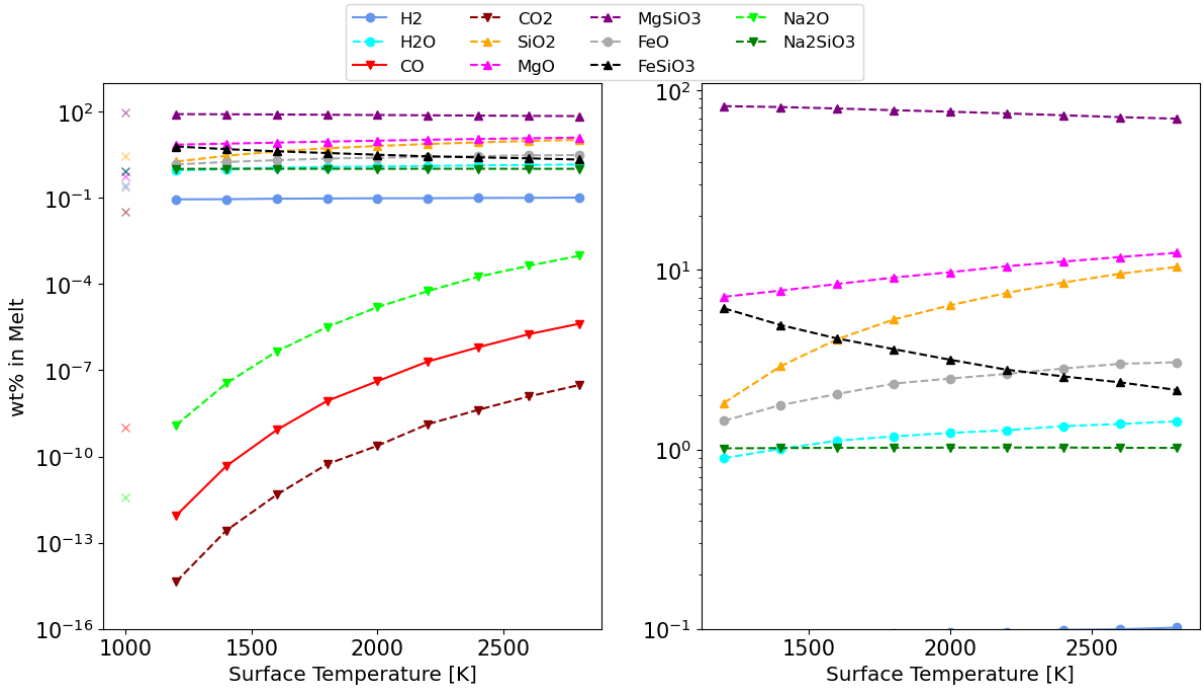


**Figure 14: Melt Composition in wt% under increasing surface temperature**. Here shown is the melt composition for the same parameters used in Figure 13

.

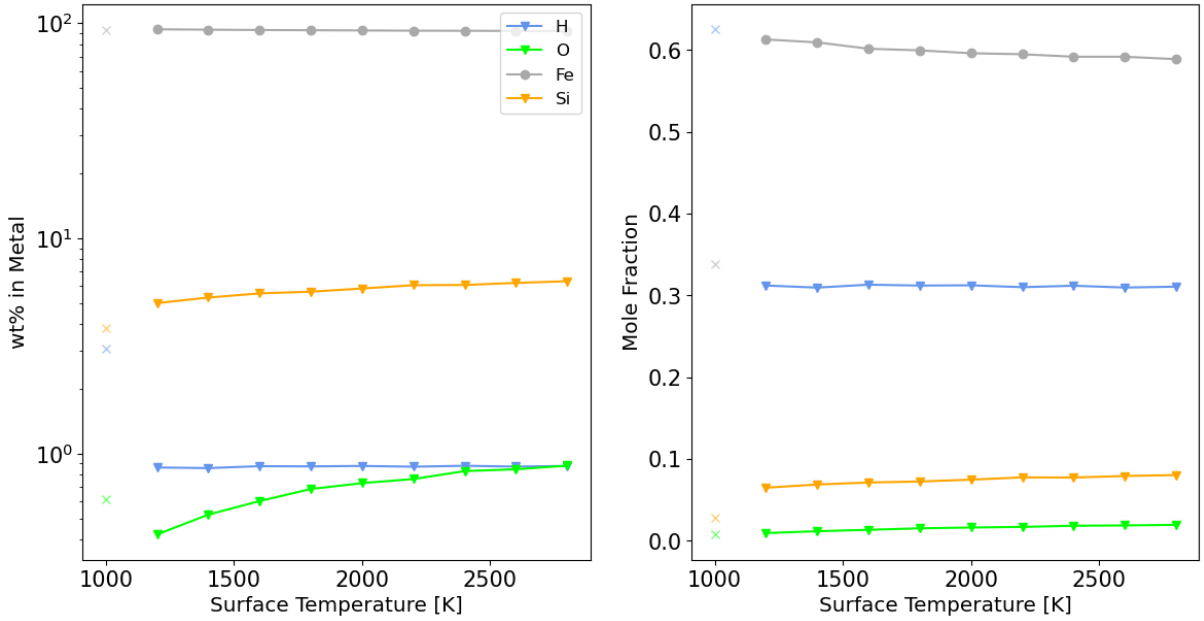


**Figure 15: Metal Composition under increasing surface temperature**. The composition is shown in wt% (left) and by mole fraction (right) for the same 4 $M_\oplus$ planet with $T_{eq} = 3000$ K.

Before equilibration, the metal is entirely made up of $\mathrm{Fe}$. Figure 15 shows that $\mathrm{Fe}$ remains almost ubiquitous in the metal, but a key result of equilibration is the ingress

of lighter elements into the metal reservoir. Immediately after equilibration, $\mathrm{O}$ and $\mathrm{H}$ build up to $\approx$ 1 wt% in the metal phase, while $\mathrm{Si}$ builds up to a few wt%. The reactions governing the exchange between the mantle and metal phases are R4, R5, R6 and R7 in the network, and are mediated by the equilibration temperature $T_{eq}$, which is kept constant here. The variability of oxygen in figure 15 might be due to the increased availability of oxygen - released from the evaporation of melt species - to partition into the metal reservoir. Due to the large discrepancies in the weights of these species, it is especially useful for the metal phase to look at the mole fractions of these species. The right panel of Figure 15 shows that the metal phase is almost 33% $\mathrm{H}$ after equilibration, and remains steady across increasing $T_s$. Increased $T_s$ seems to drive more $\mathrm{O}$ and $\mathrm{Si}$ into the core, but they constitute less than 10 wt% at these equilibration temperatures.

As the dominant element in the atmosphere and a driving factor in the reduction of the mantle, it is informative to investigate what form most of the hydrogen takes in the planet after equilibration. To that end, I compare how much hydrogen is present in every H-bearing species and relate this to the total amount of hydrogen in the system. The results are presented in Figure 16, which gives insights in the most important hydrogen reservoirs in the planet.

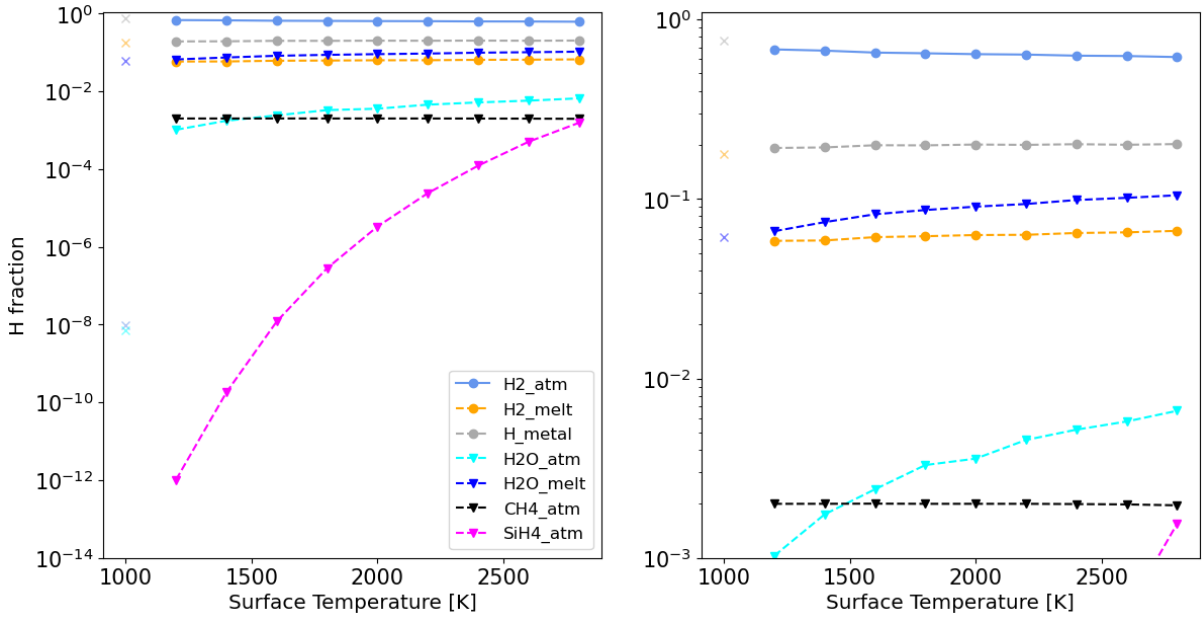


**Figure 16: Distribution of Hydrogen across its reservoirs in the planet**. Each line shows how much each reservoir accounts for the total amount of hydrogen in the planet, for increasing surface temperature. Results are presented for the same 4 $M_\oplus$ planet with $T_{eq} = 3000$ K.

For a constant $T_{eq} = 3000$ K and the surface temperatures considered in Figure 16, $\mathrm{H_2}$ gas remains the most abundant reservoir for hydrogen. The continuous increase of $\mathrm{SiH_4}$ may be attributed to the increasing quantities of $\mathrm{SiO}$ in the atmosphere, as more of the silicate mantle evaporates at the increased surface temperature, enabling the production of $\mathrm{SiH_4}$ via Reaction R19. As seen in the compositional plot for the metal phase, 'metallic' hydrogen becomes the second most abundant reservoir for hydrogen

immediately once chemical equilibrium has been reached, and remains a steady fixture with increasing surface temperature thereafter. Significant amounts of $H_2O$ are produced in both the atmosphere and mantle. While the melt contains more $H_2O$ in absolute terms, it is important to remember that the melt also contains more material than the atmosphere in all cases. By weight-percentage, the atmosphere contains up to eight times more water than the melt.

### 3.2.2 Effect of equilibration temperature

Now that I have explored the results of chemical equilibration between the atmosphere, mantle and metal core for a modest temperature range and a static equilibration temperature, the effects of more parameters on these results will be easier to interpret. I begin by considering a broader range of equilibration temperatures, as this will have an immediate influence on the composition of the metal core and melt. This in turn is expected to change the atmospheric composition and trends compared to the previous results.

Figure 17 is similar to Figure 12, but now shows the sizes of the atmosphere, mantle and metal phases for increasing equilibration temperature $T_{eq}$, from 3000 to 4500 K.

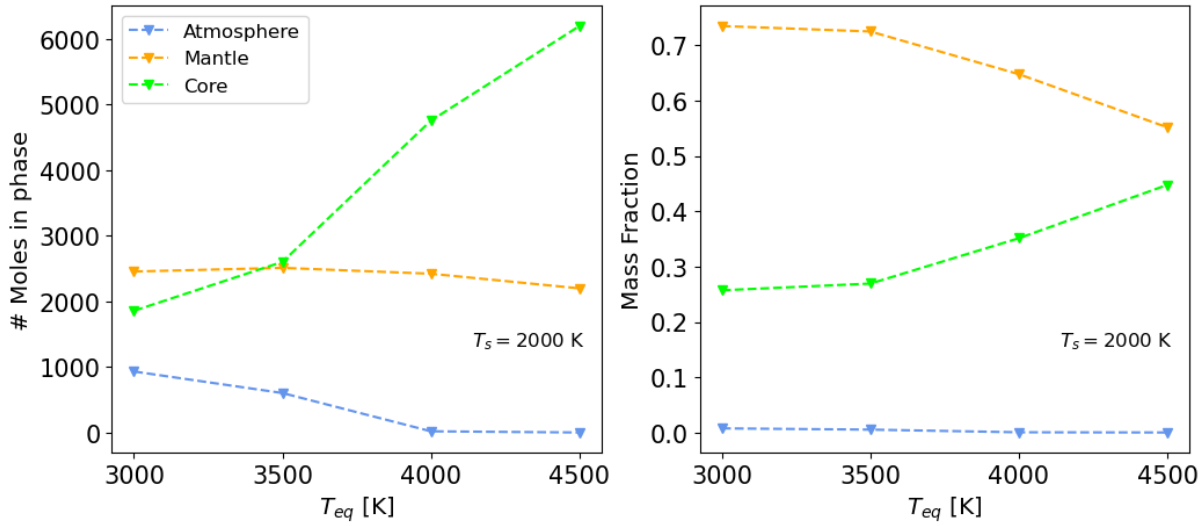


**Figure 17: Comparison of Phases under increasing core-mantle equilibration temperature**. Similar to Figure 12, but now showing the variation with $T_{eq}$ for a 4 $M_\oplus$ planet with a constant surface temperature of 2000 K. **Left:** Total number of moles in each phase. **Right:** Mass fraction of each phase.

The surface temperature is kept constant throughout. The effect of higher equilibration temperatures seem to be the shrinking and eventual almost total removal of the atmosphere, as the relative size of the core increases substantially. Past $T_{eq} = 3500$ K, the atmosphere contains a negligible amount of moles relative to the other two phases. The mass fraction of the core rises at the detriment of the mantle's, and the core likely

becomes the heaviest portion of the planet as $T_{eq} > 4500$ K.

As before, I inspect the compositions by weight percentage for the atmosphere and melt, in Figures 18 and 19, respectively. Figure 19 shows that the amount of $H_2$ in the melt stays fairly constant throughout, and the abundances of $SiO_2$ and $FeSiO_3$ both decrease as $T_{eq} > 3500$ K. However, rather than the atmosphere becoming enriched in $SiO$ and $SiH_4$, silicon mixes into the metal core instead, inhibiting the production of $SiH4$. The thinner atmosphere appears to be made up mostly of carbon oxides and water. The abundances of $Na$, $Mg$ and $Fe$ vary less with increasing $T_{eq}$, as this temperature does not directly influence their evaporation.

An important caveat to note is that the atmosphere is comprised of a much smaller amount of moles than was the case for a steady equilibration temperature. Beyond 3500 K, the atmosphere is made up of less than 30 moles. With fewer silicate species to populate this thin atmosphere, $CO$ and $CO_2$ appear to be very abundant, despite the fact that there is only a minor amount of carbon present in the planet under my baseline composition.

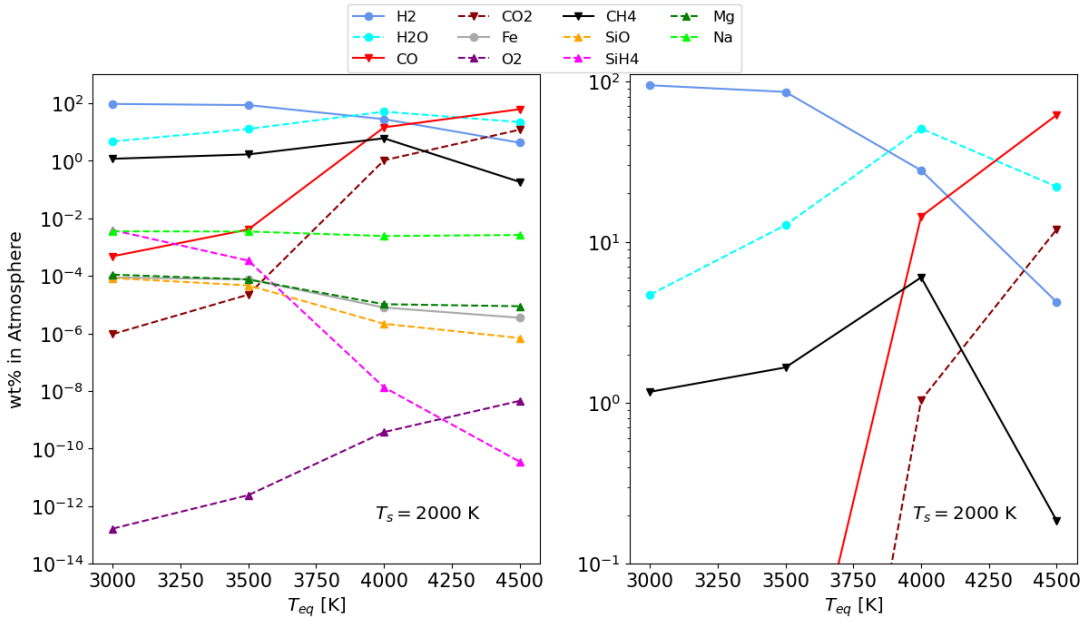


**Figure 18: Atmospheric Composition under increasing core-mantle equilibration temperature**. Similar to Figure 13, showing atmospheric composition for a $4M_\oplus$ planet for increasing core-mantle equilibration temperature, with a constant surface temperature of 2000 K.

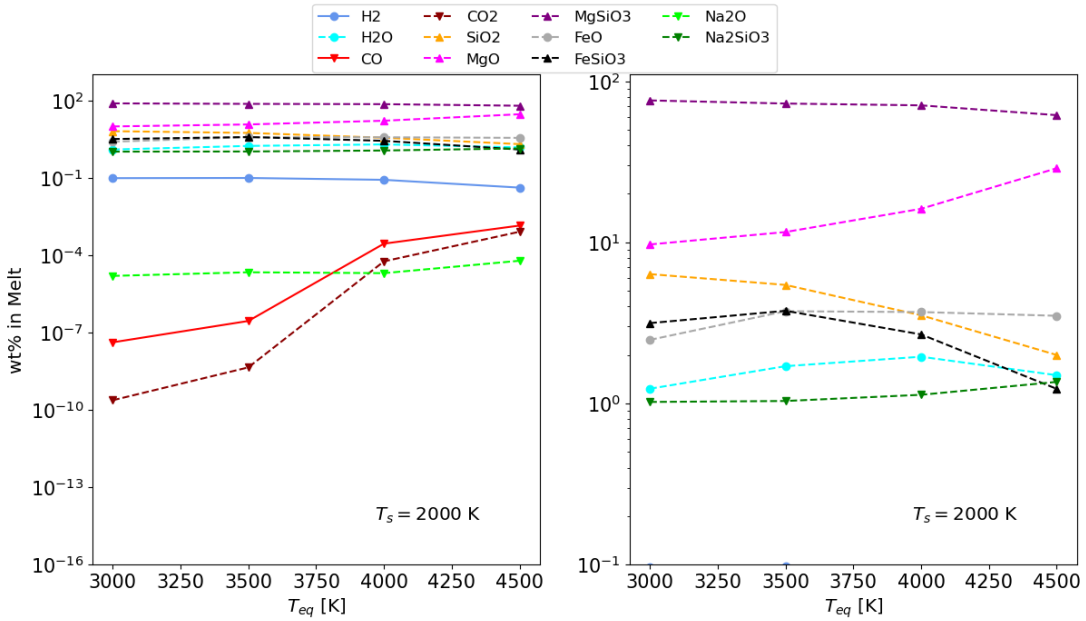


**Figure 19: Melt Composition under increasing core-mantle equilibration temperature**. Data is shown in a similar fashion to Figure 14 for a 4 $M_\oplus$ planet, with a constant surface temperature of 2000 K.

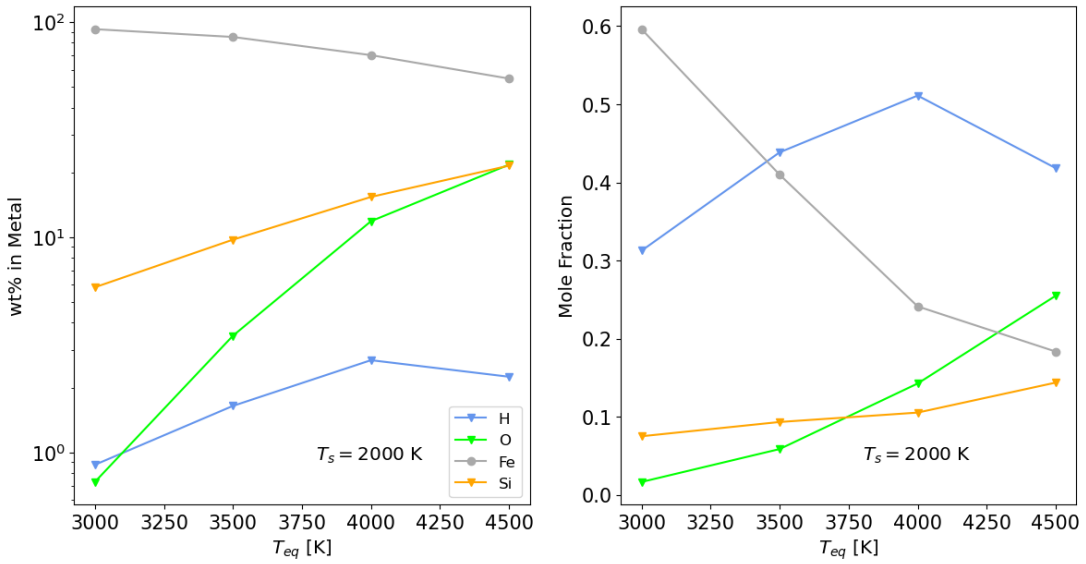


**Figure 20: Metal Composition under increasing core-mantle equilibration temperature**. Composition is shown in terms of wt% (**Left**) and by mole fraction (**Right**) for the same 4 $M_\oplus$ planet, with a constant surface temperature of 2000 K.

Inspecting the metal composition (Figure 20) shows that the sinking of hydrogen, silicon, and oxygen into the metal core is sensitive to $T_{eq}$. Note the contrast with the trends of the metal composition in Figure 15, which show these compositions to be more or less constant for surface temperature. By weight, silicon and oxygen compete

to become the second-most-important contributor to the total metal phase, although most of the metal core is composed of hydrogen by mole fraction. By total amount of moles, the core has increased from an initial 1250 moles to 6000 at $T_{eq} = 4500$ K as a result of the stoichiometry of Reactions R4, R5, R6 and R7. The main by-products of these reactions should be the production of $\mathrm{FeO}$ and $\mathrm{H_2O}$ in the melt via R4 and R6, and the corresponding removal of $\mathrm{SiO_2}$. These trends are visible in Figure 19, although the increasing abundances of $\mathrm{FeO}$ and $\mathrm{H_2O}$ are inhibited at $T_{eq} > 4000$ K.

Figure 21 again shows the distribution of hydrogen across all species across the various phases of the planet, now for increasing $T_{eq}$. Ultimately, increasingly hot equilibration temperatures push more and more hydrogen into the metal core, at the detriment of other hydrogen reservoirs. Past 4000 K, the increasing importance of metallic hydrogen slows, possibly because there is less and less hydrogen in the melt to partition further into the core. Atmospheric hydrogen is the most sensitive to the increasing equilibration temperatures, decreasing rapidly past 3500 K.

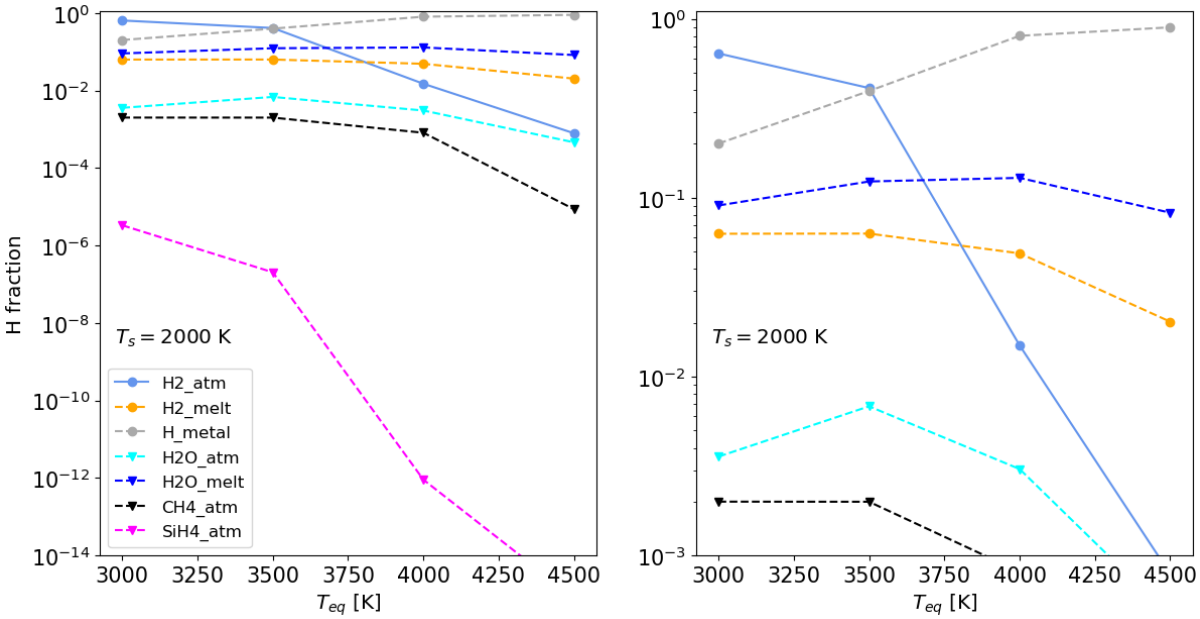


**Figure 21: Distribution of hydrogen under increasing core-mantle equilibration temperature**. As in Figure 16, shown is the hydrogen fraction for a $4M_\oplus$ planet for increasing core-mantle equilibration temperature.

These results show that the mixing of lighter elements into the metal core is, as expected, highly sensitive to the core-mantle equilibration temperature. The atmosphere is removed and recycled into the planetary exterior rapidly past 3500 K, which I will revisit in Section 4.

### 3.2.3 Oxygen Fugacity

To further investigate the joint influence of surface and core-mantle equilibration temperatures on the composition of the planet, I calculate the intrinsic oxygen fugacities of both the atmosphere and the condensed portions of the planet. These oxygen fugacities are relative to the fugacity defined by the reaction between pure $\mathrm{Fe}$ and pure Wüstite ($\mathrm{FeO}$); hence these oxygen fugacities are relative to the Iron Wüstite buffer ($\Delta IW$). I maintain the baseline composition defined previously, which corresponds to an initial oxygen fugacity for the melt of $f_{O2} = \Delta IW - 2.8$.

The oxygen fugacity of the atmosphere appears more sensitive to the surface temperature than that of the condensed part of the planet; the atmosphere starts out highly reduced due to being composed of almost entirely hydrogen. The oxygen fugacity at $T_s \approx 1000$ K increases with $T_{eq}$ significantly, likely due to larger and larger amounts of atmospheric hydrogen partitioning into the metal reservoir at higher equilibration temperatures; as such, the atmosphere starts out more oxidized by comparison at these higher equilibration temperatures. For all $T_{eq}$, the oxygen fugacity of the atmosphere increases thereafter with surface temperature, as large amounts of $\mathrm{H_2O}$ enrich the atmosphere. At higher equilibration temperatures (pink and purple lines), $\mathrm{SiO}$ and carbon oxides also play a larger role in the atmosphere, explaining the increased oxidation state of the atmosphere in those models.

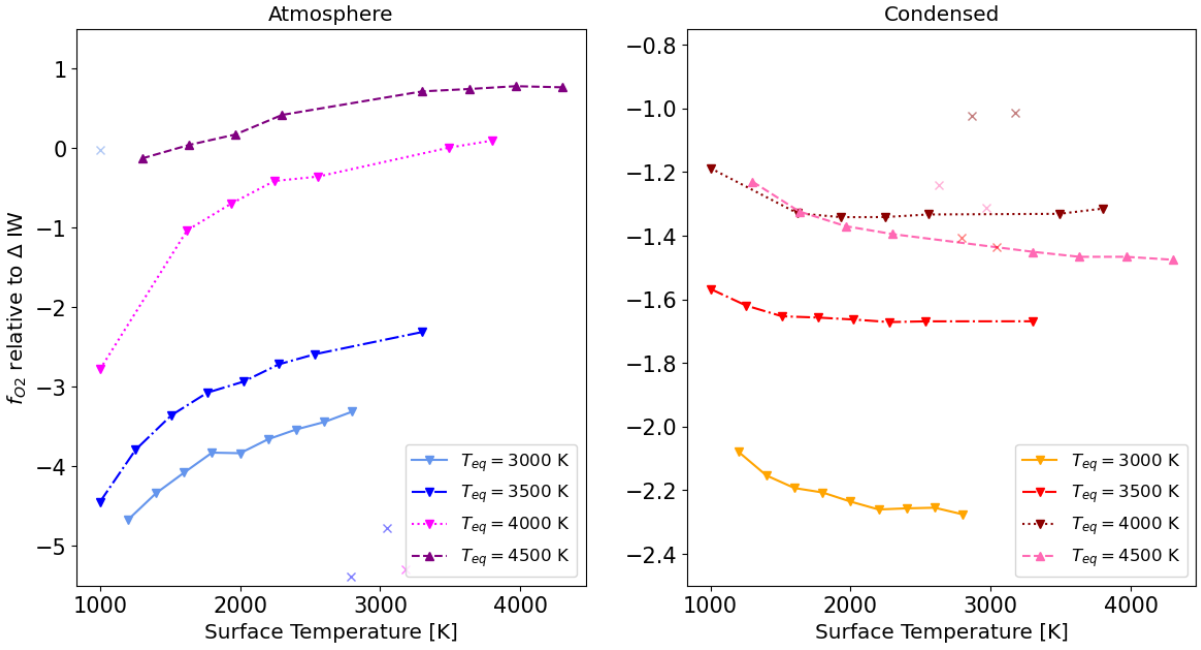


**Figure 22: Variation of Oxygen Fugacity with surface and core-mantle equilibration temperatures.** Oxygen fugacities relative to the IW buffer for the atmosphere and condensed part of a $4M_\oplus$ planet are shown under various surface and equilibration temperatures. The initial composition corresponds to a mantle oxygen fugacity of $\approx \Delta IW - 2.8$.

The condensed part of the planet, which includes both the melt and metal reser-

voirs, notably stays more constant in oxygen fugacity than the atmosphere, only showing variations of roughly 0.2 Dex on average. Overall the condensed part becomes more reduced with increasing $T_s$ yet more oxidized with increasing $T_{eq}$ until a plateau is seemingly reached for $T_{eq} \geq 4000$ Kelvin at $f_{O2} \approx \Delta IW - 1.2$. The reduction of the condensed part of the planet can be attributed in some part to the ingress of hydrogen into the melt, although the concentration of $\mathrm{H_2}$ in the melt stays roughly constant for surface temperature (Figure 14). The increased oxidation of the condensed part of the planet with increasing $T_{eq}$ is a direct result of the ingress of lighter material into the metal core; the concentration of pure $\mathrm{Fe}$ decreases for increasing $T_{eq}$, resulting in overall higher oxygen fugacities.

## 3.3 Varying planetary composition

### 3.3.1 Mg / Si ratio

Since the initial composition of the model planet will decide the total amount of moles of each element, it will have a large influence on the ultimate composition of each phase after chemical equilibrium is reached. While I can vary the composition in a multitude of ways, I have chosen here to vary the $\mathrm{Mg/Si}$ of the silicate melt. These elements make up the bulk of the mantle in my baseline composition, which has an Mg/Si ratio of approximately $1.03$. To compare, I create two new compositions by changing the concentrations of $\mathrm{MgO}$, $\mathrm{MgSiO_3}$ and $\mathrm{SiO_2}$ as follows:

- Composition 1: 3.2% $\mathrm{MgO}$, 26.1% $\mathrm{SiO_2}$, 69.7% $\mathrm{MgSiO_3}$, giving Mg/Si $\approx$ 0.75. I will refer to this as the *Silicon-rich composition.*
- Composition 2: 52% $\mathrm{MgO}$, 0.01% $\mathrm{SiO_2}$, 47% $\mathrm{MgSiO_3}$, giving Mg/Si $\approx$ 2.1. I will refer to this as the *Magnesium-rich composition.*

I take these $\mathrm{Mg/Si}$ ratios because they represent end-points of the likely distribution of $\mathrm{Mg}$ / $\mathrm{Si}$ ratios of terrestrial exoplanets, based on a study of stellar abundances by Spaargaren et al. [2023]. These different conditions additionally represent varying mantle oxidation states, as the Silicon-rich composition contains more oxygen and hence represents a more oxidized melt than the Magnesium-rich composition, which is more reducing compared to the baseline composition.

As before, I obtain the equilibrated compositions for increasing $T_s$ at two distinct equilibration temperatures, $T_{eq} = 3000$ K and $T_{eq} = 4500$ K. I compare the results for these compositions with my previous findings for the baseline composition, with Mg/Si $\approx$ 1.03.

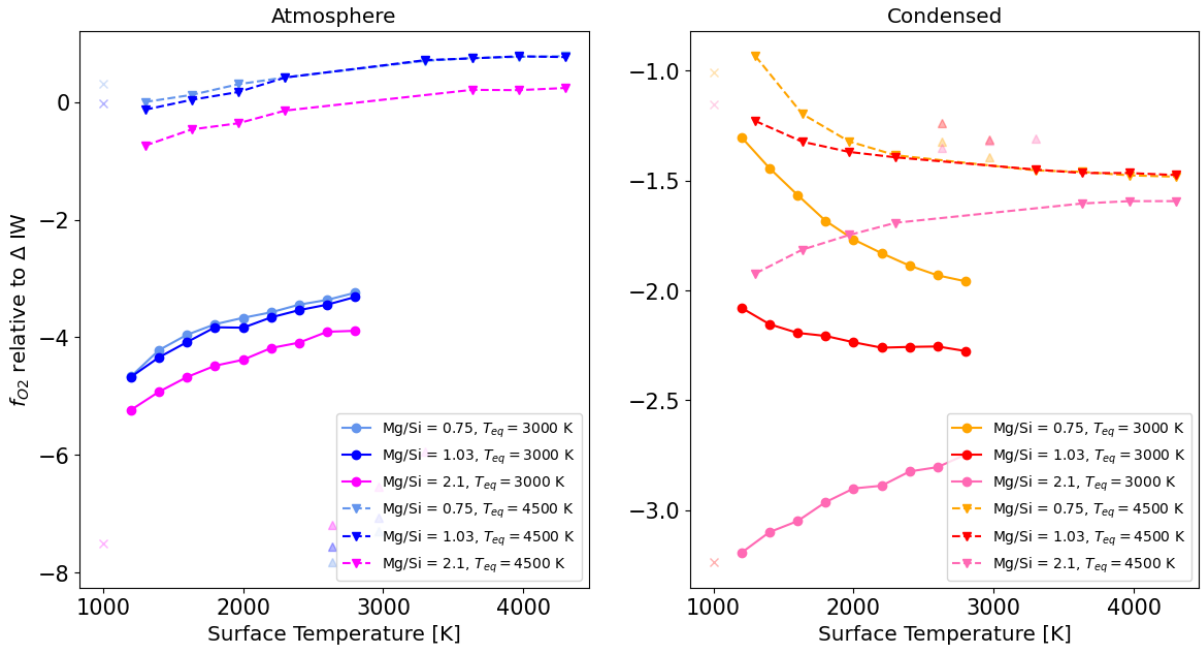


**Figure 23: Oxygen Fugacities for various mantle compositions**. Different colors correspond to different mantle compositions of varying Mg/Si ratios, ranging from 0.75 (lightblue / yellow), 1.03 (blue / red) and 2.10 (magenta / pink). Solid lines represent the results of equilibration with $T_{eq} = 3000$ K, dashed lines represent results for $T_{eq} = 4500$ K. The total planet mass is $4M_{\oplus}$ in all cases.

The calculated oxygen fugacities of the atmosphere and condensed portions of the planet are reported in Figure 23, which shows the oxygen fugacities changing with surface temperature for these various compositions. The models run with $T_{eq} = 3000$ K are represented in solid, and those run for $T_{eq} = 4500$ K are shown in dotted lines. The trends with increasing temperature are very similar for the atmospheric $f_{O2}$, which increases for each composition. The oxygen fugacity of the silicon-rich composition (light blue) and the baseline composition (dark blue) are very similar, while that of the magnesium-rich composition (magenta) is roughly 0.5 dex lower. As seen previously in Figure 22, a higher $T_{eq}$ leads to a significantly higher oxygen fugacity for the atmosphere irrespective of these different compositions.

For the condensed portion of the planet, I notice greater differences. The silicon-rich composition (yellow) starts out the most oxidized of all compositions before decreasing sharply with increasing temperature. In contrast, the magnesium-rich composition (pink) is more reduced before oxidizing at higher $T_s$. As before, hotter core-mantle equilibration temperatures increase the oxygen fugacities without modifying the trends with increasing surface temperature. These results are due to the simple fact that the main compositional differences lie in the concentrations of $\mathrm{MgO}$ and $\mathrm{SiO_2}$, as enstatite contains magnesium and silicon in equal amounts. As $\mathrm{SiO_2}$ carries more oxygen, the silicon-rich composition is more oxygen-rich than the magnesium-rich composition, as previously mentioned.

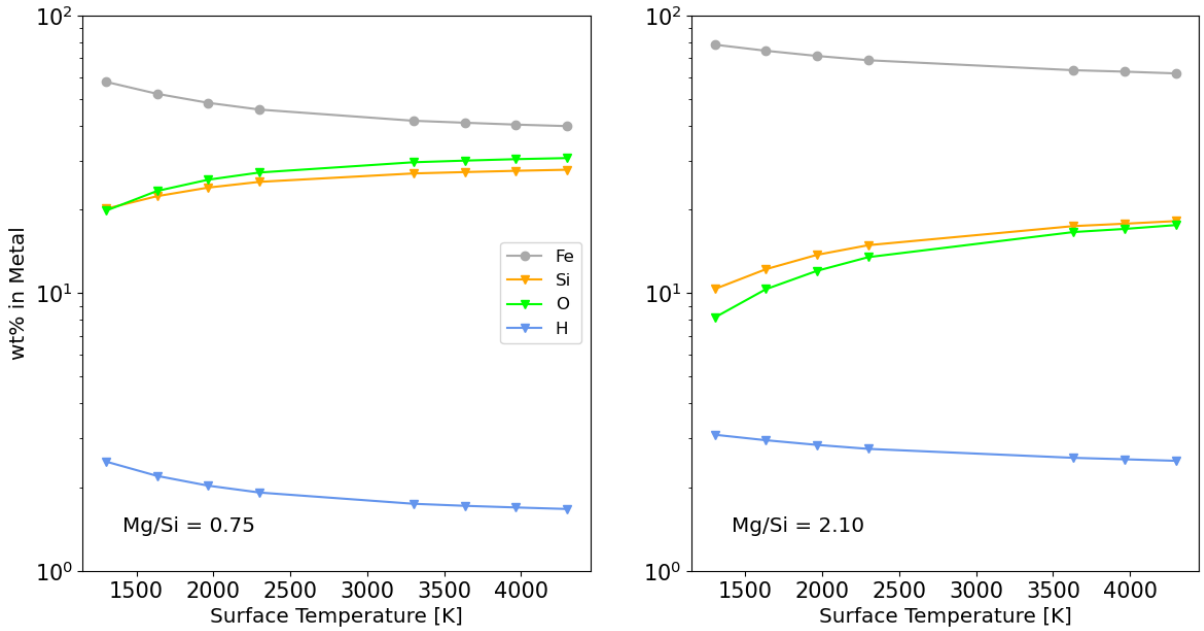


**Figure 24: Composition of Metal for silicon- and magnesium-rich compositions.** Shown here are results for $T_{eq} = 4500$ K for the silicon-rich (**Left**) and magnesium-rich (**Right**) compositions.

The increased availability of oxygen in the silicon-rich model should manifest itself in compositional differences across the three reservoirs. In Figures 24 and 25, I compare the compositions of the metal, atmosphere and melt by weight-percentages for the silicon-rich and magnesium-rich models in the respective left and right panels. For the silicon-rich model, the increased abundance of both $\mathrm{Si}$ and $\mathrm{O}$ naturally lead to their greater abundances in the metal reservoir compared to the magnesium-rich model (Figure 24). The concentration of hydrogen in the metal is higher for the magnesium-rich model.

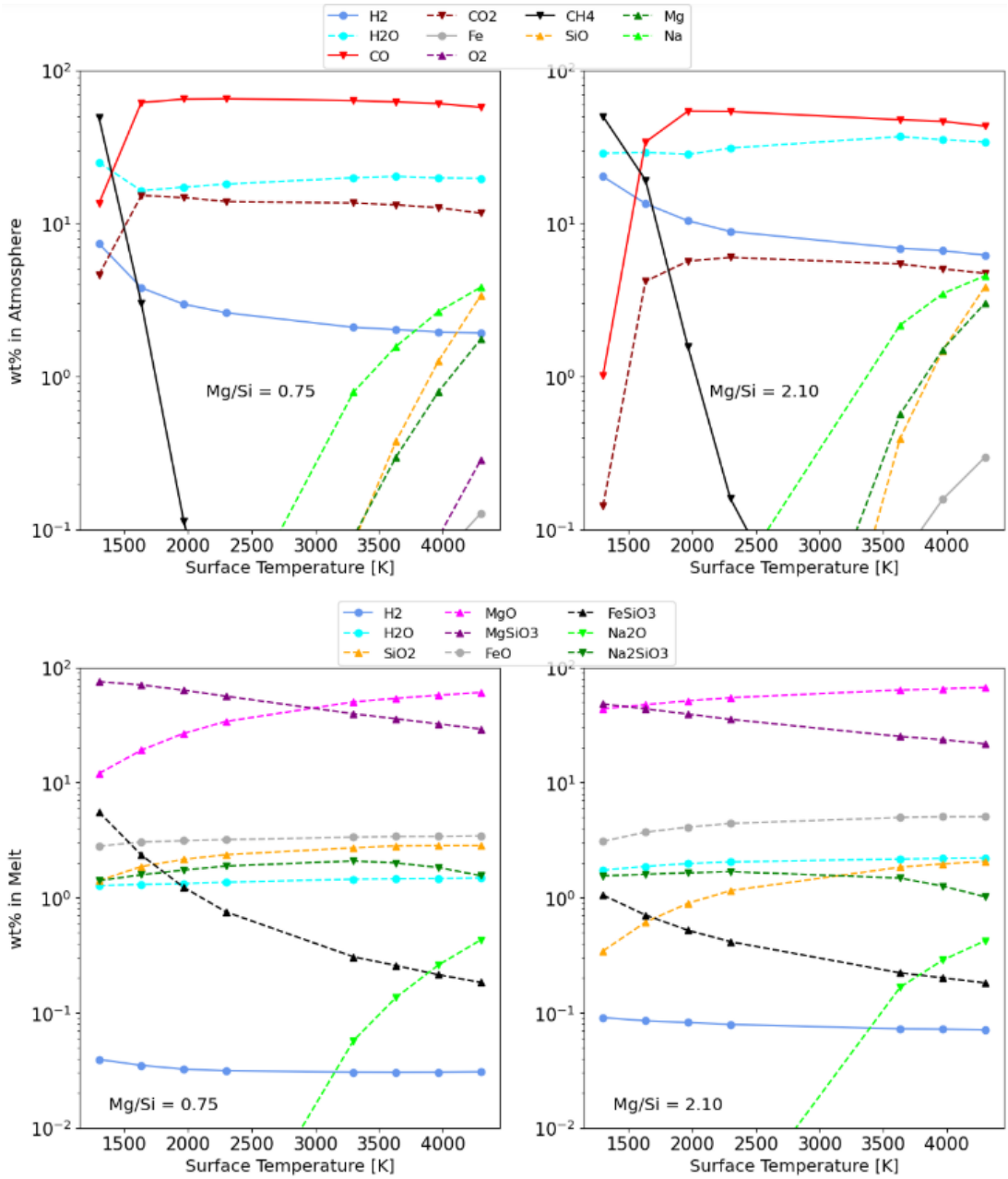


**Figure 25: Atmosphere and Melt compositions for silicon- and magnesium-rich models**. The top panels show the atmospheric composition for the silicon-rich (**Left**) and magnesium-rich (**Right**) models after equilibration. The bottom panels show the Melt compositions for the same models. Note that this plot shows only the most abundant species in the range of 0.1 - 100%. Shown here are results for $T_{eq} = 4500$ K.

Interestingly, the composition of the melt becomes similar for both the silicon- and magnesium-rich models at higher surface temperatures; they are similarly abundant in $FeSiO_3$, $Na_2O$, $Na_2SiO_3$, $FeO$, $MgO$ and $MgSiO_3$ at $T_s = 4300$ K. The abundances of $H_2$ and $SiO_2$ show the greatest difference; the silicon-enriched model contains roughly $1.5$ times as much $SiO_2$ at those temperatures. The excess oxygen present in the silicon-rich environment takes the form of $SiO_2$, which donates most of its oxygen to the metal

and atmosphere via reactions R5 and R13, rather than form additional water in the melt via R6.

Given the similar abundance of $\mathrm{SiO}$ in the atmosphere for both models, much of the excess $\mathrm{SiO_2}$ in the melt of the silicon-rich model likely partitions into the metal. However, $\mathrm{O_2}$ builds up to wt% levels in the silicon-rich model's atmosphere for the first time in my results so far, while $\mathrm{Fe}$ is more abundant for the magnesium-rich model. Another outcome is a decrease in the concentration and corresponding weight-abundance of $\mathrm{H_2}$ for the silicon-rich model.

### 3.3.2 Planet Mass

Another parameter that has not been considered so far is the planet mass, $M_p$. This enters the model only through Equation 4, used to calculate the pressure at the boundary between the atmosphere and the magma-ocean. As such, it influences the atmospheric species primarily, for which pressure corrections are implemented in Equations 1. It is difficult to reason in advance what effect these pressure corrections have on the atmosphere's composition as the system settles into chemical equilibrium. To that end, I model a planet with $M_p = 1.5\,M_\oplus$ and compare the results to the previous $4\,M_\oplus$ case. Because I expect these results to only impact the atmospheric composition, I model at a lower core-mantle equilibration temperature of $3000$ K, where the atmosphere is not partitioning fully into the metal phase.

The pressure difference between a $1.5M_\oplus$ and a $4M_\oplus$ planet is significant. There is little variance in the pressure with increasing surface temperature, and I find mean surface pressures $\langle P \rangle = 1.26$ GPa and $2.35$ GPa for the lighter and heavier planet respectively. The large difference leads to macroscopic changes in the atmospheric composition and atmospheric oxidation state, as shown in Figure 26, which shows the atmospheric composition in the left panel and the oxygen fugacities in the right panel.

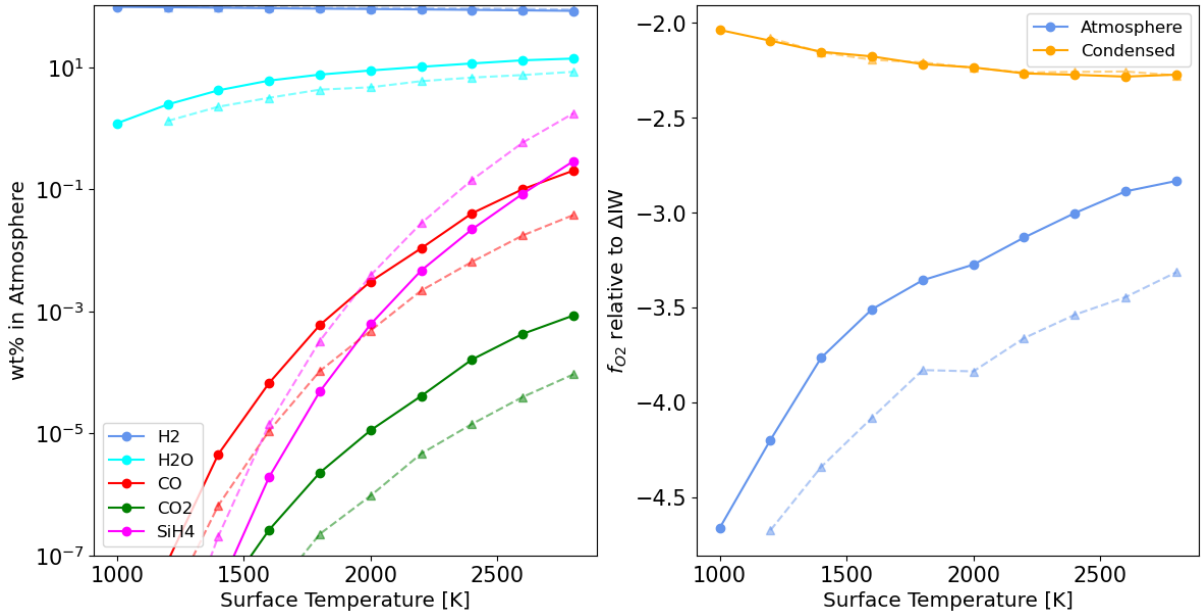


**Figure 26: Comparison of Atmospheric Composition and Oxygen Fugacity for a light and heavy planet**. Solid lines represent data for the 1.5 $M_{\oplus}$ planet, while dashed lines show results for a 4 $M_{\oplus}$ planet for comparison. Results are shown for $T_{eq} = 3000$ K. Only atmospheric species that display significant differences between the models are shown to improve legibility.

The lighter planet has higher abundances of $H_2O$, $CO$ and $CO_2$ than the $4M_{\oplus}$ planet for all temperatures, and comparatively less $SiH_4$. Accordingly, the atmospheric oxygen fugacity of a $1.5M_{\oplus}$ planet is higher than that of its heavier counterpart. The decreased pressure appears to affect Reactions R16, R17 and R18, less soluble into the magma ocean, leading to their increased abundance here. The right panel of Figure 26 shows that the oxygen fugacity of the condensed part of the planet remains almost identical between the two planets. The pressure difference barely affects the compositions of the melt and metal phases, and so I do not inspect their compositions in any more detail here.

## 3.4 Ideal Mixing

Up to this point, all model runs incorporated activities to describe the deviation from ideal behaviour for $Si$, $O$ and $H_2O$. Here I briefly give consideration to the ways in which these results change when I instead consider all mixing to be ideal. Figure 27 shows the compositions in weight-percent of the atmosphere and mantle of a $4M_{\oplus}$ planet again by increasing surface temperature, but now with all mixing treated as ideal. This Figure is intended to be compared to Figures 13 and 14, to show how the global compositions differ after chemical equilibrium is set.

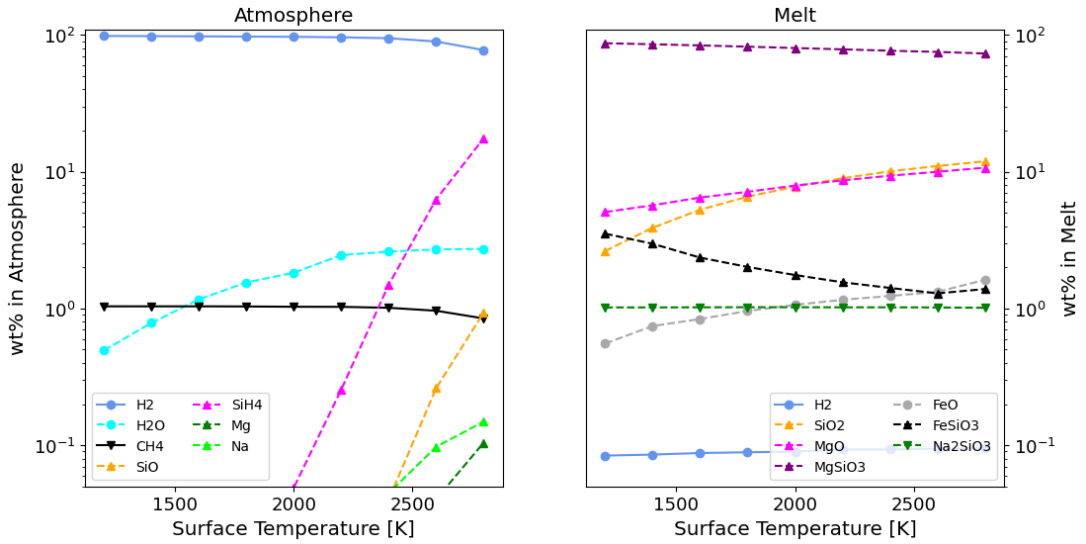


**Figure 27: Atmospheric Composition under ideal conditions**. Results are shown for a $4M_{\oplus}$ planet with $T_{eq} = 3000$ K with ideal mixing only. The region from 0.1 to 100% is shown for the atmosphere (**Left**) and melt phase (**Right**).

The most significant differences between the ideal and non-ideal cases are represented in this figure and the right-most panels of Figures 13 and 14. $\mathrm{SiH_4}$ is significantly more abundant in the atmosphere for the ideal case, making up to around 20% of the atmosphere by weight - ten times more than the maximum abundance seen in the non-ideal case. This is attributable to a smaller amount of $\mathrm{Si}$ and $\mathrm{H}$ in the metal for the ideal case, possibly leaving more material with which to ultimately form $\mathrm{SiH_4}$ through reactions R4, R5, R13 and R19. At the same time, $\mathrm{H_2O}$ is less abundant in the atmosphere - possibly due to being diluted by the higher amount of $\mathrm{SiH4}$ - and much less abundant in the melt. While $\mathrm{H_2O}$ builds up to $\approx$ 1% in the non-ideal case, in the right panel of Figure 27 $\mathrm{H_2O}$ does not even appear; it makes up only 0.004% of the melt, and melt-phase $\mathrm{H_2O}$ is the smallest reservoir of Hydrogen in the planet, while it was the third-largest for the non-ideal case (Figure 16).

On a global scale, these differences cause the oxygen fugacity to be roughly two dex lower at all temperatures for the ideal case compared to the non-ideal case, as the atmosphere is strongly reduced by the higher abundance of $\mathrm{SiH_4}$ while the melt is reduced due to the absence of $\mathrm{H_2O}$. For increased $T_s$, the atmospheric $f_{O_2}$ increases while the melt's decreases, similar to the behaviour shown by the light-blue and orange lines in Figure 22.

## 3.5 Unreactive Core Modelling

So far, I have allowed the full planet to equilibrate under the surface temperature and core-mantle equilibration temperature. The composition of the atmosphere and melt will change significantly if I only allow them to equilibrate with each other, and keep

the metal core chemically isolated from the rest of the system. I model the same $4M_{\oplus}$ planet and inspect the planet composition for temperatures ranging from $1100$ to $4500$ K. The core-mantle equilibration temperature is no longer relevant for this exercise. Since I incorporate activities for $\mathrm{Si}$, $\mathrm{Fe}$ and $\mathrm{O}$ in reference to $T_{eq}$, I consider here only ideal mixing to keep the metal core completely separated in all respects in the model.

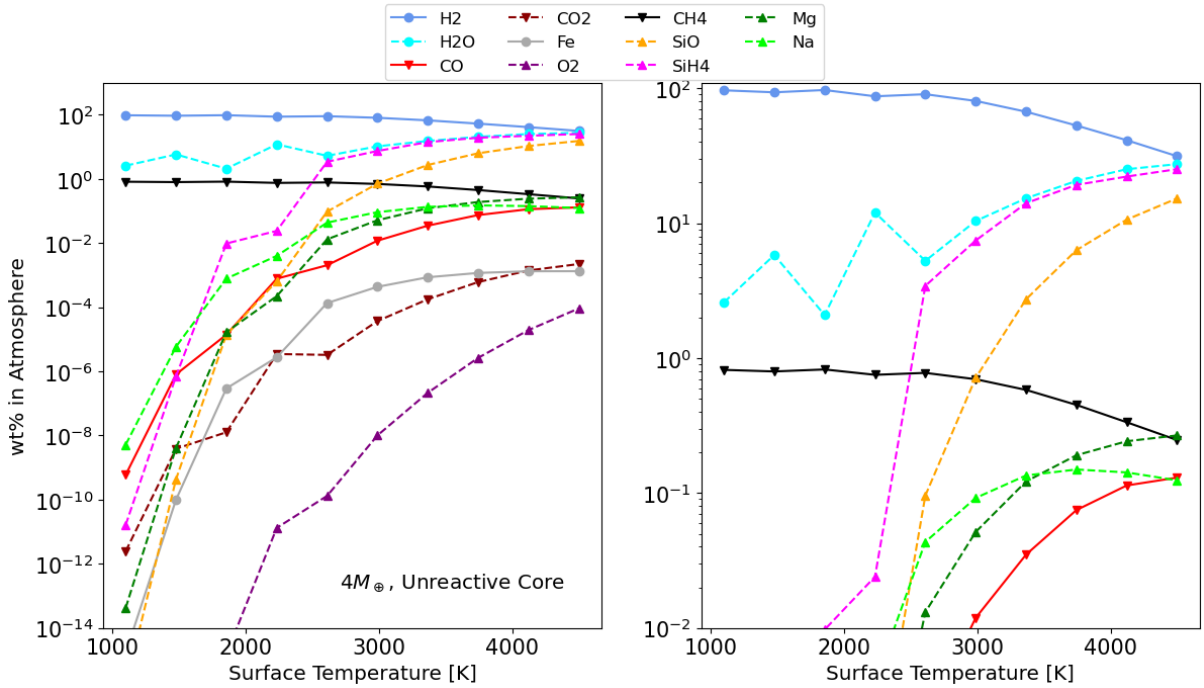


**Figure 28: Atmospheric Composition for an Unreactive Core.** Shown is the atmospheric composition by weight-percentage for a $4M_{\oplus}$ planet with an unreactive metal core. The right panel is zoomed in on the region from 0.01% - 100%, in accordance with Figure 13.

The resulting composition of the atmosphere and melt are presented in Figures 28 and 29 respectively. These compositions are not directly comparable to any previous model planets, as the previous plots were impacted by both $T_s$ and $T_{eq}$, whereas Figures 28 and 29 show these phase's compositions under increasing surface temperature alone. $\mathrm{H_2}$, $\mathrm{H_2O}$ and $\mathrm{SiH_4}$ become almost equally abundant at $T_s \approx 4500$ K, and $\mathrm{SiO}$ is able to build up to $\approx$ 10% of the atmosphere by weight. The increased abundance of $\mathrm{SiH_4}$ is at the cost of $\mathrm{CH_4}$. The abundance of water in the atmosphere varies significantly at lower temperatures. This may point to an instability in the model, as this variation lacks a strong physical explanation for a system in chemical equilibrium.

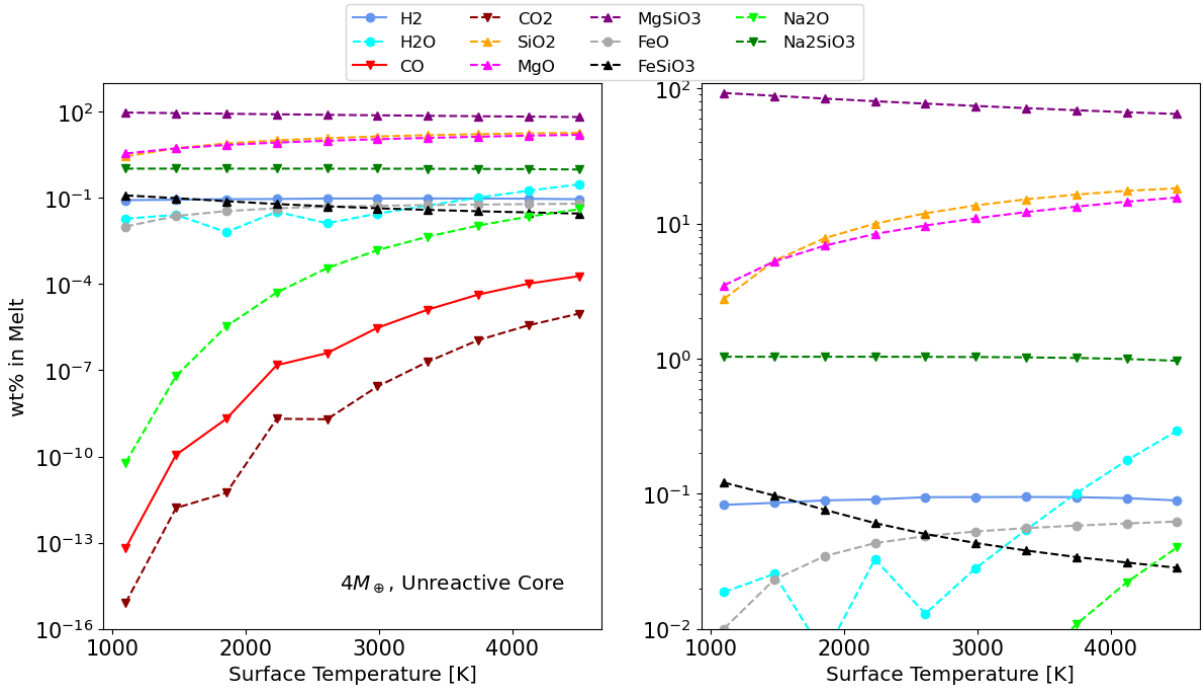


**Figure 29: Melt Composition for an Unreactive Core**. Shown is the melt composition for the same planet as in Figure 28.

Perhaps the greatest difference in the melt is the significantly reduced abundance of $\mathrm{FeO}$ and $\mathrm{FeSiO_3}$. While these species had abundances between 1 and 10% in the melt for all previous models, here they are reduced to below 0.1% at almost all temperatures. $\mathrm{FeSiO_3}$ speciates into $\mathrm{FeO}$ and $\mathrm{SiO_2}$, and in absence of reaction R4 to produce $\mathrm{FeO}$ by driving $\mathrm{Si}$ into the metal, their abundances are reduced compared to previous cases. Instead, the melt is around 80% $\mathrm{MgSiO_3}$ and 10% each in $\mathrm{MgO}$ and $\mathrm{SiO_2}$. With no metal core for silicon to partition into and several reaction pathways enabling the production of $\mathrm{SiO_2}$, the result is a high abundance of both $\mathrm{SiO_2}$ in the melt and $\mathrm{SiO}$ in the atmosphere. Lastly, there is significantly less water in the melt for the unreactive case: around 0.3% in this melt, while it reached between five and ten times higher wt% in all previous compositions, irrespective of $T_{eq}$ (as seen in Fig 19). Direct production of water in the melt is prohibited as R6 does not take place in absence of a reactive core, hence melt-phase $\mathrm{H_2O}$ comes from the solubility of water into the melt (R16). Higher temperatures facilitate a heavier atmosphere and hence a higher surface pressure, forcing more $\mathrm{H_2O}$ into the melt at higher temperatures and thus explaining the increased abundance of water at higher $T_s$.

Overall, without the metal core acting as a sink for $\mathrm{O}$, $\mathrm{Si}$ and $\mathrm{H}$, the atmosphere becomes more quickly oxidized than in previous cases, as $\mathrm{H_2O}$ and $\mathrm{SiO}$ build up to high abundances quickly. The variability of $\mathrm{H_2O}$ in both the melt and atmosphere at $T_s < 2500$ K are very similar and do not seem tied to any physical mechanism that has come up in previous cases. As such, I assume these fluctuations to be the result of instabilities in the model for the unreactive case.

# 4 Discussion

## 4.1 Comparison to Schlichting & Young (2022)

In this work, I have used a chemical equilibrium model originally developed by SY22 to investigate the changes in the compositions of exoplanetary atmospheres, molten silicate mantles and metal cores, under several parameters of interest. Unfortunately, the version of the code utilized in this thesis differed from the version used in SY22 in numerous ways, making a direct comparison difficult. These differences include the inclusion of reaction R19; the incorporation of non-ideal behaviour for $\mathrm{Si}$, $\mathrm{O}$ and $\mathrm{Fe}$, and the usage of a separate surface temperature $T_s$ and core-mantle equilibration temperature $T_{eq}$. Other differences between the model versions are likely, but the scope of the model makes them harder to isolate. Nevertheless, I will perform a qualitative comparison between the major results of my work with that of the modelling performed by SY22 and infer from where any differences might arise.

For a $4M_{\oplus}$ planet with a reactive metal core, SY22 computed the mass fractions of the atmosphere, melt and metal core from $3500$ to $6000$ K. In their results, large portions of the melt evaporate, leading to an increase in the mean molecular weight of the atmosphere. As a result, they observe a gradual increase in the mass fraction of the atmosphere at the detriment of the melt's. In my model, however, I must account for the separate core-mantle equilibration temperature being higher than the surface temperature. As Figure 17 shows, the atmosphere decreases in mole count rapidly once $T_{eq} \geq 4500$ K. This motivated me to inspect lower temperature ranges, where the effects of equilibration on the still-retained atmosphere could be inspected. At lower temperatures, the mass fractions of the three phases remain roughly constant, which does not seem inconsistent with the results of SY22.

It is puzzling that the full-scale equilibration of the core, mantle and atmosphere at temperatures beyond 4500 K does not to recycle the atmosphere into the interior in the results of SY22, as occurs in my results. The influence of non-ideal behaviour for $\mathrm{Si}$, $\mathrm{O}$ and $\mathrm{Fe}$ in the metal phase likely plays a role in modifying my results for the core composition compared to their work. The hierarchical composition of the metal is $\mathrm{Fe}$ > $\mathrm{O}$ » $\mathrm{H}$ » $\mathrm{Si}$ according to SY22, whereas in my results I instead report $\mathrm{Si}$ and $\mathrm{O}$ as the most abundant species in the metal phase after iron, even at $T_{eq} = 4500$ K, where there is overlap with Figure 12 in their work. The implementation of activities for $\mathrm{Si}$, $\mathrm{O}$ and $\mathrm{Fe}$ in the metal-silicate exchange could account for these differences, as well as the dependency on two temperatures rather than one.

The results for atmospheric and condensed oxygen fugacities are similar in trends. Irrespective of $T_{eq}$, I notice a continuous increase in atmospheric $f_{O2}$ values relative to the IW buffer with increasing surface temperature; similarly, SY22 find increases of up to $2$ dex as the temperature increases from $3500$ to $6000$ K. Again, a direct comparison is not possible as my modelling takes place at lower temperatures; the best model run I have to compare to the results of the 2022 work is the modelling with $T_{eq} = 4500$ K

(Figure 22, purple and pink lines). I notice similar increases in the atmospheric oxidation state, although my atmospheres become more oxidized at lower temperatures than those in the 2022 work. For the silicate, SY22 report sharp reductions in oxygen fugacity, going from $f_{O2} = \Delta IW - 3.5$ at $T = 3500$ K down to $f_{O2} = \Delta IW - 4.6$ at $T = 6000$ K. My findings are again quite different, with higher $f_{O2}$ values immediately after equilibration is set and decreasing moderately with increased surface temperature thereafter. The trends are roughly similar - both codes agree that increasing temperature raises the oxidation state of the atmosphere, while decreasing that of the silicate. Figure 22 illustrates the importance of the two temperatures on the resulting oxidation state, hence the differences between the two results likely stems from the different ways that the temperatures are handled.

Given the stark influence of $T_{eq}$ on the composition of the atmosphere, my results for the atmospheric composition are difficult to compare with the findings of SY22. My models for a hot planet with $T_{eq} = 4500$ K and surface temperatures up to $4300$ K result in an atmosphere that is predominantly $\mathrm{CO}$ and $\mathrm{H_2O}$, with $\mathrm{H2}$ and $\mathrm{SiO}$ at similar, if lower, abundances. SY22 do predict similar abundances for $\mathrm{H_2}$ and $\mathrm{SiO}$ at $T = 4500$K, but with significantly less $\mathrm{H_2O}$, $\mathrm{CO}$. The abundance of $\mathrm{Fe}$ in the atmosphere is roughly similar, hovering between 0.1 and 1% in the atmosphere. For an unreactive metal core, my results as presented in Figure 28 give an atmosphere with similar abundances of $\mathrm{H_2O}$, $\mathrm{H_2}$ and $\mathrm{SiO}$ at $T_s = 4500$ K. SY22 report an atmosphere that remains dominated by $\mathrm{H_2}$, with lower abundances of $\mathrm{SiO}$ and $\mathrm{H_2O}$ compared to my result. The inclusion of $\mathrm{SiH_4}$ in my modelling forms the primary difference between the models, as R19 can combine with R10 to produce more water at the cost of hydrogen. Furthermore, the non-ideal behaviour of $\mathrm{H_2O}$ solubility into the melt is incorporated in my modelling here, while it is not included in SY22. This difference combined with the presence of Reaction R19 may explain the discrepancy when it comes to the abundance of $\mathrm{H_2O}$ in the atmosphere.

To better contextualize my results, I look beyond the work of SY22 and compare these findings to further literature. Nicholls et al. [2024] obtained atmospheric compositions from modelling the time-evolution of magma ocean worlds across Gyr timescales using a coupled interior-atmosphere model. They varied the hydrogen budget, mantle oxidation state and $\mathrm{C/H}$ ratio, and report atmospheric compositions for non-solidified planets in terms mole fractions for $\mathrm{H_2O}$, $\mathrm{CO}$, $\mathrm{CO_2}$, $\mathrm{CH_4}$, $\mathrm{N_2}$ and $\mathrm{H_2}$. They find that $\mathrm{CO}$ and $\mathrm{CO_2}$ dominated atmospheres are produced for $\mathrm{C/H}$ > 1.0 and $f_{O2} \geq \Delta IW - 1$. For $\mathrm{C/H} \approx$ 0.01, atmospheres remain largely $\mathrm{H_2}$ dominated except at high oxidation states ($f_{O2} \geq \Delta IW + 0$) where they come increasingly rich in $\mathrm{CO}$ and $\mathrm{CO_2}$. They find that the abundances of carbon-species are $\mathrm{CO} > \mathrm{CO_2} >> \mathrm{CH_4}$ in most cases, with $\mathrm{CO_2}$ becoming the most important atmospheric carbon reservoir for higher oxygen fugacities.

The findings of Nicholls et al. [2024] are in line with the compositions presented in Figure 25; a more oxidized mantle with $\mathrm{Mg/Si} \approx$ 0.75 (left panels) corresponds to a mantle oxygen fugacity of $\approx \Delta IW - 1$, at which point the atmosphere is $\mathrm{CO}$ and $\mathrm{H_2O}$ dominated by weight. In terms of mole fractions, the atmosphere goes from 97% $\mathrm{H_2}$ at

$T_s = 1000$ K to $63\%$ at $T_s = 2200$ K, which is in line with their results for $f_{O2} = \Delta IW - 1$ and a $\mathrm{C/H}$ ratio of 0.1. Nicholls et al. [2024] notes that bulk of $\mathrm{H_2O}$ in the planet remains dissolved in the mantle. Figures 16 and 21 corroborate this, with melt-phase $\mathrm{H_2O}$ being a more abundant reservoir of $\mathrm{H}$ than atmospheric $\mathrm{H_2O}$ for both increasing surface temperatures or increasing core-mantle equilibration temperatures. Nicholls et al. [2024] report $\mathrm{CH_4}$ to be a minor fixture in almost all atmospheres, with its mixing ratio maximized for the most reduced and $\mathrm{H}$ abundant planets. All of my modelling is performed with high hydrogen endowment and a mantle composition below the $\Delta$IW buffer, and $\mathrm{CH_4}$ is a steady fixture at about 1 wt% in the atmosphere when $T_{eq} < 4000$ K, in agreement with their findings.

My atmospheric compositions' variability with surface temperature and mantle composition can be further compared to results by Seidler et al. [2024], who studied the compositions of 'mineral' atmospheres as produced by equilibration with a molten silicate mantle. They note $\mathrm{SiO}$, $\mathrm{Mg}$ and $\mathrm{Fe}$ as the primary atmospheric constituents for reducing mantles ($f_{O2} < \Delta IW$), with the abundance of $\mathrm{SiO}$ increasing significantly as $T_s > 2500$ K, in accordance with my findings here. Seidler et al. [2024] also note that the influence of composition on the resulting abundance is more or less linear. Planets with slightly varying $\mathrm{Mg}$ / $\mathrm{Si}$ ratios will have very similar abundances for the resulting gas species ($\mathrm{Si}$, $\mathrm{SiO}$, $\mathrm{SiO_2}$, $\mathrm{Mg}$, $\mathrm{MgO}$ in their model). I notice similar behaviour in my comparison of various $\mathrm{Mg/Si}$ compositions, as the overall abundance of $\mathrm{SiO}$ is similar across the two models shown in Figure 25. In compositions extremely deficient in $\mathrm{SiO_2}$, Seidler et al. [2024] obtain atmospheres dominated by $\mathrm{Mg}$ and $\mathrm{MgO}$ over $\mathrm{SiO}$. While my limited modelling in this direction supports this trend, my model currently does not incorporate gas-phase $\mathrm{MgO}$. This result would be a viable validation for a future version of the model that incorporates a wider variety of atmospheric species.

## 4.2 Implications for Observations

### 4.2.1 Core Densities and the Mass-radius Relationship

A recurring result from my models that incorporate a reactive metal core, is the ingress of $\mathrm{Si}$, $\mathrm{O}$ and $\mathrm{H}$ into the core. This has implications for the density of the metal core, which will necessarily be lower for a core consisting of a $\mathrm{Si}$ / $\mathrm{O}$ / $\mathrm{H}$ alloy than that of a pure $\mathrm{Fe}$ core. This result was investigated in close detail by SY22, who note that these density deficits add a layer of degeneracy to the mass-radius relationship for exoplanets, and show that the ingress of lighter elements into metal cores can account for differences in inferred densities of rocky exoplanets.

These density deficits express themselves as a percentage decrease compared to the density of a pure $\mathrm{Fe}$ core, $\rho_0$. To compute these deficits, I use the same method applied by SY22, who approximated the reductions of $\rho_0$ as $8.7\%$ per wt% of $\mathrm{H}$, $1.2\%$ per wt% of $\mathrm{O}$ and $0.8\%$ per wt% of $\mathrm{Si}$ in the metal, based on results from Li et al. [2019] ($\mathrm{H}$) and Huang et al. [2019] ($\mathrm{O}$). Hence I compute the metal density deficit based on

experimental values as follows:

$$\delta_{\%} = 100 \cdot \frac{\rho_0 - \rho}{\rho_0} = 8.7(\text{wt\% H}) + 1.2(\text{wt\% O}) + 0.8(\text{wt\% Si})$$

In Figure 30 I illustrate the effects of varying surface temperature and core-mantle equilibration temperature on these density deficits, as the influence of these parameters on this parameter had not been explored further in previous work. The core-mantle equilibration temperature has a significant effect on these deficits, as more hydrogen and oxygen are driven into the metal core for higher $T_{eq}$; the increased density deficits are correlated strongly in particular to the amount of oxygen in the metal, as it reaches similar concentrations to hydrogen but is eight times heavier. In my hottest case, I obtain deficits of approximately 70%, while the coldest case modelled here gives a deficit of 12%.

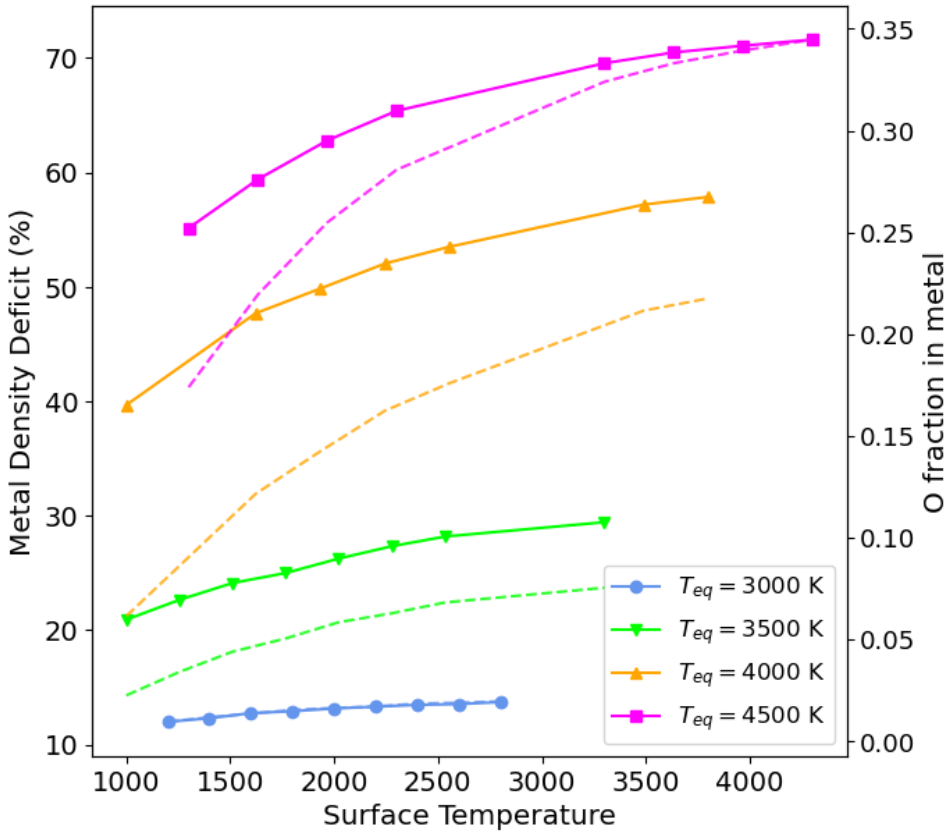


**Figure 30: Density deficits under increasing surface temperature**. **Solid lines**: Experimental deficit of the metal core compared to the density of pure $\mathrm{Fe}$ for a $4M_{\oplus}$ planet. Colored lines show the effect of increasing $T_{eq}$. **Dashed lines:** Mole fraction of oxygen in the metal phase for the same models, with values displayed on the additional y-axis.

Overall, the deficits reported by SY22 are far smaller on average than those I report at similar temperatures. For instance, at $T_{eq} = 4500$ K, I obtain deficits ranging from 55 to 70%, while they report deficits of approximately 12% at those temperatures. Given that my modelling of lighter planets showed the melt and metal compositions to

be largely unaffected by planet mass, I expect these density deficits to be a relevant result for both lighter super-Earths and more massive sub-Neptunes. Depending on the composition of the metal core, planets of similar masses may have varying radii due to the under-dense core, indeed giving a layer of degeneracy to the mass-radius relationship.

It should be noted that the applied density decreases due to $\mathrm{O}$ and $\mathrm{H}$ in the metal are based on experimental values from which the modelling extrapolates. For example, the values inferred from Huang et al. [2019] are based on $\mathrm{Fe\text{-}Si\text{-}O}$ ternaries at 3800 - 4800 Kelvin and a pressure of 136 GPa, yet several of my models here run for substantially lower temperatures. It is therefore disputable how applicable this method of computing density deficits is. In addition, the true amount of material that is able to ingress into the metal core is inhibited by the efficiency of vertical transport throughout the planet, which this model does not account for. As such these deficits should be regarded as upper limits at most.

### 4.2.2 Atmospheric Measurements

The effects of global chemical equilibration on the atmospheric composition of these modelled exoplanets are extensive, so here I consider to what extent these results may inform exoplanet observations. Remote observations of the interior is clearly not possible, so of particular interest are potential trends in the atmosphere that stem from the underlying core and mantle interactions, so that these atmospheric trends may inform us on the planetary interior.

I begin by identifying key species in my resultant atmospheres. For my models with reactive metal cores, I broadly distinguish two scenarios. In the first, high core-mantle equilibration temperatures (> 4500 K) drive the majority of the atmosphere into the melt and metal reservoirs, and what remains is mainly $\mathrm{CO}$ and $\mathrm{H_2O}$ followed by $\mathrm{CO_2}$, and smaller amounts of $\mathrm{H_2}$, $\mathrm{Na}$, $\mathrm{Mg}$ and $\mathrm{SiO}$. For colder core-mantle equilibration temperatures ($T_{eq} \approx 3000$ K), a thick $\mathrm{H_2}$ atmosphere is retained, with significant amounts of $\mathrm{H_2O}$, $\mathrm{SiH_4}$, $\mathrm{CH_4}$ and less than 1 wt% $\mathrm{SiO}$ and $\mathrm{Mg}$. Hotter core-mantle equilibration temperatures drive most of the carbon into the oxides, while lower core temperatures result in $a$ 1 wt% $\mathrm{CH_4}$ in the atmosphere throughout. $\mathrm{H_2O}$ remains a fixture in these equilibrated atmospheres irrespective of $T_{eq}$. As stated previously, the presence of $\mathrm{Na}$ and $\mathrm{SiO}$ is expected in atmospheres stemming from outgassing by a molten silicate melt, making the observability of these species of keen interest to us. Lastly, for a planet with a chemically isolated core, my unreactive modelling points to an atmosphere with roughly equal parts $\mathrm{H_2}$, $\mathrm{H_2O}$ and $\mathrm{SiH_4}$, and far more $\mathrm{SiO}$ than a planet with a reactive core and all else kept equal.

The prevalence of $\mathrm{H_2O}$ in my model atmospheres is an important result. SY22 highlighted numerous pathways for water to form given the reaction network outlined in this model, whether or not the metal core is able to equilibrate with the overlying mantle. My results, summarized in Figures 13 ($T_s$), 18 ($T_{eq}$) and 28 (unreactive metal

core) corroborate this. In all cases, between $\sim$ 1 and 10wt% of the atmosphere is water vapor. As mentioned in the introduction, even moderate amounts of water vapor in (proto)planetary atmospheres can significantly increase the cooling timescale of the melt, due to its effectiveness as a greenhouse gas. The modelling by Hamano et al. [2015], which was performed for similar temperature ranges as those considered in this thesis, concludes that a water vapor abundance of $\sim$ 1wt% to be sufficient to sustain a magma ocean for Gyr timescales provided the planet is within a critical distance from its host star at which stellar irradiation exceeds the atmosphere's radiation limit. My results therefore contribute to the picture that magma-ocean exoplanets may sustain a globally molten mantle for up to Gyr timescales.

Hamano et al. [2015] additionally provide predictions for the observability of steam atmospheres such as those predicted by my model atmospheres with direct imaging. The hot planetary surface would lead to visible and near-IR emission, part of which would be absorbed by the steam in the atmosphere. Some thermal radiation passes through atmospheric windows, with two benchmarks for direct detectability being a sufficiently large planet-to-star contrast in terms of their emitted flux, and the orbital angular separation. Hamano et al. [2015] predicted that close-in exoplanets with such water-rich atmospheres would be favourable targets for direct imaging, as the planet-to-star ratio in the infrared K-band (centered on 2.2 µm) exceeds conservative detection limits for the entirety of the magma ocean lifetime, which is comparable to the main-sequence lifetime of the host star. Angular separation represents the main challenge for detection, with upcoming Extremely Large Telescopes possibly providing the means to resolve planets within 10 pc.

The observabilities of the remaining atmospheric species with JWST have been demonstrated by recent works. The atmosphere of sub-Neptune TOI-270d was recently characterized via a full JWST NIRSpec transmission spectrum from 0.6 to 5.2 µm by Benneke et al. [2024], showing five vibrational bands for $\mathrm{CH4}$ as well as signatures for both $\mathrm{CO_2}$ and $\mathrm{H_2O}$, which immediately highlights their potential detectability with present instrumentation. Both $\mathrm{H_2O}$ and $\mathrm{CO_2}$ show absorption features in the infrared due to their vibrational transitions, although they may overlap and be difficult to distinguish from each other when present in similar abundances, as is the case in my reactive core models when $T_{eq} \approx 4500$ (Figure 25). It should also be noted that my modelling points to water vapor being abundant in most cases for an equilibrated magma-ocean planet, and so it may not prove useful as a diagnostic when hoping to distinguish between planets with differing melt compositions or interior temperatures. The observability of $\mathrm{SiH_4}$ is more questionable. A gas-melt equilibrium study performed by Falco et al. [2024] investigated the atmospheric structure and observational implications of hot rocky exoplanets with atmospheres of varying hydrogenation. They likewise report that $\mathrm{SiH_4}$ may be an abundant species in these atmospheres when there is sufficient hydrogen in the primary atmosphere, but note that $\mathrm{SiH_4}$ tends to dissociate at higher altitudes. Any $\mathrm{SiH_4}$ is therefore locked to the deeper layers of the atmosphere, close to the magma ocean surface, where its spectral features would be unobservable.

## 4.2 Implications for Observations

The molecular and atomic silicate species have prominent features in the near-to-mid infrared. A study by Zilinskas et al. [2022] modelled outgassed equilibrium chemistry for short-period rocky exoplanets in order to ascertain JWST observability of species in the atmospheres of these partially molten worlds. They identify $\mathrm{SiO}$, $\mathrm{SiO_2}$, $\mathrm{MgO}$ and $\mathrm{Na}$, as among the strongest absorbers in silicate-rich atmospheres. For $\mathrm{Na}$, a large portion of the opacity comes from a strong doublet at 0.6 µm, while most of its spectral features towards the infrared are noticeably weaker. The low abundance of $\mathrm{Na}$ in my modelled atmospheres will make its detection challenging, especially as its strongest feature lies in the optical regime rather than the infrared, just on the edge of JWST's wavelength coverage. $\mathrm{SiO}$ shows strong absorption between 0.2 and 10 µm, split into four separate features that should be detectable with JWST given sufficient abundance in the atmosphere, although there is debate regarding its 9 µm band, which may be a prominent emission source instead due to thermal inversions in the atmosphere. Seidler et al. [2024] backs up the infrared visibility of $\mathrm{SiO}$ and $\mathrm{SiO_2}$, and further highlights a broad $\mathrm{MgO}$ feature at 6 µm .

Given the detectability of numerous key species in these resultant atmospheres, I will highlight a few trends that are potentially distinguishable with current instruments. First, modelling the core-mantle equilibration temperatures invariably leads to atmospheres dominated by $\mathrm{CO}$ and, to a lesser extent, $\mathrm{CO_2}$. For $T_{eq} \geq 4000$, $\mathrm{H_2}$ cedes dominance to the carbon oxides and water. The abundance of $\mathrm{CO}$ and $\mathrm{CO_2}$ will be tied to the $\mathrm{C/H}$ ratio of the planet, which is very small in my model compositions ($\approx 0.01$), and is brought to the forefront in my models due to large amounts of the atmosphere being recycled into the planetary core, leaving a thin, tenuous atmosphere. Nevertheless, a high abundance of $\mathrm{CO}$ and $\mathrm{CO_2}$ in magma-ocean exoplanet atmospheres may point to a hotter planetary interior.

Connecting atmospheric observations to the oxygen fugacity of the silicate mantle is possible given my results when one looks at the relative abundances of $\mathrm{SiO}$ and $\mathrm{Mg}$ in the atmosphere; for a more reducing mantle (as represented by the $\mathrm{Mg/Si}= 2.1$ models in Figures 23 and 25), $\mathrm{Mg}$ enters the atmosphere at wt% levels even at lower core-mantle equilibration temperatures, for $T_s = 3000$ K. Inclusion of at least $\mathrm{MgO}$ in the atmosphere is necessary to make this connection more robust, and in my current results I can only use the presence or absence of $\mathrm{Mg}$ to constrain the melt's $\mathrm{Mg/Si}$ towards higher values.

While Schlichting and Young [2022] noted the dominance of either $\mathrm{SiO}$ or $\mathrm{H_2}$ as a potential diagnostic for planets with or without a reactive metal core, I cannot claim the same from my results; $\mathrm{H_2}$ remains dominant in the atmospheres for $T_s = 3000$ K for both reactive and unreactive models. However, the abundances of $\mathrm{H_2O}$, $\mathrm{SiH_4}$ and $\mathrm{SiO}$ are markedly higher in an unreactive model, as the absence of a sink for $\mathrm{H}$, $\mathrm{O}$ and $\mathrm{Si}$ enables their buildup. So while I would expect hydrogen to remain the most abundant species in the atmosphere of an equilibrated magma-ocean planet, a lower $\mathrm{H/Si}$ ratio may be a potential tool to investigate the reactivity of the metal core of the planet. Furthermore, Figures 16 and 21 show that while it is feasible to estimate a

sub-Neptune's hydrogen budget from its atmosphere alone for systems with a cooler interior ($T_{eq} < 3500$ K), this may become less valid for hotter core-mantle boundaries, as my modelling indicates that ingress of $\mathrm{H}$ into the metal phase becomes progressively more important as $T_{eq}$ is increased.

The results of Zilinskas et al. [2022] and Seidler et al. [2024] in indicating several of these species as prominent spectral features for magma-ocean atmospheres highlights the importance of including more vaporized silicates in the atmospheric reservoir of my model, notably $\mathrm{SiO_2}$, $\mathrm{FeO}$ and $\mathrm{MgO}$. $\mathrm{SiO_2}$ has strong absorption features in the mid-infrared, which do not blend with those of $\mathrm{SiO}$, highlighting its importance as an atmospheric feature for modelling the observability of an equilibrated molten exoplanet. Additionally, Seidler et al. [2024] highlight the connections between the spectral features of $\mathrm{SiO}$ and $\mathrm{MgO}$ and the oxygen fugacity of the underlying melt. The prominent features of $\mathrm{SiO}$ in atmospheric spectra of magma-ocean planets are strongest under reducing melt conditions, and vanish for highly oxidized melts as the atmosphere becomes dominant by $\mathrm{O}$ and $\mathrm{O_2}$ instead. Furthermore, the line ratio between $\mathrm{SiO}$ at 9 µm and $\mathrm{MgO}$ emission at 6 µm is a strong diagnostic feature for $f_{O2}$, observable with current and upcoming missions such as JWST and Ariel. An extension of the atmospheric chemistry in this model would significantly increase its relevance to observations of close-in exoplanets.

## 4.3 Validity of results

### 4.3.1 Estimation of Uncertainties

I have made attempts to estimate uncertainties in my results in two ways, as described in section 2. These uncertainties are reported to the user after each model run, and included in the output files for further use. I computed uncertainties in two distinct ways. The first is to retrieve the results of the 500 next-highest posterior probability samples from the MCMC search, in an attempt to sample from a region around the global minimum. I then compute a standard deviation from these samples for each parameter and apply this as an uncertainty on the MAP result. This method is only statistically valid if the 500 next-best samples are distributed roughly symmetrically around the MAP, and when the MAP itself coincides with the mean of that distribution. As I illustrated in Figure 9, this is not the case for all parameters in a model run; as such, using this method of estimating uncertainties is not always valid. Another approach utilized is to compute the 16th, 50th and 84th percentile values for each variable, taking data from the entire range of samples. This will necessarily include samples drawn from areas outside of the global minimum, which likewise makes this method not representative of any true error on the MAP results.

The uncertainties are not represented in my figures, as they are small relative to the expectation value if the MCMC run converges towards the global minimum of the objective function. For the weight-percentage abundances of species, the average relative error is less than 2%, which is not visible under the scales used in my figures. To

gauge the performance of the model, it is more informative to instead inspect the sampled distributions for each parameter, and their correlations, through the use of a corner plot. These plots show the sampled distributions for each individual parameter on the diagonal, and 2D contour plots between pairs of parameters on the off-diagonals. As the full 30x30 corner-plot is too large to display and keep legible, I show a portion of the full corner plot for several melt species in Figure 31. The selection is intended to allow for a visual interpretation of the model's performance, which is well-represented by this portion.

If the MCMC run has converged, the walkers should have successfully moved to the global minimum and sampled from the posterior probability density. One would then expect smooth, Gaussian-like distributions for each parameter, with clear peaks and no multimodality. After 300,000 iterations for an ensemble of 200 walkers, such smooth distributions are produced for each parameter in Figure 31, suggesting convergence. Some parameters, such as $\mathrm{Na_2SiO_3}$ here, show some skew in the tail of their sampled distribution, which goes to show that the sampling may not be equally successful for all parameters. Asymmetric uncertainties indicated at the top of each histogram stem from the 68% confidence interval, similar to what I compute following each run.

The contours on the off-diagonal inform us about potential correlations between pairs of parameters. They can be regarded as 2D representations of the individual marginalized distributions, as though the top histogram were the flattened projection of the contour plot's horizontal axis, and likewise for the other histogram and the vertical axis. Therefore uncorrelated, well-sampled variables will show round contours, centered at the peaks of the individual distributions. Elliptical contours instead point to some degree of correlation, as can be seen for $\mathrm{MgO}$ and $\mathrm{MgSiO_3}$: samples with lower mole fractions of $\mathrm{MgO}$ concurrently sample higher fractions of $\mathrm{MgSiO_3}$. The contours are smooth and show correlations that I would expect, which again would suggest a reliable result for this MCMC run. I do note some isolated blobs and splotches in these contours, which arise from walker samples from possible local minima rather than the global minimum.

Not each cornerplot indicates good convergence, and occassionally the model fails to settle into the global minimum. In those cases, the distributions on the diagonal are flat or show numerous indistinguishable peaks, and disorganized, irregular shapes dominate the joint distributions. Although uncommon, it is possible for the model to return statistics ($\chi^2$, $a_f$, $R$) suggesting a good fit, despite the cornerplot showing irregular contours and multimodal individual distributions. Examples of such cornerplots are provided in Appendix B (Figures 35 and 36). One interpretation of this is that only a few walkers have converged to the global minimum, with most samples stemming from local minima in close proximity to the global minimum of the objective function. In that case, the contour plot will indicate poor convergence, yet the evaluated MAP still stems from the global minimum.

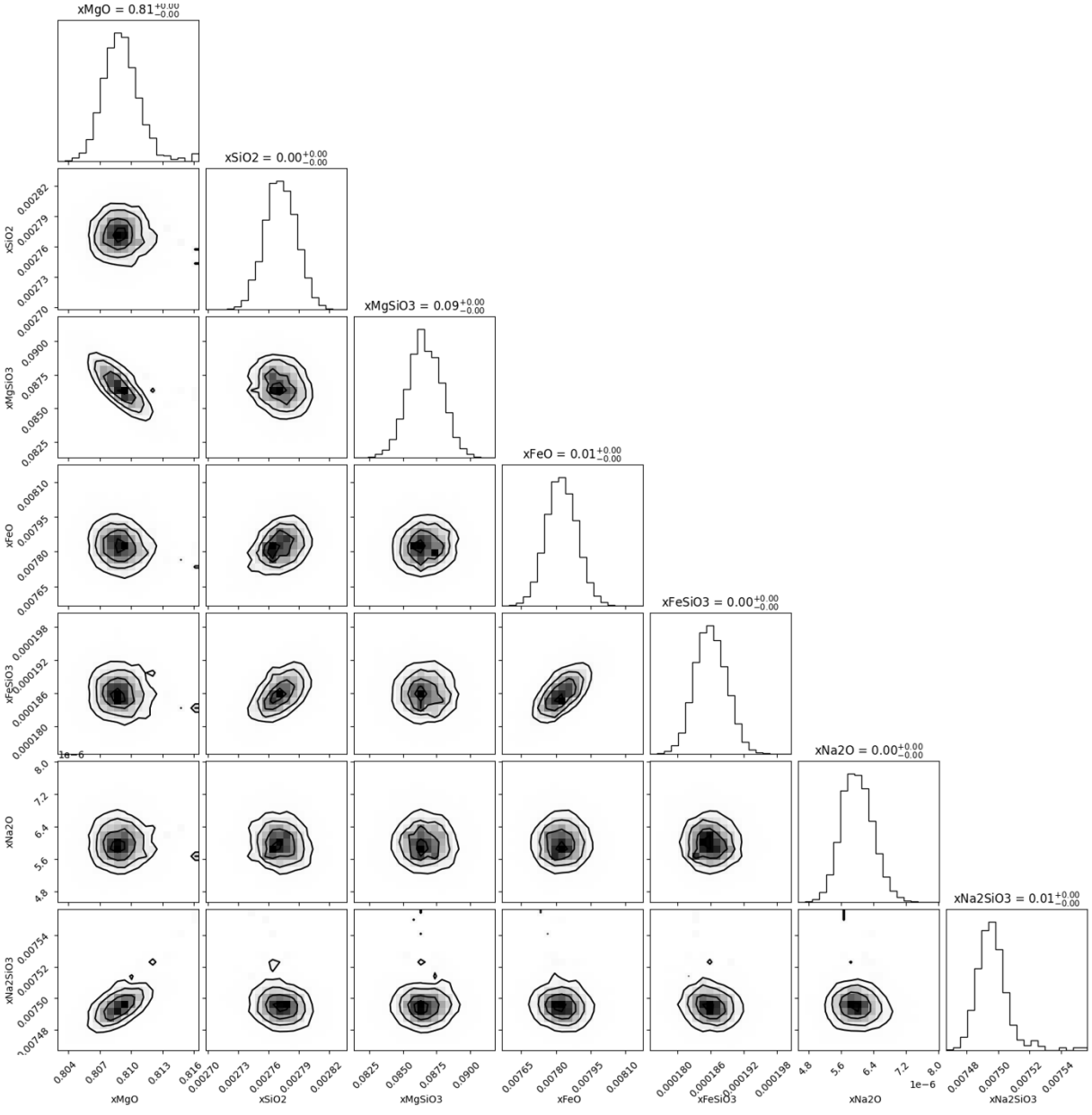


**Figure 31: 7x7 Cornerplot following converged MCMC run**. Sampled 1D distributions and 2D contours are shown on the diagonal and off-diagonal respectively. Shown are distributions for melt-species $\mathrm{MgO}$, $\mathrm{SiO_2}$, $\mathrm{MgSiO_3}$, $\mathrm{FeO}$. $\mathrm{FeSiO_3}$, $\mathrm{Na_2O}$ and $\mathrm{Na_2SiO_3}$. These results stem from a model run with $T_s = 2000$ K; $T_{eq} = 5000$ K, and evaluated a reduced $\chi^2$ statistic $\chi^2 = 0.147$.

As such, my conclusion is that the model is well-behaved and shows signs of good convergence in optimal cases, although it is not uncommon for the model to struggle to converge to a global minimum. Evaluating the MAP in this case can still lead to an appropriate solution, with good statistics and behaviour in line with expected trends from adjacent model runs in the parameter grid. Since the objective function contains numerous weights and penalty functions which can be finely tuned, it is possible to improve the model's performance for dedicated runs if time is invested in tuning

the weights to suitable values. For this thesis I utilized the same tunings as used by Schlichting and Young [2022].

### 4.3.2 Model Assumptions and Future Work

Several assumptions and simplifications are made in this model, the impact and validities of which are described in more detail by Schlichting and Young [2022]. Here I aim to examine some of this model's assumptions and shortcomings and discuss their impact on my results.

The model considers the entire planet to be in constant chemical contact: all material in the atmosphere, silicate mantle and metal core is able to undergo chemical exchange and reach chemical equilibrium. This ties in with the assumption that the silicate mantle is entirely molten, making the full mantle reservoir available for equilibration. In addition, the model assumes nothing about the planet's interior structure, beyond tracking how much of each species is tied to the atmosphere, melt or metal phase. The mole fraction of $\mathrm{Fe}$ in the metal, $x_{Fe}^{metal}$, does not distinguish between iron contained in a differentiated core or smaller droplets entrained in the magma ocean, as described by Lichtenberg [2021].
A key issue with these assumptions is that the amount of material across the planetary reservoirs that is able to chemically equilibrate is likely smaller in reality. Chemical equilibration occurs only at the interfaces between these phases. While a turbulent, strongly convective mantle may circulate enough of its material to achieve near or complete chemical equilibration with the overlying atmosphere, it is doubtful whether full equilibration between cores and mantles will be attained. The reactive and unreactive models are the edge cases of this scenario, with a possibly more realistic scenario seeing a fraction of the material between the melt and metal core equilibrating. Abundances of $\mathrm{H_2O}$ in the melt and $\mathrm{SiO}$ will likely be inversely correlated to the degree of equilibration between the mantle and core, assuming the transport of $\mathrm{H}$ and $\mathrm{Si}$ towards the metal core is efficient. If less of these light elements are able to partition into the melt, the results will tend towards those presented in Figure 28.

Likewise, the thermal evolution of the silicate mantle itself is not considered here, as my modelling provides a snapshot of the planet's composition once chemical equilibration is reached. The assumption of a global magma ocean is likely valid for primordial magma oceans, which remain so hot from accretion that they are likely molten across the planet and towards significant depth [Dorn and Lichtenberg, 2021]. How much of the mantle remains molten depends on a multitude of factors, including stellar irradiation, the degree of convection in the mantle, transport of volatiles into the atmosphere, and the presence of greenhouse gases such as $\mathrm{H_2O}$ and $\mathrm{CO_2}$. It is a common assumption that the mantle crystallizes in a bottom-up scenario, with the outer surface remaining largely molten from a mix of irradiation and runaway greenhouse effects given a thick steam or carbon-dominated atmosphere. Increased pressure towards the planetary interior makes it possible for the lower portions of the melt to crystallize, stopping core-mantle equilibration as the core becomes chemically isolated. The convective velocities in the mantle will decrease as the solid fraction increases, possibly

inhibiting atmosphere-mantle equilibration as a result, since less of the mantle material will circulate into contact with the atmosphere [Lichtenberg, 2021]. These effects would likely manifest different observable trends for super-Earths and sub-Neptunes, as the latter planets have higher internal pressures due to their higher masses, possibly leading to faster core isolation, yet also enjoy thicker atmospheres that may drive higher surface temperatures and even permanent magma oceans.

Furthermore, I consider these model planets in full isolation, as a 'closed-box' model; infall or escape of material is not considered, which is a necessary but impactful simplification. Ingress of new material through impacts may be the primary delivery method for the bulk volatile inventory of close-in rocky exoplanets, which are thought to accrete in mostly dry regions [Venturini et al., 2020b]. On the other end, atmospheric escape is crucial to incorporate especially for highly irradiated planets, as UV-driven escape is a strong controller of the atmosphere's relative size and composition. On a related topic, the composition and structure of the atmosphere will be influenced significantly by the stellar irradiation, which will drive photochemical reactions that are currently not considered in the model. To further infer the observability of any trends suggested by the atmosphere-mantle equilibration, these photochemical reactions must be accounted for to obtain a more complete picture of the potential atmospheres we may remotely detect.

Finally, there are several numerical caveats to this model. As discussed previously, the model's objective function incorporates numerous weight coefficients and penalties that can be tuned to improve the convergence of the Simulated Annealing search, and consequently enhance the MCMC sampling. The current tunings in my default configuration file provide satisfactory results for most of the modelling cases presented in this work. I invite the curious reader to examine the default configuration files on the model's GitHub Repository. However, numerical instabilities at temperatures below 3000 K are present in Figures 28 and 29, as I did not tune the objective function for the unreactive core modelling. This goes to show that the model can be numerically improved in several ways. In addition, the Shomate coefficients used to compute the Gibbs free energies are defined for temperatures no lower than 298 K and no higher than 6000 K, and are based on outdated chemical data. As such, the model likely extrapolates at higher temperatures. Finally, the abundances reported for trace species - those with wt% lower than $\sim 10^{-5}$, should be taken with a grain of salt. My requirement for a successful model run is a deviation from the initial amount of moles of no more than $0.006\%$ for each element, hence small abundances may fall within the error margin prescribed to the amount of moles of each element in the system.

Future adaptations to this model should focus on improving the convergence of the Simulated Annealing and MCMC searches, in order to make large-scale modelling more flexible and robust. I made limited attempts to improve the model's efficiency in runtime, with current models taking roughly 70 minutes on average for 50,000 SA iterations and 300,000 MCMC samples drawn. Applying methods such as Just-In-Time compiling, or improving the MCMC search to allow for a smaller number of samplings,

could help to shorten the model's runtime. Coupling this chemical-equilibrium model to models of magma ocean interior dynamics and structure, as well as atmospheric escape models, will allow us to model the evolution of a magma-ocean planet in a self-consistent manner, providing a clearer picture of the nature of these planet types. With my contributions to the model's modularity and clarity, I hope to have made such pursuits more feasible.

# 5 Conclusions

In this thesis, I investigated the interior geochemistry relevant for globally molten super-Earths and sub-Neptunes through the use of a chemical equilibrium model. Building on previous literature, I utilize a reaction network spanning 19 basis reactions for 26 chemical species in terms of their mole fractions, spread across the planetary atmosphere, molten silicate mantle and metal core. These phases are allowed to reach full chemical equilibrium with each other, allowing for inspection of the resulting planetary composition under various parameters of interest, most notably the surface temperature, core-mantle equilibration temperature, silicate composition, planet mass and core reactivity. My modelling reveals several notable trends:

- In all cases, the effect of chemical equilibration is to increase the oxidation state of the atmosphere as parts of the silicate mantle evaporate into the atmosphere. The silicate mantle becomes more reduced for most cases, but stays more oxidized than the atmosphere at lower surface temperatures.
- The main effect of increasing the core-mantle equilibration temperature is to recycle large amounts of the atmosphere into the planetary interior for $T_{eq} \geq 4000$ K, leaving behind a tenuous atmosphere that is dominated by $\mathrm{CO}$ and $\mathrm{H_2O}$, with the metal phase containing large abundances of $\mathrm{H}$, $\mathrm{O}$ and $\mathrm{Si}$. The abudance of $\mathrm{CO}$ in the atmosphere may be a potential tracer of interior temperature.
- As surface temperature increases, the atmosphere becomes progressively more abundant in $\mathrm{H_2O}$, $\mathrm{SiO}$ and more silicate evaporates at $T_s > 3500K$, including $\mathrm{Na}$, $\mathrm{Mg}$ and $\mathrm{Fe}$ in the hottest cases. Some of these, most notably $\mathrm{SiO}$, have prominent mid-infrared features that could be observable with current and upcoming instruments such as JWST and Ariel. Detection of $\mathrm{SiO}$ and abundance measurements of $\mathrm{CO}$ may allow us to distinguish magma-ocean equilibrated systems from non-equilibrated atmospheres, and inform us of their interior temperatures.
- In the unreactive core case, where the metal core is unable to chemically interact with the rest of the system, the abundances of $\mathrm{SiO}$, $\mathrm{SiH_4}$ and $\mathrm{H_2O}$ in the atmosphere are increased significantly compared to the reactive case, as there is no metal sink for $\mathrm{Si}$ and $\mathrm{O}$. However, unlike the findings from previous studies applying this model, my results do not suggest that one can use the dominance of either $\mathrm{SiO}$ (reactive) or $\mathrm{H_2}$ (unreactive) as an observational diagnostic for these distinct cases.

Coupling this model to simulations of magma ocean interior dynamics and structure, as well as models incorporating atmospheric escape and photochemistry, is crucial in order to obtain a self-consistent picture of magma-ocean exoplanet's chemical evolution over Gyr timescales. This will further inform us of their observability with current and future instruments, potentially allowing remote observations of their atmospheres to provide insights into their interior structures, oxidation states and volatile inventories. This in turn will illuminate lingering questions regarding super-Earth and sub-Neptune formation and differentiation, the origin of the Radius Valley, and provide a window into Earth's past, when it too was a molten planet.

**Acknowledgements**

This research has made use of the NASA Exoplanet Archive, which is operated by the California Institute of Technology, under contract with the National Aeronautics and Space Administration under the Exoplanet Exploration Program.

I would like to thank Prof. Dr. Edward D. Young for making the latest version of his chemical equilibrium model available to me, as well as for the explanations and insight he offered throughout the project.

My sincerest gratitude goes out to Dr. Tim Lichtenberg and Dr. Rob Spaargaren for the advice, expertise, patience, humour and support they have provided me over the course of this thesis. It was a pleasure to work with both of you!

Lastly, this work would have been impossible without the love and support of dozens of fellow students, both within and beyond the disciplines of astronomy and planetary science. Thank you all for helping me refine my writing, re-think my plots, and for providing me with an ample supply of life-saving coffee.

Likewise, I would not have managed to complete this thesis in good health and good spirits without the care and encouragement of my family, friends, and dog. Thank you for reminding me to drink enough water, and for lying on my feet to keep me from getting up. It kept me focussed and on track and helped me bring this project to a conclusion. You are all amazing.

# References

Alex Wolszczan and Dale A. Frail. A planetary system around the millisecond pulsar psr1257 + 12. *Nature*, 355:145–147, 1992. URL https://api.semanticscholar.org/CorpusID:4260368.

Michel Mayor and Didier Queloz. A jupiter-mass companion to a solar-type star. *Nature*, 378:355–359, 11 1995. doi: 10.1038/378355a0. URL https://www.nature.com/articles/378355a0.

Jessie L Christiansen, Douglas L McElroy, Marcy Harbut, David R Ciardi, Megan Crane, John Good, Kevin K Hardegree-Ullman, Aurora Y Kesseli, Michael B Lund, Meca Lynn, Ananda Muthiar, Ricky Nilsson, Toba Oluyide, Michael Papin, Amalia Rivera, Melanie Swain, Nicholas D Susemiehl, Raymond Tam, van Eyken, and Charles Beichman. The nasa exoplanet archive and exoplanet follow-up observing program: Data, tools, and usage, 2025. URL https://arxiv.org/abs/2506.03299v1.

Saloni Bhatiani, Xinyu Dai, and Eduardo Guerras. Confirmation of planet-mass objects in extragalactic systems. *The Astrophysical Journal*, 885:77–77, 11 2019. doi: 10.3847/1538-4357/ab46ac.

Aaron C. Rizzuto, Elisabeth R. Newton, Andrew W. Mann, Benjamin M. Tofflemire, Andrew Vanderburg, Adam L. Kraus, Mackenna L. Wood, Samuel N. Quinn, George Zhou, Pa Chia Thao, Nicholas M. Law, Carl Ziegler, and César Briceño. Tess hunt for young and maturing exoplanets (thyme). ii. a 17 myr old transiting hot jupiter in the sco-cen association. *The Astronomical Journal*, 160:33, 06 2020. doi: 10.3847/1538-3881/ab94b7.

Benjamin J. Fulton, Erik A. Petigura, Andrew W. Howard, Howard Isaacson, Geoffrey W. Marcy, Phillip A. Cargile, Leslie Hebb, Lauren M. Weiss, John Asher Johnson, Timothy D. Morton, Evan Sinukoff, Ian J. M. Crossfield, and Lea A. Hirsch. The california-keplersurvey. iii. a gap in the radius distribution of small planets. *The Astronomical Journal*, 154:109, 08 2017. doi: 10.3847/1538-3881/aa80eb.

J. M. Diederik Kruijssen, Steven N Longmore, and Mélanie Chevance. Bridging the planet radius valley: Stellar clustering as a key driver for turning sub-neptunes into super-earths. *The Astrophysical Journal Letters*, 905:L18–L18, 12 2020. doi: 10.3847/2041-8213/abccc3.

James E. Owen and Yanqin Wu. The evaporation valley in the kepler planets. *The Astrophysical Journal*, 847:29, 09 2017. doi: 10.3847/1538-4357/aa890a.

Sivan Ginzburg, Hilke E Schlichting, and Re'em Sari. Core-powered mass-loss and the radius distribution of small exoplanets. *Monthly Notices of the Royal Astronomical Society*, 476:759–765, 02 2018. doi: 10.1093/mnras/sty290.

Akash Gupta and Hilke E Schlichting. Sculpting the valley in the radius distribution of small exoplanets as a by-product of planet formation: the core-powered mass-loss mechanism. *Monthly Notices of the Royal Astronomical Society*, 487:24–33, 05 2019. doi: 10.1093/mnras/stz1230.

U. Marboeuf, Amaury Thiabaud, Yann Alibert, N Cabral, and W Benz. From planetesimals to planets: volatile molecules. *Astronomy and Astrophysics*, 570:A36–A36, 10 2014. doi: 10.1051/0004-6361/201423431.

Tim Lichtenberg and Yamila Miguel. Super-earths and earth-like exoplanets. *Treatise on Geochemistry*, pages 51–112, 2025. doi: 10.1016/b978-0-323-99762-1.00122-4. URL https://arxiv.org/abs/2405.04057.

Jacob L. Bean, Sean N. Raymond, and James E. Owen. The nature and origins of sub-neptune size planets. *Journal of Geophysical Research: Planets*, 126, 01 2021. doi: 10.1029/2020je006639.

Julia Venturini, Octavio M. Guilera, Jonas Haldemann, María P. Ronco, and Christoph Mordasini. The nature of the radius valley. *Astronomy Astrophysics*, 643:L1, 10 2020a. doi: 10.1051/0004-6361/202039141.

Nikku Madhusudhan, Subhajit Sarkar, Savvas Constantinou, Måns Holmberg, Anjali A. A. Piette, and Julianne I. Moses. Carbon-bearing molecules in a possible hycean atmosphere. *The Astrophysical Journal Letters*, 956:L13, 10 2023. doi: 10.3847/2041-8213/acf577. URL https://esawebb.org/media/archives/releases/sciencepapers/weic2321/weic2321a.pdf.

Hamish Innes, Shang-Min Tsai, and Raymond T Pierrehumbert. The runaway greenhouse effect on hycean worlds. *The Astrophysical Journal*, 953:168–168, 08 2023. doi: 10.3847/1538-4357/ace346.

Jérémy Leconte, Aymeric Spiga, Noé Clément, Sandrine Guerlet, Franck Selsis, Gwenaël Milcareck, Thibault Cavalié, Raphaël Moreno, Emmanuel Lellouch, Óscar Carrión-González, Benjamin Charnay, and Maxence Lefèvre. A 3d picture of moist-convection inhibition in hydrogen-rich atmospheres: Implications for k2-18b. *Astronomy astrophysics*, 686, 06 2024. doi: 10.1051/0004-6361/202348928.

Hilke E. Schlichting and Edward D. Young. Chemical equilibrium between cores, mantles, and atmospheres of super-earths and sub-neptunes and implications for their compositions, interiors, and evolution. *The Planetary Science Journal*, 3:127, 05 2022. doi: 10.3847/psj/ac68e6.

Tim Lichtenberg. Redox hysteresis of super-earth exoplanets from magma ocean circulation. *The Astrophysical Journal Letters*, 914:L4–L4, 06 2021. doi: 10.3847/2041-8213/ac0146.

Tim Lichtenberg, Laura Schaefer, Miki Nakajima, and Ronald Fischer. Geophysical evolution during rocky planet formation. *arXiv (Cornell University)*, 03 2022. doi: 10.48550/arxiv.2203.10023.

M. Ikoma, L. Elkins-Tanton, K. Hamano, and J. Suckale. Water partitioning in planetary embryos and protoplanets with magma oceans. *Space Science Reviews*, 214, 05 2018. doi: 10.1007/s11214-018-0508-3.

Don L Anderson. *Theory of the Earth*. Blackwell Scientific Publ, 1991.

Bernard J. Wood, Michael J. Walter, and Jonathan Wade. Accretion of the earth and segregation of its core. *Nature*, 441:825–833, 06 2006. doi: 10.1038/nature04763.

Harrison Nicholls, Tim Lichtenberg, Dan J. Bower, and Raymond Pierrehumbert. Magma ocean evolution at arbitrary redox state. *Journal of Geophysical Research: Planets*, 129, 12 2024. doi: 10.1029/2024je008576.

A. Vazan, C W Ormel, and C Dominik. Effect of core cooling on the radius of sub-neptune planets. *Astronomy astrophysics*, 610, 02 2018. doi: 10.1051/0004-6361/201732200.

Keiko Hamano, Hajime Kawahara, Yutaka Abe, Masanori Onishi, and George L. Hashimoto. Lifetime and spectral evolution of a magma ocean with a steam atmosphere: Its detectability by future direct imaging. *The Astrophysical Journal*, 806: 216, 06 2015. doi: 10.1088/0004-637x/806/2/216.

Marc M. Hirschmann. Magma ocean influence on early atmosphere mass and composition. *Earth and Planetary Science Letters*, 341-344:48–57, 08 2012. doi: 10.1016/j.epsl.2012.06.015.

D.C. Rubie, H.J. Melosh, J.E. Reid, C. Liebske, and K. Righter. Mechanisms of metal–silicate equilibration in the terrestrial magma ocean. *Earth and Planetary Science Letters*, 205:239–255, 01 2003. doi: 10.1016/s0012-821x(02)01044-0.

Nisha Katyal, Gianluigi Ortenzi, John Lee Grenfell, Lena Noack, Frank Sohl, Mareike Godolt, Antonio García Muñoz, Franz Schreier, Fabian Wunderlich, and Heike Rauer. Effect of mantle oxidation state and escape upon the evolution of earth's magma ocean atmosphere. *Astronomy Astrophysics*, 643:A81, 11 2020. doi: 10.1051/0004-6361/202038779.

Daniel J. Frost and Catherine A. McCammon. The redox state of earth's mantle. *Annual Review of Earth and Planetary Sciences*, 36:389–420, 05 2008. doi: 10.1146/annurev.earth.36.031207.124322.

Alexandre Corgne, Shantanu Keshav, Bernard J. Wood, William F. McDonough, and Yingwei Fei. Metal–silicate partitioning and constraints on core composition and oxygen fugacity during earth accretion. *Geochimica et Cosmochimica Acta*, 72:574–589, 01 2008. doi: 10.1016/j.gca.2007.10.006.

Björn Benneke, Pierre-Alexis Roy, Louis-Philippe Coulombe, Michael Radica, Caroline Piaulet, Eva-Maria Ahrer, Raymond Pierrehumbert, Joshua Krissansen-Totton, Hilke E Schlichting, Renyu Hu, Jeehyun Yang, Duncan Christie, Daniel Thorngren, Edward D Young, Stefan Pelletier, Heather A Knutson, Yamila Miguel, Thomas M

Evans-Soma, Caroline Dorn, Anna Gagnebin, Jonathan J Fortney, Thaddeus Komacek, Ryan MacDonald, Eshan Raul, Ryan Cloutier, Lorena Acuna, David Lafrenière, Charles Cadieux, René Doyon, Luis Welbanks, and Romain Allart. Jwst reveals $ch_4$, $co_2$, and $h_2o$ in a metal-rich miscible atmosphere on a two-earth-radius exoplanet. *arXiv (Cornell University)*, 03 2024. doi: 10.48550/arxiv.2403.03325.

Edward D. Young, Anat Shahar, and Hilke E. Schlichting. Earth shaped by primordial h2 atmospheres. *Nature*, 616:306–311, 04 2023. doi: 10.1038/s41586-023-05823-0. URL https://arxiv.org/pdf/2304.07845.pdf.

Bruce Fegley and A.G.W. Cameron. A vaporization model for iron/silicate fractionation in the mercury protoplanet. *Earth and Planetary Science Letters*, 82:207–222, 04 1987. doi: 10.1016/0012-821x(87)90196-8.

James Badro, John P. Brodholt, Hélène Piet, Julien Siebert, and Frederick J. Ryerson. Core formation and core composition from coupled geochemical and geophysical constraints. *Proceedings of the National Academy of Sciences*, 112:12310–12314, 09 2015. doi: 10.1073/pnas.1505672112.

Marc M Hirschmann, Anthony C Withers, Paola Ardia, and N.T Foley. Solubility of molecular hydrogen in silicate melts and consequences for volatile evolution of terrestrial planets. *Earth and Planetary Science Letters*, 345-348:38–48, 09 2012. doi: 10.1016/j.epsl.2012.06.031.

Takuo Okuchi. Hydrogen partitioning into molten iron at high pressure: Implications for earth's core. *Science*, 278:1781–1784, 12 1997. doi: 10.1126/science.278.5344.1781.

Gordon T Moore, Torsten Vennemann, and Ian . An empirical model for the solubility of h<sub>2</sub>o in magmas to 3 kilobars. *American Mineralogist*, 83:36–42, 02 1998. doi: 10.2138/am-1998-1-203.

Vivian Pan, John W Holloway, and Richard L Hervig. The pressure and temperature dependence of carbon dioxide solubility in tholeiitic basalt melts. *Geochimica et Cosmochimica Acta*, 55:1587–1595, 06 1991. doi: 10.1016/0016-7037(91)90130-w.

Jonathan Goodman and Jonathan Weare. Ensemble samplers with affine invariance. *Communications in Applied Mathematics and Computational Science*, 5:65–80, 01 2010. doi: 10.2140/camcos.2010.5.65. URL https://msp.org/camcos/2010/5-1/p04.xhtml.

Daniel Foreman-Mackey, David W. Hogg, Dustin Lang, and Jonathan Goodman. emcee: The mcmc hammer. *Publications of the Astronomical Society of the Pacific*, 125:306–312, 03 2013. doi: 10.1086/670067. URL https://arxiv.org/pdf/1202.3665.pdf.

James M. Flegal, Murali Haran, and Galin L. Jones. Markov chain monte carlo: Can we trust the third significant figure? *Statistical Science*, 23(2), May 2008. ISSN 0883-4237. doi: 10.1214/08-sts257. URL http://dx.doi.org/10.1214/08-STS257.

Rob J Spaargaren, Haiyang S Wang, Stephen J Mojzsis, Maxim D Ballmer, and Paul J Tackley. Plausible constraints on the range of bulk terrestrial exoplanet compositions in the solar neighborhood. *The Astrophysical Journal*, 948:53–53, 05 2023. doi: 10.3847/1538-4357/acac7d.

Fabian L. Seidler, Paolo A. Sossi, and Simon L. Grimm. Impact of oxygen fugacity on the atmospheric structure and emission spectra of ultra-hot rocky exoplanets. *Astronomy Astrophysics*, 09 2024. doi: 10.1051/0004-6361/202450546.

J Li, B Chen, Mainak Mookherjee, GUILLAUME Morard, B Orcutt, I Daniel, and R Dasgupta. Carbon versus other light elements in earth's core. *Deep Carbon (Cambridge University Press, Cambridge, ed. 1, 2020)*, pages 40–65, 2019.

Dongyang Huang, James Badro, John Brodholt, and Yunguo Li. Ab initio molecular dynamics investigation of molten fe–si–o in earth's core. *Geophysical research letters*, 46:6397–6405, 06 2019. doi: 10.1029/2019gl082722.

Aurélien Falco, Pascal Tremblin, Sébastien Charnoz, Robert J Ridgway, and Pierre-Olivier Lagage. Hydrogenated atmospheres of lava planets: Atmospheric structure and emission spectra. *Astronomy and Astrophysics*, 683:A194–A194, 02 2024. doi: 10.1051/0004-6361/202347650.

Mantas Zilinskas, van Buchem, Yamila Miguel, Amy Louca, Roxana Lupu, Sebastian Zieba, and W. van Westrenen. Observability of evaporating lava worlds. *Astronomy and Astrophysics*, 661:A126–A126, 05 2022. doi: 10.1051/0004-6361/202142984.

Caroline Dorn and Tim Lichtenberg. Hidden water in magma ocean exoplanets. *The Astrophysical Journal Letters*, 922:L4, 11 2021. doi: 10.3847/2041-8213/ac33af.

Julia Venturini, Maria Paula Ronco, and Octavio Miguel Guilera. Setting the stage: Planet formation and volatile delivery. *Space Science Reviews*, 216, 07 2020b. doi: 10.1007/s11214-020-00700-y.

# Appendix

## A: Gelman-Rubin Statistics

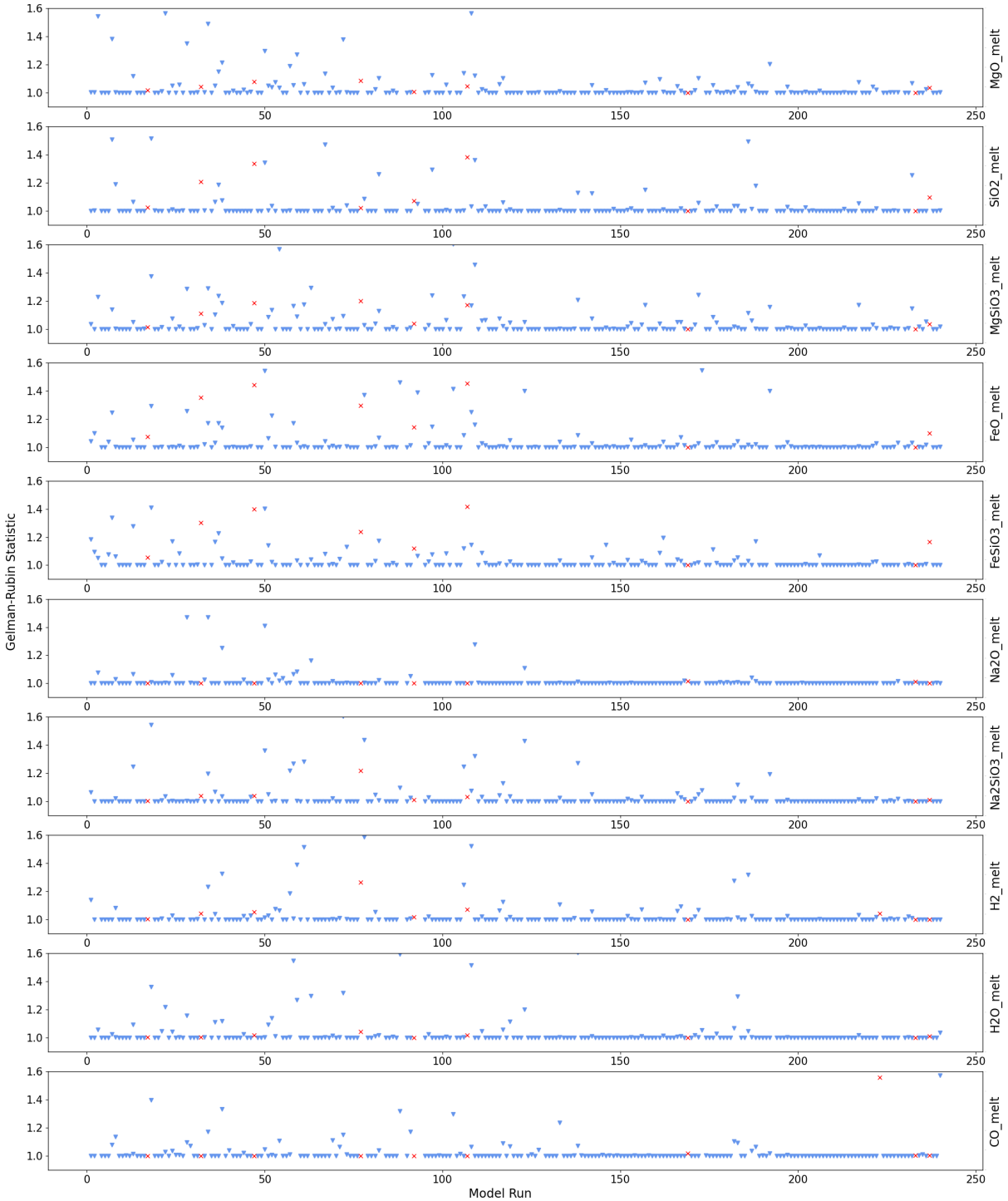


**Figure 32:** Calculated Gelman-Rubin statistics for model variables across 240 model runs. Datapoints marked by an 'x' have a reduced $\chi^2$ statistic above $1.0$. Shown here are the first ten model variables.

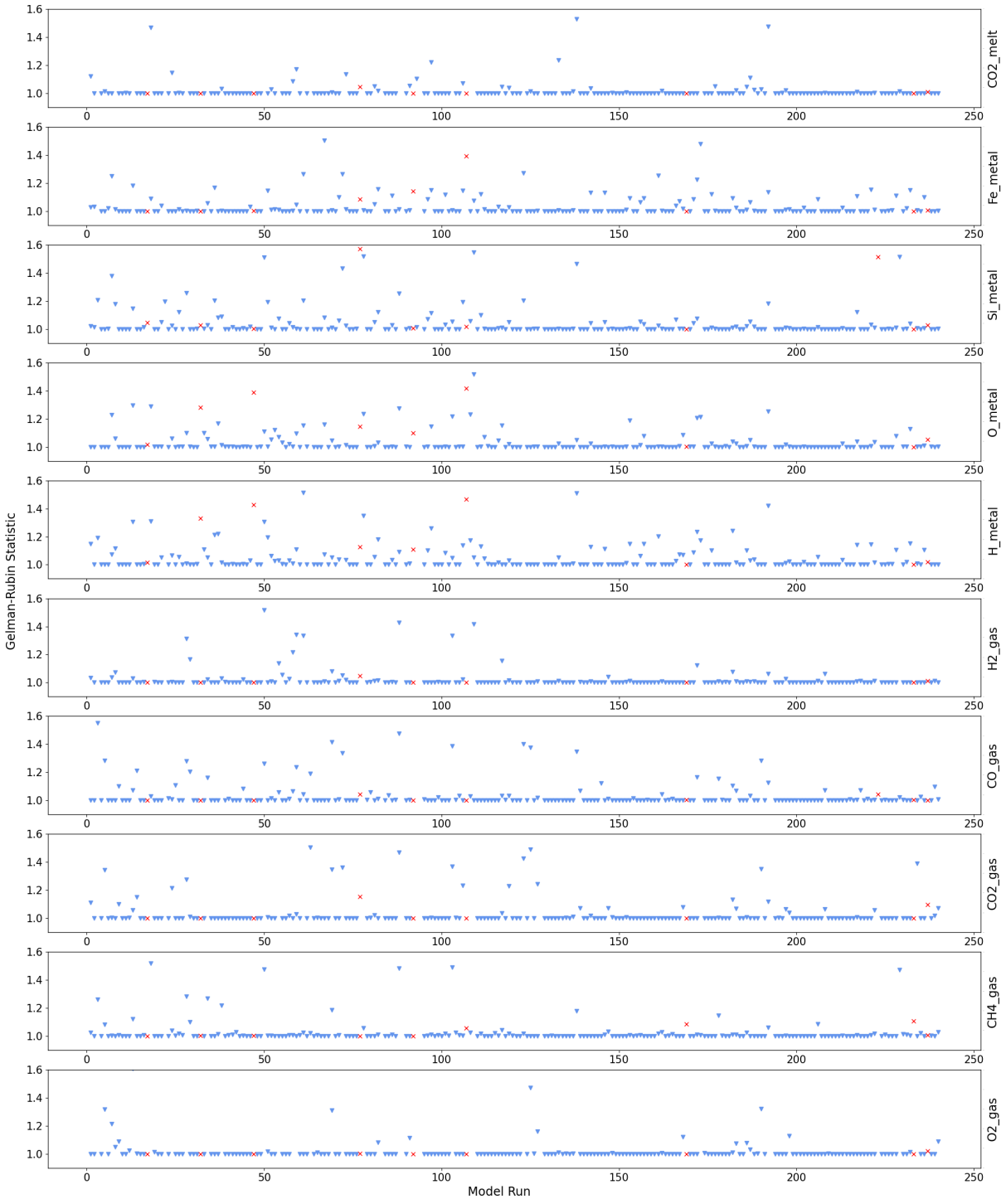


**Figure 33:** Same as Figure 32, for variables 11 to 20.

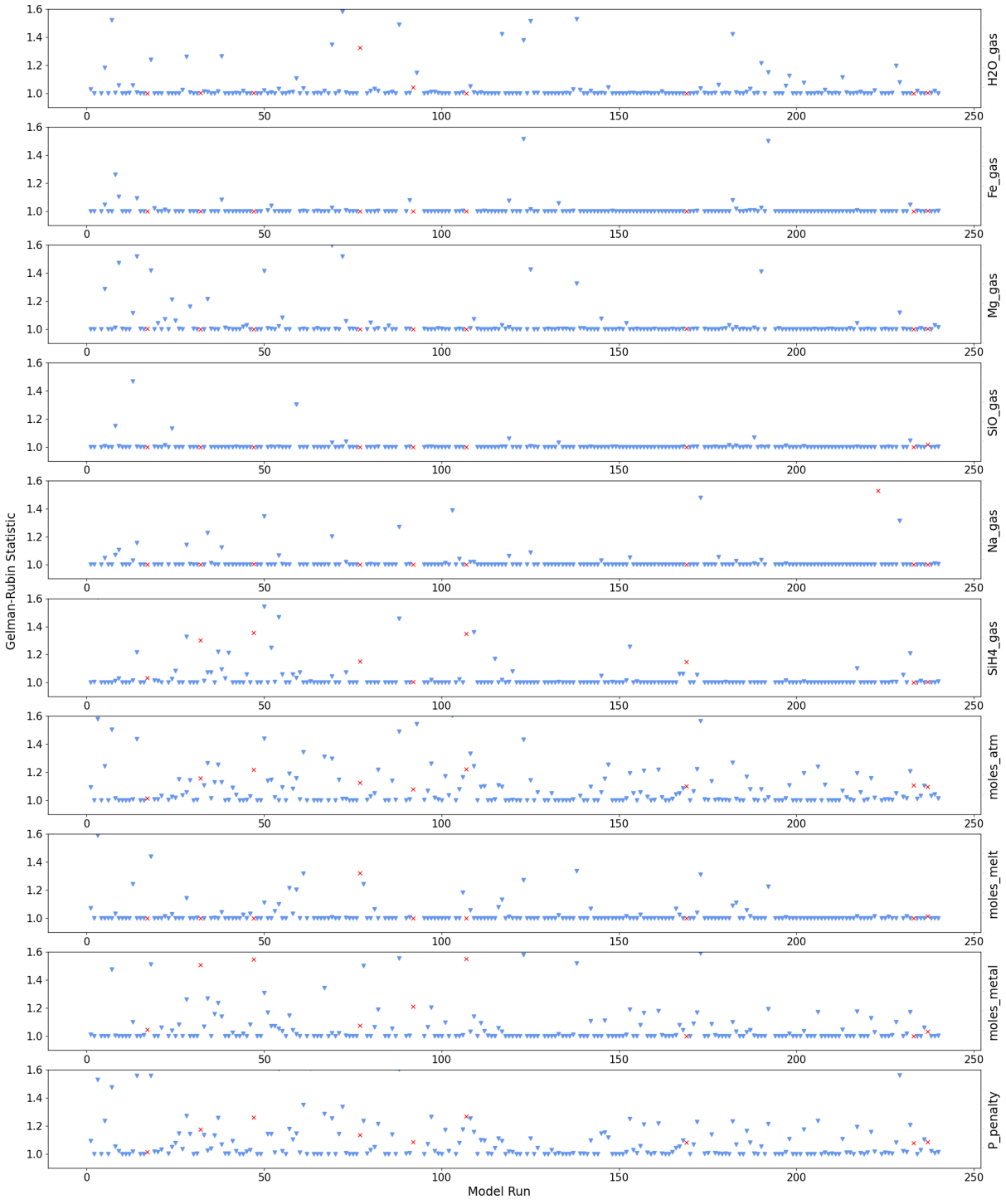


**Figure 34:** Same as Figures 32 and 33, for variables 21 to 30.

## B: Cornerplots

Shown in this appendix are two 7x7 cornerplots of the same species as presented in Figure 31, showing how runs with statistics satisfying my convergence criteria can have cornerplots which suggest poor or non-convergence. Figure 35 shows a cornerplot with broadly well-constrained contours, but including several 'blobs' that could be indicative of unconverged walkers or insufficient sampling.

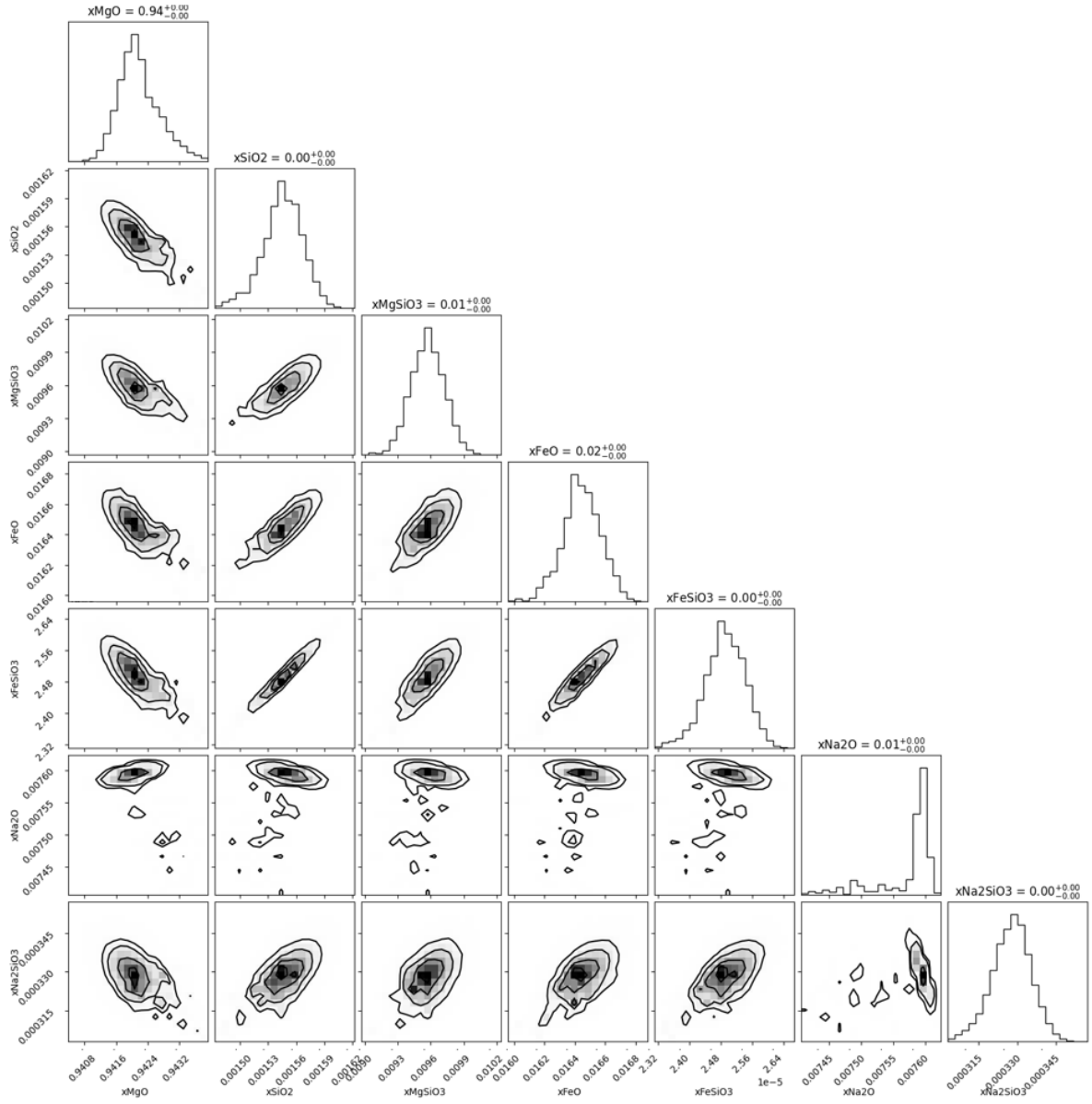


**Figure 35: 7x7 Cornerplot following converged MCMC run, but showing signs of possible non-convergence.** Melt-species $\mathrm{MgO}$, $\mathrm{SiO_2}$, $\mathrm{MgSiO_3}$, $\mathrm{FeO}$, $\mathrm{FeSiO_3}$, $\mathrm{Na_2O}$ and $\mathrm{Na_2SiO_3}$ are shown. Results stem from a model run with $T_s = 5000$ K; $T_{eq} = 6000$ K, and evaluated a reduced $\chi^2$ statistic $= 0.126$

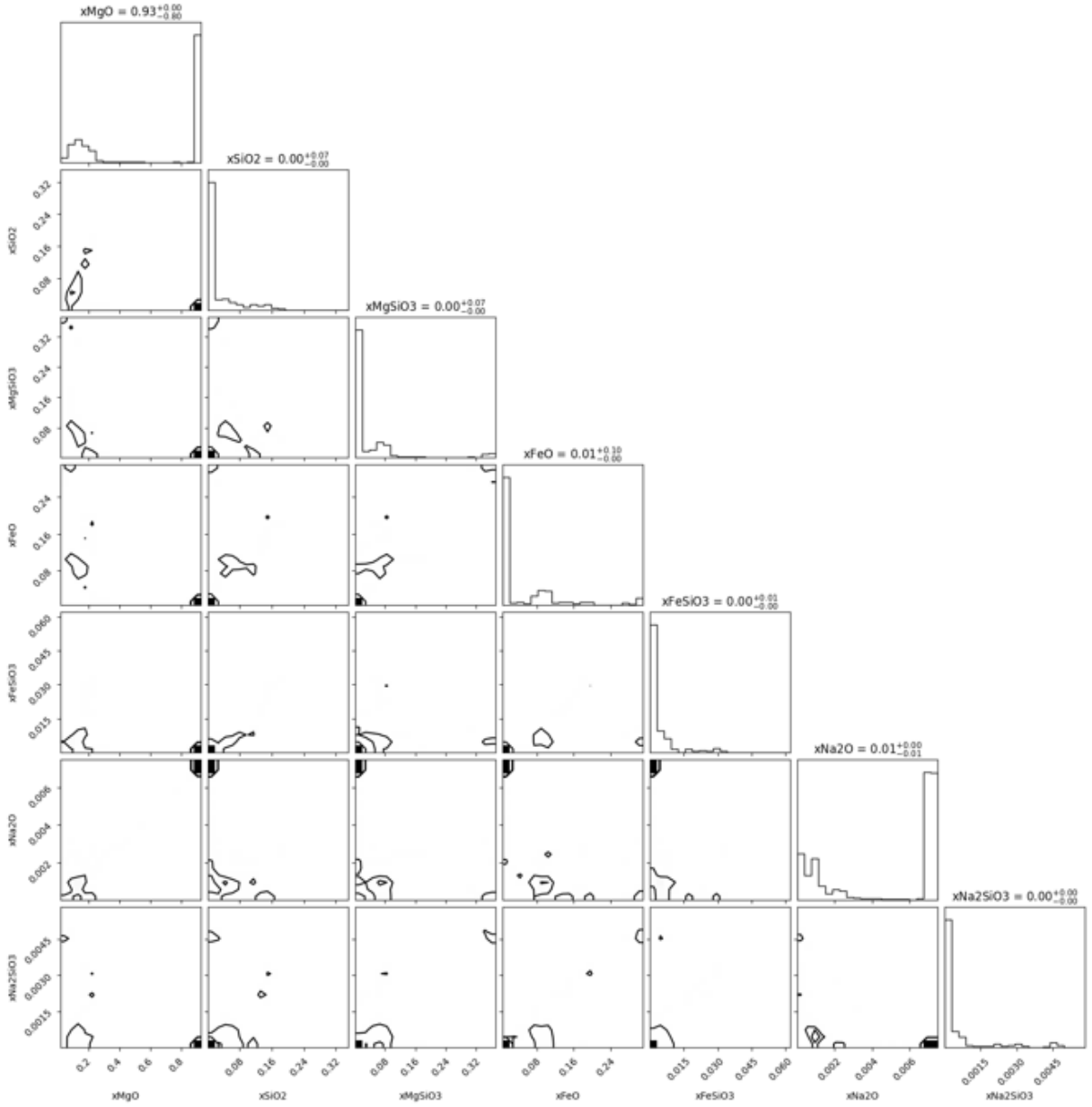


**Figure 36: 7x7 Cornerplot following converged MCMC run, but showing signs of poor convergence.** Melt-species $\mathrm{MgO}$, $\mathrm{SiO_2}$, $\mathrm{MgSiO_3}$, $\mathrm{FeO}$, $\mathrm{FeSiO_3}$, $\mathrm{Na_2O}$ and $\mathrm{Na_2SiO_3}$ are shown. Results stem from a model run with $T_s = 5000$ K; $T_{eq} = 6000$ K, and evaluated a reduced $\chi^2$ statistic $= 0.103$.

Figure 36 shows a cornerplot from another model run with good statistics, yet the cornerplot would suggest extremely poor MCMC walker convergence. There are no well-defined contours, and the resulting 1D histograms sample a very wide region and are asymmetric and jagged. Nevertheless, results from this model run show no deviation from trends established from adjecent runs in the parameter space.